Aerothermodynamic Analysis of Flow Modification Techniques in Non-equilibrium Supersonic/Hypersonic Flows

A thesis submitted

in partial fulfillment of the requirements

for the Degree of

DOCTOR OF PHILOSOPHY

in

Mechanical Engineering

by

SHAILENDRA KUMAR

Roll No : 166103001

Department of Mechanical Engineering

Indian Institute of Technology Guwahati

Guwahati - 781 039

"The only limit to our realization of tomorrow will be our doubts of today"
— Franklin D. Roosevelt

Dedicated to my
Parents

CERTIFICATE

It is certified that the work contained in the thesis entitled, "**Aerothermodynamic Analysis of Flow Modification Techniques in Non-equilibrium Supersonic/Hypersonic Flows**", submitted by Shailendra Kumar, in the Department of Mechanical Engineering, Indian Institute of Technology Guwahati, India, for the award of degree of Doctor of Philosophy has been carried out under our supervision and that this work has not been submitted elsewhere for the award of any other degree or diploma.

Signature: Date:

Supervisor: Dr. Vianyak N. Kulkarni
Department of Mechanical Engineering,
Indian Institute of Technology Guwahati,
Guwahati-781039, Assam, India.

ACKNOWLEDGEMENT

First of all thanks to God who has made me worthy of such a prestigious award. There are many people who need to be acknowledged.

Foremost, I would like to sincerely thank Prof. Vinayak N. Kulkarni for his invaluable guidance. I am deeply obliged to him for giving me the freedom to work in the aerodynamics field that I wanted. His critical comments and suggestions have been instrumental in completing this dissertation and I am extremely gratified with his endeavor in molding me into a disciplined research student. I would love to cherish my whole life in the memory of his association with me as a student.

Special thanks to Prof. Amaresh Dalal who taught me basics of Computational Fluid Dynamics. He also provided invaluable suggestions during my research work. I would like to thanks Prof. Niranjan Sahoo who taught me the gas dynamics subject which was very important for my entire research work. I never forgot mathematics class during my course work, as my favorite subject ever, that I learned from Dr. Arnab De. His lucid manner of teaching skills and knowledge always inspire me.

I would like to thanks my doctoral committee members, Dr. D. N. Basu, Dr. A. De, Dr. A. Shelke and Dr. G. Natragan, for their continuous guidance and proper suggestion during my research work. They are equally responsible to build confidence inside me by their constructive comments and advice.

I would like to extend my sincere thanks to past and present departmental heads Professor S. K. Dwivedy and Professor S. S. Senthivelan for their kind permission for enrollment, lab facilities and scholarship support in the mechanical department at IIT Guwahati.

I have been blessed with very good seniors and friends in my PGC lab. I never forget the contribution of *Siddesh Bhaiya* and *Shobhayen Bhaiyaa* to the completion of this research work. They are like my elder brother and a good teacher who taught me to use various research-related tools. I am fortunate to be a friend of *Jubajyoti*. He always helped in programming and debugging code during my course. I would like to thank *Masuruddin*, *Dhannajy* and *Ajay* for spending their time with me. I can write endlessly about the days we have spent together on the campus but some things are better left unsaid. In this campus, luckily I have surrounded by some very good friends, Harendra, Ali, Rasool, Amrita, Nagendra, Samrat, Sunita, Ramchandra, Anand, Anil, Abhishek, Samar, Shivdayal, and Sanjeev.

It is my pleasure to acknowledge the help provided by my senior and junior

students, Mukesh, Vishnu, Rahul, Sashidhar, Hidam, Inzmam, Sankalp, Keshar, Adit, Amitesh and all other lab members from our lab.

I am extending my thanks to my childhood friends, Tinku, Prabhat, Ajju, and Gautam for their motivation and supports.

In this precious moment of my life, I would like to express my deep sense of gratitude to my parents, Mr. Jawahar Prasad and Mrs. Urmila Devi for their love, blessings and constant encouragement throughout my life. I would like to thank my brother and sisters, Akhilesh Kumar, Pinku Kumari and Annu Kumari for their love and best wishes. Without their support, it would have been very difficult to finish my PhD work. I am deeply in debt to my family and friends for the sacrifices they have borne to ensure the fulfillment of my dreams. Next, I would like to express my special sense of gratitude to my grandparents Late Mr. Pati Mahto and Mrs. Bhaso Devi for their blessing. I am also grateful to my uncle, Vinod Prasad and Pramod Prasad for their constant encouragement throughout my life. I want to thank those guardians (Late Raani, Late Durga Devi and Late Sanju Devi) who are not in this world but their blessing are always with me. I also thank my family members, Shivanand, Mukul, Manish, Satyendra, Piyush, Prateek, Pusha, Pankaj, Rajeev, Dhanjany, Sanjay, Vijay, Gulshan, Uday, Suday, Suman, Preeti. I want to offer my sincere gratitude to all of you. You have always been inspiring, supporting and teaching me to understand the true value of human life.

Shailendra

ABSTRACT

Higher wave drag is a common problem for an object flying in the supersonic or hypersonic flow regime. Hence, the present investigations use computational fluid dynamics as a tool to study the dynamics of flow field to mitigate the adverse effects in such a complex environment. For this, a finite volume-based two dimensional axisymmetric compressible reacting flow solver is developed which is comprised of five species and eleven chemical elementary reactions. This solver deals with the coupled form of Navier-Stokes equations and species conservation in such a way that both calorically perfect gas model and reacting gas model can be handled as per requirement. Temperature-dependent thermophysical parameters and transport properties are employed for the study of low as well as high enthalpy flow field. After subsequent validation, the present solver is used for the investigations of various flow modification methods in the low as well as high enthalpy flow field.

Initial investigations on blunt object show that downstream movement of the bow shock and shock stand-off distance lead to increases in the surface pressure and thus drag force. Lesser flow field temperature is marked for reacting gas solver and hence lower magnitude of the heat flux is predicted at higher stagnation enthalpy conditions. Shock reconstruction for the spiked object leads to the downstream movement of the upstream influence location (UIL) on the spike surface and upstream movement of the shock impingement location (SIL) on the object surface at higher enthalpy conditions. This flow alteration supports the downward shift of the conical shocks which leads to the lesser size of the recirculation zones. Hence, higher pressure and drag is obtained for every conical spike length at higher stagnation enthalpy cases. It is concluded that the effectiveness of spike towards drag reduction decreases in the reacting high enthalpy flows. Different shapes of the spike tip are also investigated for maximum drag reduction in high enthalpy flows. For a given spike length, the drag reduction efficiency of a flat-tipped spike is found better than the spherical and conical tipped spikes at higher enthalpy consideration. Integration of two drag reduction methods, spike and counter flow jet, is also investigated for higher drag reduction. Here, very small pressure ratio of the jet (PR=0.1) and spike length (L=0.5D) are marked for significant drag reduction in case of the blunt object. A larger mass flow rate of the jet leads to greater amount of drag reduction.

Further, studies are carried out to understand the Shock-Shock (S-S) interactions for a spherical object in the presence of a forward-facing stagnation spike. The shock

stand-off spike (L=0.125D) witnesses initiation of the S-S interaction and seeding of a recirculation zone. This is the spike case at which frictional drag is higher than the wave drag. Further longer spikes alter the recirculation bubble size and S-S interaction type. Stronger interaction and undeveloped recirculation, for spike length of 0.25D, lead to maximum drag enhancement for the object. Higher exergy destruction is also observed for the same spike length. Further increment in spike length produces weaker interaction as well as larger recirculation zone which improves drag reduction for the same object. Combination arrangement of spike (L=0.25D) and counter-flow jet is also investigated to demonstrate the drag reduction criteria for the short spiked configurations. It is found that at least two recirculation zones and weak S-S interaction are mandatory for the realization of drag reduction using a stagnation spike.

Unsteady and steady energy deposition techniques are also studied for the drag alteration in non-equilibrium flow. Initial simulation for the unsteady energy deposition is carried out at lower enthalpy (0.3 MJ/Kg) to realize the real gas effects on surface pressure, reduced energy and drag signal for a spherical object. Later studies at higher freestream enthalpy show increase in pressure and decrease in density in the deposited energy pulse. Moreover, the size of the blast wave increases for elevated enthalpy cases. This alteration in energy pulse leads to the formation of a stronger vortex in the stagnation region and witnesses generation of an extra valley in the drag signal. Hence, power effectiveness for the energy pulse increases at higher enthalpy conditions and it is in consistent with all upstream deposition locations. Further, steady energy deposition is marked with higher drag and lesser power effectiveness at higher stagnation enthalpy conditions. Hence, the unsteady energy deposition is found to be better for drag reduction over the steady energy deposition at higher enthalpy cases. Performance of unsteady energy deposition has shown further improvement when multiple pulses are deposited in a certain frequency at a given upstream location.

CONTENTS

LIST OF FIGURES

LIST OF TABLES

ABBREVIATIONS

CFD	-	Computational fluid dyanamics
CFL	-	Courant friedrichs lewy
CV	-	Control volume
FSE	-	Freestream stagnation enthalpy
FVM	-	Finite volume method
NS	-	Normal shock
OS	-	Oblique shock
PGS	-	Perfect gas solver
PE	-	Power effectiveness
RGS	-	Reacting gas solver
SED	-	Steady energy depposition
SFD	-	Skin frictional drag
SIL	-	Shock impingement location
SSI	-	Shock-Shock interactions
SSOD	-	Shock standoff distance
SWBLI	-	Shock wave boundary layer ineraction
UED	-	Unsteady energy deposition
UIL	-	Upstream influence location
WD	-	Wave drag

NOMENCLATURE

A_p	-	Projected area of blunt object (m^2)
C_{wd}	-	Co-efficient of wave drag
C_{fd}	-	Co-efficient of frictional drag
C_i	-	Mass concentration of species i (kg/m^3)
C_p	-	Co-efficient of pressure
C_{pi}	-	Specific heat of i^{th} species at constant pressure (J/kmolK)
D_m	-	Diffusin coefficient (5×10^{-5} m^2/s)
E	-	Total energy (J/kg)
e	-	Internal energy (J/kg)
e_i	-	Internal energy of i^{th} species (J/mol)
E_I	-	Inviscid/Convective flux vector in x direction
F_I	-	Inviscid/Convestive flux vector in y direction
E_v	-	Viscous flux vector in x direction
F_v	-	Viscous flux vector in y direction
h_i	-	Specific enthalpy of i^{th} species (J/(kg))
h^0_{fi}	-	Heat of formation of i^{th} species (J/mol)
H_o	-	Freestream stagnation enthalpy (J/kg)
k	-	Conductivity (W/(m K))
L	-	Upstream location of energy deposition (mm)
MW_i	-	Molecular weight of i^{th} species
p	-	Pressure (N/m^2)
Q	-	Energy strength(W)
q_x	-	Heat flux in x direction (W/m^2)
q_y	-	Heat flux in y direction (W/m^2)

r	-	Radius of energy spot (mm)
Re	-	Reynolds number
R_u	-	Universal gas constant (J/kmolK)
S_I	-	Inviscid/Convective axisymmetric source term
S_i	-	Species production rate of i^{th} species (kg/m^{3}s)
S	-	Source term vector
S_v	-	Viscous axisymmetric source term
t	-	Time (s)
t^*	-	Dimensionless time
T	-	Temperature (K)
T_R	-	Reference temperature (K)
T_{wall}	-	Wall temperature (K)
T_∞	-	Freestream temperature (K)
Y_i	-	Mass fraction of i^{th} species
U	-	State/Conserved variable vector
U_∞	-	Freestream velocity (m/s)
u	-	Velocity in x direction (m/s)
$\overline{u}_{\ i}$	-	Diffusion velocity of i^{th} species in x direction (m/s)
v	-	Velocity in y direction (m/s)
$\overline{v}_{\ i}$	-	Diffusion velocity of i^{th} specis in y direction (m/s)
α	-	Constant ($\alpha = 0$ for 2-D problem and $\alpha = 1$ for axisymmetric cases)
ρ	-	Density (kg/m^3)
ρ_∞	-	Freestream density (kg/m^3)
δ	-	Shock standoff distance (mm)
$\tau_{xx}, \tau_{xy}, \tau_{yy}, \tau_{\theta\theta}$	-	Components of shear stresses (N/m^2)
μ	-	Viscosity (N s/m^2)

CHAPTER 1

INTRODUCTION

1.1 Background

Despite many failures before a successful attempt to fly, Ornithopters built the possible perceptions of flight at the end of 15^{th} century. Their interpretations helped many researchers to build the first fly by ballons in the year 1977 which was followed by the development of Glider in the year 1783 and fixed-wing aircraft in the year 1799. Later, Wright brothers registered their signature for manifesting the human flight propelled by gasoline-powered engine on 17^{th} Dec. 1903. This successful revolution drastically changed the field of aerodynamics and then mankind witnessed the first supersonic flight in 1947. Afterwards, the desire of flying faster and higher led to the exponential increase in the development of various space vehicles.

The design and development of a space vehicle for any mission or objective mainly revolve around the aerodynamic regime of the flight. An aircraft or space vehicle encounters different flow regimes such as subsonic, sonic, supersonic and hypersonic during its flight. These regimes are conventionally decided by a non-dimensional flow parameter, Mach number, which is expressed as M or Ma as the ratio of velocity and local speed of sound. If speed of the aircraft exceeds the speed of sound or Ma is greater than one, then the flow regime is characterized as the supersonic flow. Most of the fighter planes and aircraft like the BAC Concorde and Tupolev Tu-144 are examples of such supersonic vehicles. Moreover, if the vehicle speed is greater than five times the speed of sound or Ma is greater than 5, then the regime is named as the hypersonic flow regime. As hypersonic flow is a subset of the supersonic flow, but it possesses some special characteristics which separate it from other flow regimes. These

features include thin shock layer, entropy layer, viscous interaction, high-temperature flows etc. However, these features generate various adverse effects and corresponding complications on the high-speed vehicle during its flight. These special features include the low-density effect, high-temperature effect and real gas effect which are responsible for the generation of complex flow patterns like Shock-Shock interactions, higher drag force and aerodynamic heating. As a result of this, performance of the high-speed vehicles gets lowered due to increased fuel consumption, decreased payload capacity, communication blackout etc. Hence, these adverse effects need to be addressed for the safe, cost-effective and faster flight of the hypersonic vehicle. BrahMos-11, Shaurya and Boeing X-51 waverider are the example of such modern high-speed vehicles. In the following sections, different issues related to the hypersonic vehicle are detailed.

1.1.1 Effect of higher temperature

Subsonic or low-speed vehicles encounter different fluid dynamics than hypersonic aircraft. In this flow regime, due to lesser changes in temperature, there is no change in the internal degree of freedom and even no possibilities of chemical reactions. As a result, the behavior of gas can be approximated as an ideal or perfect gas. Thus for most of the flight conditions, the gas is modeled as the calorically perfect gas. In the above said gas model, the specific heat at constant pressure (C_p), specific heat at constant volume (C_v) and specific heat ratio (γ) remain constant. Also, the transport properties of the fluid such a viscosity and conductivity remain unchanged with the temperature. On the other hand, high-speed vehicles when form very strong bow shock around the blunt surface they experience very high post-shock temperature. This higher temperature is due to the conversion of the kinetic energy into the internal energy in the shock layer. This higher temperature leads to vibrational excitation and even initiates the dissociation and recombination chemical reactions. Atmospheric air is composed of various gaseous compounds in which concentrations of Oxygen (O_2) and Nitrogen (N_2) are higher. The concentration of these species changes at higher temperature due to chemical reactions. These reactions produce new species (like O and N) from the existing species of the air (like O_2 and N_2) and these new molecules recombine to form other new species (like NO, O_2 and N_2). Figure 1.1 gives the relevance between temperature and the reactions. The flow behavior in the presence of chemical reactions is governed by the completion time of these chemical reactions. In such flows, changes in the thermophysical properties like viscosity, conductivity, specific heats and specific heat ratio are inevitable. This type of flow is commonly referred to as the chemically reacting gas flow and gas is modeled with the reacting gas model. Here, it is clear that the calorically perfect gas model is not valid in high-

temperature flow situations. Therefore, it is highly desirable to study the effect of such flows on high-speed configurations.

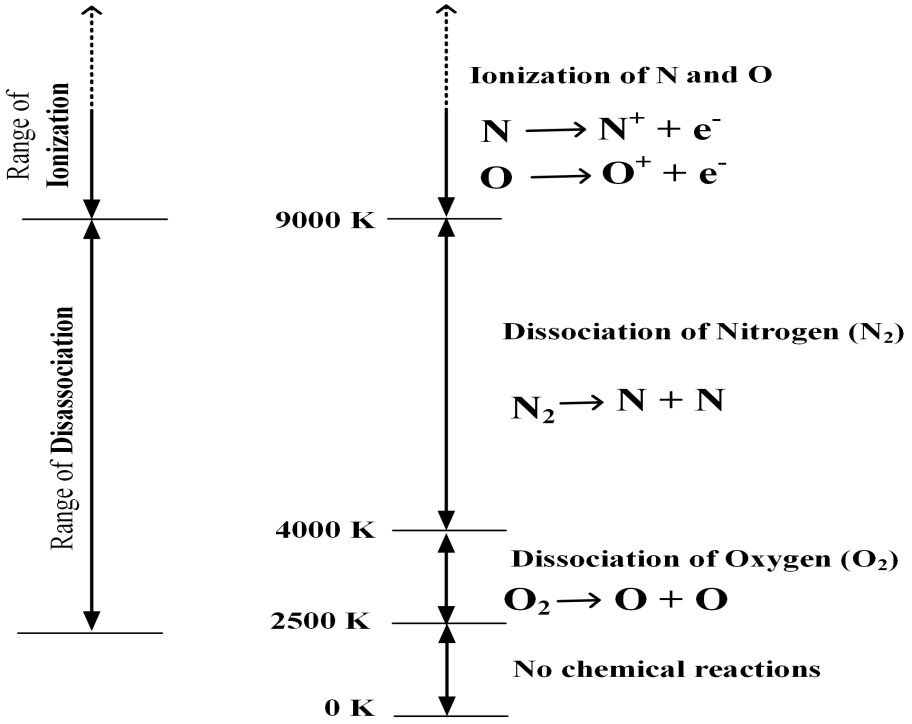

Figure 1.1: Behaviour of air molecule with the temperature

1.1.2 Chemical reactions in high enthalpy flow

In high enthalpy flow, different types of chemical reactions are possible, among which some are listed below:-

Dissociation reaction

The term 'dissociation' is referred to when there is a breakge of a compound into more than one constituents. This reaction demands energy input, thus it is a type of endothermic chemical reaction. From Fig. 1.1, it is clear that dissociation of oxygen starts when the temperature of air reaches 2500 K at 1.01325 bar. In this process, the molecule of O_2 breaks and forms atoms O.

$$O_2 + energy \rightarrow 2O$$

Further, molecule of the Nitrogen (N_2) starts dissociation at some higher temperature (4000 K) and continue to dissociate till 9000 K. This can also be seen in the Fig. 1.1 and expressed as:

$$N_2 + energy \rightarrow 2N$$

Recombination reaction

Recombination is an exothermic reaction in which two or more similar or dissimilar species recombine to form one molecule or more than one smaller atoms or molecules or both. For example, the recombination reaction of Oxygen and Nitrogen atoms is expressed as:-

$$O + O \rightarrow O_2 + energy$$
$$N + N \rightarrow N_2 + energy$$

Ionization reaction

This term is characterized by gaining or losing of ion by an atom. This can be a result of the collision between two different or the same molecules or atoms. For example, as shown in Fig.1.1 when the temperature of atmospheric air is more than 9000 K then ionization of the nitrogen atom is observed. This can be expressed below as:-

$$N + energy \rightarrow N^+ + e^-$$

1.1.3 Types of flows based on chemical reactions

The term "reaction rate" or "rate of reaction" or "reaction time" signifies how fast or how slow a chemical reaction takes place. Hence there exists a time scale associated with the chemical reactions. Further, the "flow time" or "rate of flow" has relevance with the time scale of the flow. Based on these two time scales, flows can be categorized as follows:

Frozen flow

This type of flow is encountered when the rate of reaction is very small in comparison with the flow rate. In other words, for a given flow, the reaction time is very large as compared to the flow time. Therefore no reaction triggers in the flow as shown in Fig. 1.2 (a).

Equilibrium flow

On the other hand, if the rate of reaction is very high as compared to the flow rate then the reaction time becomes very small as compared to the flow time. Since the time required to initiate a reaction is very small, the composition changes in a very small distance as presented in Fig. 1.2 (b). This type of flow is generally categorized as the equilibrium flow.

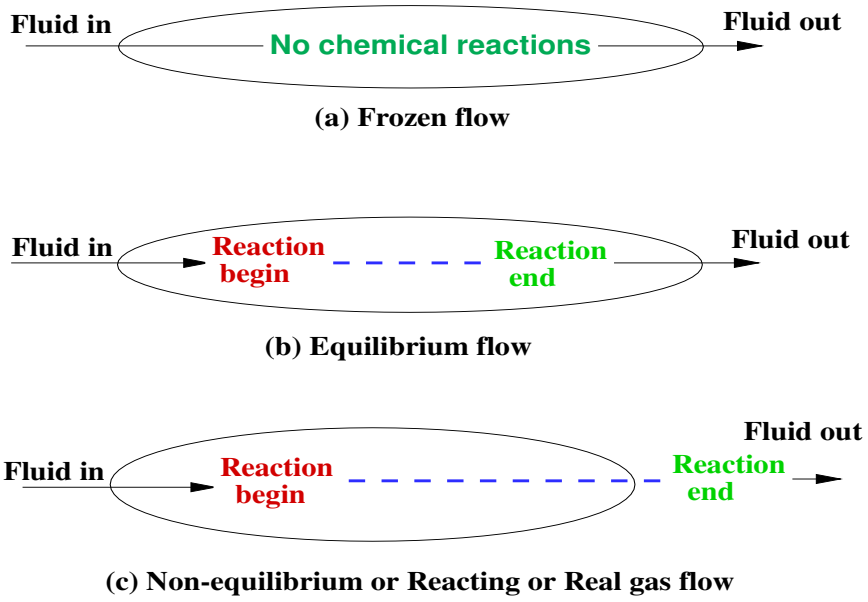

Figure 1.2: Schematic of flows based on chemical reactions

Non-equilibrium flow

The above described flows have either a very fast reaction rate or a very slow reaction rate. These are two extreme conditions for the flow. However, if the reaction time scale and flow time scale are equal then such flows are known as non-equilibrium flow. In this type of flow, chemical reaction triggers but never completes in the flow domain as shown in Fig. 1.2 (c).

1.2 Drag reduction techniques

Objects experiencing hypersonic flow like launch vehicles, re-entry vehicles and space planes have blunt shape configurations. The surface heating loads of these vehicles can be reduced by making them blunt at the nose as the surface heating is inversely related to the nose radius at hypersonic speed. This blunt shape keeps the bow shock away from the object and thus helps in reducing the surface heating. Still, the blunt configurations lead to higher surface heating for a small area of the object, near the stagnation region, and lower heating for the rest part of the vehicle. Despite the major advantage of reduced heat flux, these blunt configurations inherent disadvantage associated with the upstream formation of strong bow-shock as larger wave drag. Such a higher drag force is advantageous during the descent phase of the flight but increases

the fuel consumption during ascent and cruise phases. To overcome the limitations and hurdles caused due to the presence of bow shock, various structured or passive and un-structured or active methods are used by researchers. These methods are employed to alter the location and shape of the bow-shock and hence adjust the external flowfield to regain a new effective body shape. These alterations lead to changes in the aerothermodynamic properties like reduction of pressure and temperature in the shock layer. Such alterations help in the reduction of wave drag, frictional drag and surface heating load on the hypersonic object. Some of the drag reduction techniques are briefly explained in the following subsections.

Forward facing spike

Attaching an aerospike at the nose of a blunt-body is a widely adopted method for reducing the drag force. In this structured or passive method, a metallic bar or spike of fixed shape and base diameter but variable length can also be selected for the above said purpose. This solid spike replaces the strong bow shock, which is initially formed around the object, into oblique or conical shocks. These conical shocks are due to

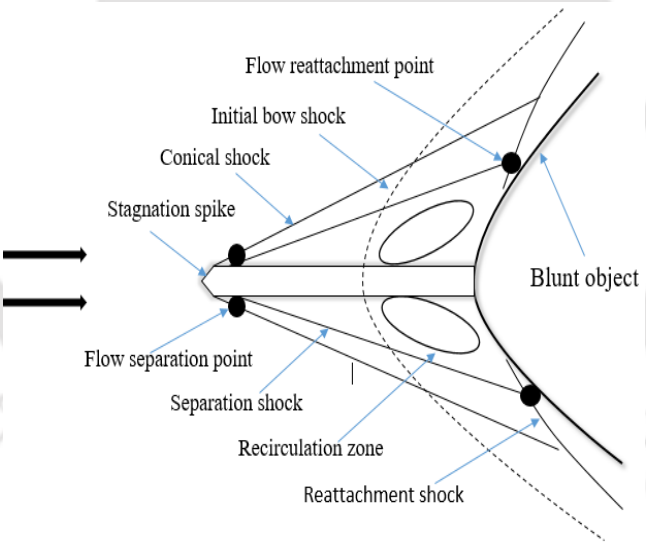

Figure 1.3: Schematic of aero-spike based drag reduction technique

flow separation from the tipping point of the spike surface and its reattachment on the body surface as shown in Fig. 1.3. This phenomenon reassures formation of the conical dead air region or recirculation zone near the stagnation region [1]. Such recirculation zone has low pressure, low temperature and low-density gas which is responsible for the lower drag and heat load on the object. Without such a spike, strong bow shock would impose pressurized gas on the object and thus offers higher drag force or wave drag. But in presence of a spike, an object gets surrounded with a low-density gas

which imposes less drag on it. Hence, the introduction of an aerospike is essential for the formation of the recirculation zone and to witness the drag reduction. The amount of drag reduction solely depends on the shape and length of the spike. In general, a larger length of the spike is selected for higher drag reduction. Different shapes of spike tip such as round or spherical, conical and flat-ended have been used for the better performance of spike towards reduction of the drag force. Because of the simplicity and cost-effectiveness advantages, this approach is widely adopted for the reduction of drag force as well as surface heat flux on the blunt object.

Energy deposition

Despite the structured method, an unstructured or active method has also been used by various researchers for drag reduction. Among those, upstream energy addition is an active or unstructured method in which steady energy is added by electric arc discharge or by microwave instruments. A fixed amount of energy is added along the stagnation streamline of the blunt object as shown in Fig. 1.4. This addition reconstructs the shock structure around the object by separating the flow downstream of energy deposition location and reattaching the same on the body surface [2]. Therefore

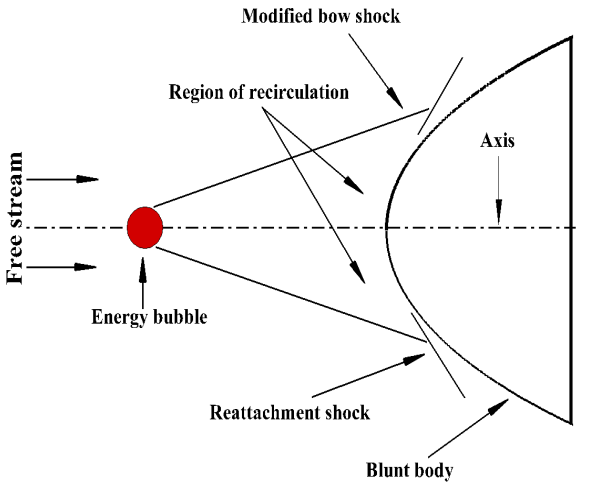

Figure 1.4: Schematic of steady energy deposition based drag reduction

energy deposition leads to the formation of a conical dead air zone near the stagnation region of the object. Due to this, less pressure acts on the object and thus drag force on the body decreases. The amount of drag reduction is dependent on the area of the conical dead air region near the stagnation point. This area may depend on several factors like the amount of energy addition (Q), the radius of the energy bubble (r)

and upstream location of the energy deposition [3]. This method is more useful for wave drag reduction rather than the heat load on the blunt object. In addition to the

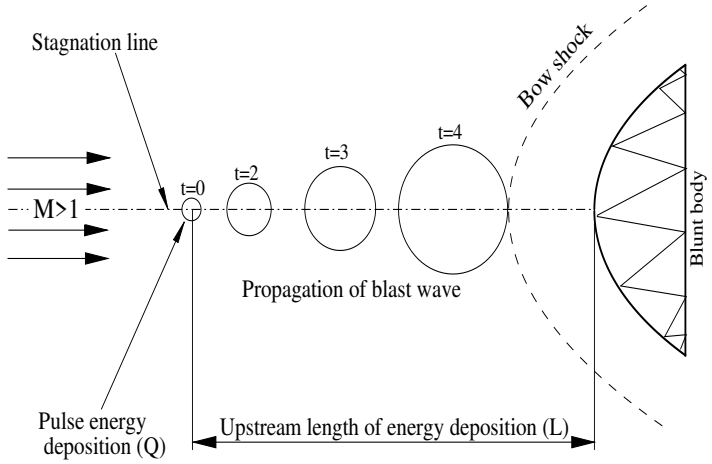

Figure 1.5: Schematic of unsteady enrgy deposition based drag reduction

steady energy deposition, unsteady energy deposition is also an unstructured method of drag reduction in the supersonic/hypersonic flow regimes. In this technique, an energy pulse is deposited for very small time instance, along the stagnation line, in front of the steady bow shock. Propagation of the pulse with the time makes its interaction with the standing bow shock as shown in Fig. 1.5. This action leads to the formation of low-density vortex in the flow field near the stagnation region [4]. This vortex travels, with the advancement of time, along the surface and imposes less pressure on the blunt object. This alteration in the flow field offers lesser drag on the body. Thus drag reduction due to the unsteady energy deposition solely depends on the strength of the vortex formed during the interaction. The effectiveness of this method towards drag reduction can be increased by changing the strength (Q) and upstream deposition location (L). Periodic deposition of the energy pulse is also a suitable approach for a larger reduction of wave drag.

Counter-flow jet injection

The counter jet injection method is an unstructured or active approach for drag and heat flux reduction. In this technique, an opposing jet is introduced from the nose point of the body [6]. The main function of this pressurized jet is to push the bow shock away from the body and to make a low-density recirculation zone around the stagnation region as shown in Fig. 1.6. This restructuring of the bow shock leads to less pressure on the object and thus reduces the drag [7]. The dead-air region

formed by these modifications acts as a blanket for the blunt object and thus reduces heat load as well. Any gas like air, Helium (He), Nitrogen (N2), Argon etc can be considered for injection. The total pressure of the gas and diameter of the jet outlet

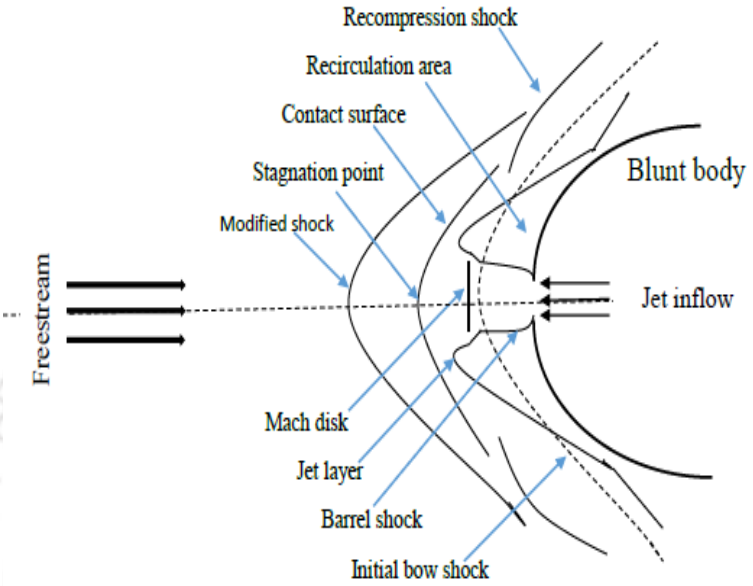

Figure 1.6: Schematic of counter jet drag reduction technique

are the controlling parameters for the amount of heat and drag reduction by this active method.

1.3 Shock-Shock (S-S) interactions

Proper design of the high-speed vehicle is the most interesting and challenging task for the researchers. This task requires a detailed analysis of the flow field for any adverse conditions of the hypersonic vehicles. The difficulties in understanding the flow field can be due to the interaction of different shock waves. As two shock waves of same or different strength are intersected then there is an alteration in the flow pattern near the object as shown in Fig. 1.7. This is also termed the Shock-Shock interaction. These interactions may lead to complex flow situations because of the presence of various shocks (Incident shock (IS), normal shock (NS), transmitted shock (TS) etc.), slip plane, sonic line, expansion fan and supersonic jets (SJ) as shown in Fig. 1.7. Also, the strength and structure of the shock waves may vary with the relative direction of the impinging shocks, their incidence angles, body geometry and the freestream Mach number. Moreover, the complexity of the interaction increases

especially in presence of the boundary layer and the chemical reactions in the gas. Further, these interactions are categorized based on complexity. Commonly, six types of interactions are known and they are discussed in the next section. These interactions

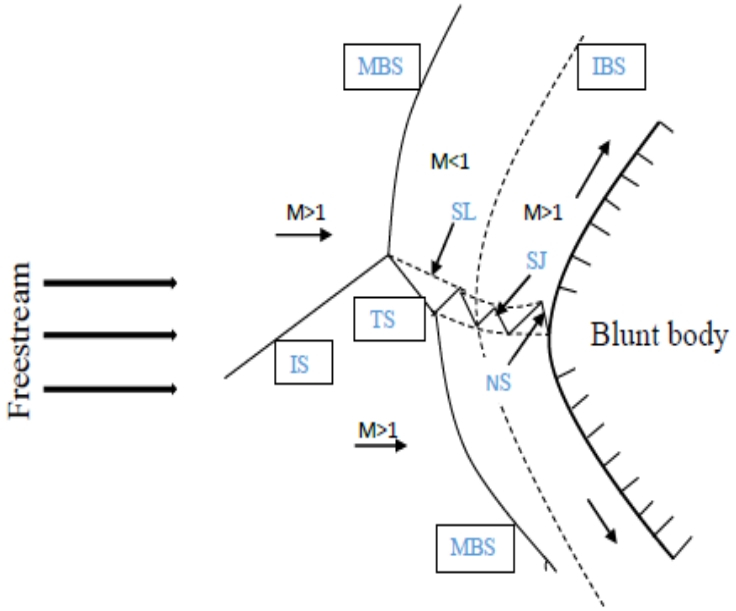

Figure 1.7: Schematic of the S-S interaction for spherical body. (IBS - Initial bow shock, MBS - Modified bow shock, IS - Incident shock, TS - Transmitted shock, SL - Slip line, SJ - Supersonic jet, NS - Normal shock)

can locally introduce very high rise in the pressure and heat load on a particular area of the flight. Such pressure rise can enhance the drag force and temperature rise can lead to the thermal stresses on the high-speed vehicle. Thus, it is necessary to predict the actual prediction of the shock-shock interactions for the safe flight condition. Such shock – shock interaction can also be observed in the case of missiles, space shuttles, long ranges space vehicles, scramjets etc. Further, flow modifications in the presence of spike, counter-jet or energy addition, for drag reduction also lead to interactions of different shocks. Hence, the performance of these drag reduction techniques is governed by the strength of such interactions. Therefore, it is highly desirable to understand the Shock-Shock interaction for the commonly used drag reduction techniques.

1.4 Literature review

Literature reported investigations about prominent issues in hypersonic flows (discussed above) are presented in this section.

1.4.1 High temperature effects

Pioneer contribution for the high-temperature effects on the flow field is by Brainerd and Emmons [8]. They incorporated temperature-dependent transport properties (μ and K) for the calculation of drag on the blunt object. Later, variable specific heats (C_p and C_v), as well as transport properties, were introduced by Moore [9] to solve the laminar boundary layer equations. Further advancement in reacting field of reacting flow was led by Fay and Riddle [10] and Rose [11], [12]. They proposed a theory of stagnation point heat transfer in the dissociated air. Later, the ionization along with the dissociation in the air was considered by Fenster [13] for the measurement of stagnation point heat flux. Further, the rapid and slow reaction rates were considered by Conti and Dyke [14] to see the effect of density, pressure and wave drag for the inviscid flow conditions. An algorithm, named UPWIND, based on the thermo-chemical non-equilibrium flows was developed by Liu and Vinokur [15]. Their solver incorporates the most generalized form of thermal and chemical non-equilibrium for any random gas. Further, the development of a flux splitting algorithm for non-equilibrium chemistry and thermodynamics was carried out by Grossman and Cinnella [16]. Netterfield [17] developed a 3-D PNS solver for the verification of the thermochemical results. For inviscid flux calculation, a second-order upwind TVD scheme was used and incorporated in a two-temperature model for a non-equilibrium solver. Later, Park [18] introduced the two-temperature model which is based on the translational and vibrational energy of the dissociated air. Again, Park [19] developed CENS2H program for the applications like sub-orbital hypersonic flight. It was proposed that there is 10% change in pitching moment and drag by the consideration of thermo-chemical behavior of air. A higher-order accurate non-equilibrium flow solver for the reentry vehicle was proposed by Sawley and Wothrich [20]. Further Sabetta et al. [21] compared the shock stand-off distance and stagnation pressure for the equilibrium and non-equilibrium models of air chemistry. They proposed that the equilibrium model over predicts the temperature and pressure at the stagnation point. But non-equilibrium model predicts almost double the shock stand-off distance as compared to the equilibrium one. Desideri et al. [22] used five chemical species model to describe the flow behavior around an object in dissociating high-temperature flow field. Similarly, five species model, as well as perfect gas model, was considered by Hassan et al. [23] for the aerothermodynamic analysis of aerobraking vehicles like the Apollo module. According to them, the prediction of flowfield temperature (as shown in Fig. 1.8 (a))as well as lift to drag ratio is lesser for the thermochemical model as compared non-reacting or perfect gas model. Later on, Miller et al. [24] developed the parabolized N-S (PNS) solver by incorporating the thermo-chemical non-equilibrium and equilibrium behaviors of air. For this, they considered seven species and seven chemical reactions in their compressible flow

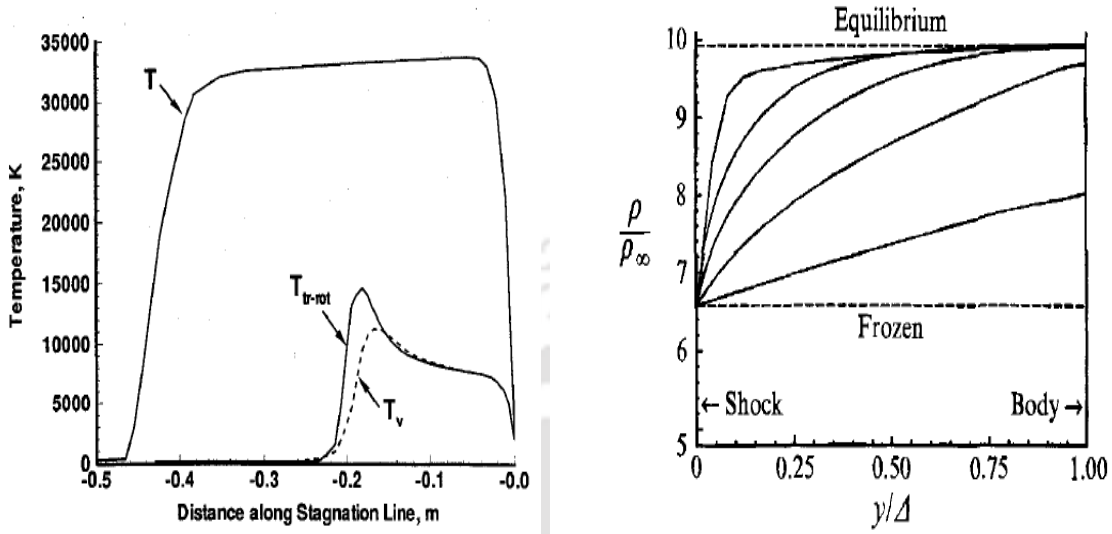

Figure 1.8: [Left] (a) Temperature distribution for perfect and reacting gas model ([23]) and [Right] (b) Density profile along the stagnation streamline for different reaction rates ([27]).

solver. The vibrational and chemical energy, of each species, in the reaction, is also accounted. The studies are further extended by Candler [25] by considering 8 species and 12 elementary chemical reactions along with the chemical kinetics model of the mixture of CO_2 - N_2 gases for the Martian atmosphere. A correlation of heat transfer for the Martian atmosphere was proposed. Eleven species model was incorporated by Gupta [26] for thermal equilibrium simulations. Here transport properties and chemical-reaction rates for all species were considered to be temperature-dependent till the temperature of 30000 K. Later, numerical and experimental investigations were carried out by Wen and Hornung [27] for the spherical object in hypersonic flow. They presented the behavior of bow shock for various inlet enthalpy cases which can be seen in Fig. 1.8 (b). Argyris et al. [28] showed the real gas effects by considering the mass transfer phenomena of the reacting species for viscous hypersonic flows. They extended their work to reduce the computational effort [29] associated with the chemical kinetics of species in the non-equilibrium solver. Reddy and Sinha [30] predicted heat flux with chemical reactions for FIRE-II capsule in high enthalpy flows. They mentioned that the recombination reaction of oxygen molecules gives larger heat load on the surface. Moreover, Greenshields and Reese [31] compared three non-equilibrium boundary conditions such as Patterson, Smoluchowski and the DSMC for the rarefied hypersonic flows (M=10).

1.4.2 Drag reduction

Attaching a forward-facing spike is the structural method of the drag reduction for the blunt object. Various studies for supersonic/hypersonic flows over spiked bodies are conducted both numerically and experimentally. Formost contributions in this area was by Mair [32]. A pointed spike of length (L) 1.5 times the body diameter (D) was mounted over the axisymmetric body with hemispherical and flat ends by Mair for the experimental investigations. It was concluded that the pattern of conical shock wave and size of the recirculation zone are strongly dependent on the flow around the separation point. Later, drag force and heat flux reduction for the blunt object, with forward-facing stagnation spike, were studied by Bognodroff and Vas [33]. They varied the spike length and body geometry (flat and hemispherically faced object) to get the maximum drag reduction in the hypersonic flow of Mach 14. In the experiments by Maull [34], it was found that the flow remains steady over the spike. The oscillations

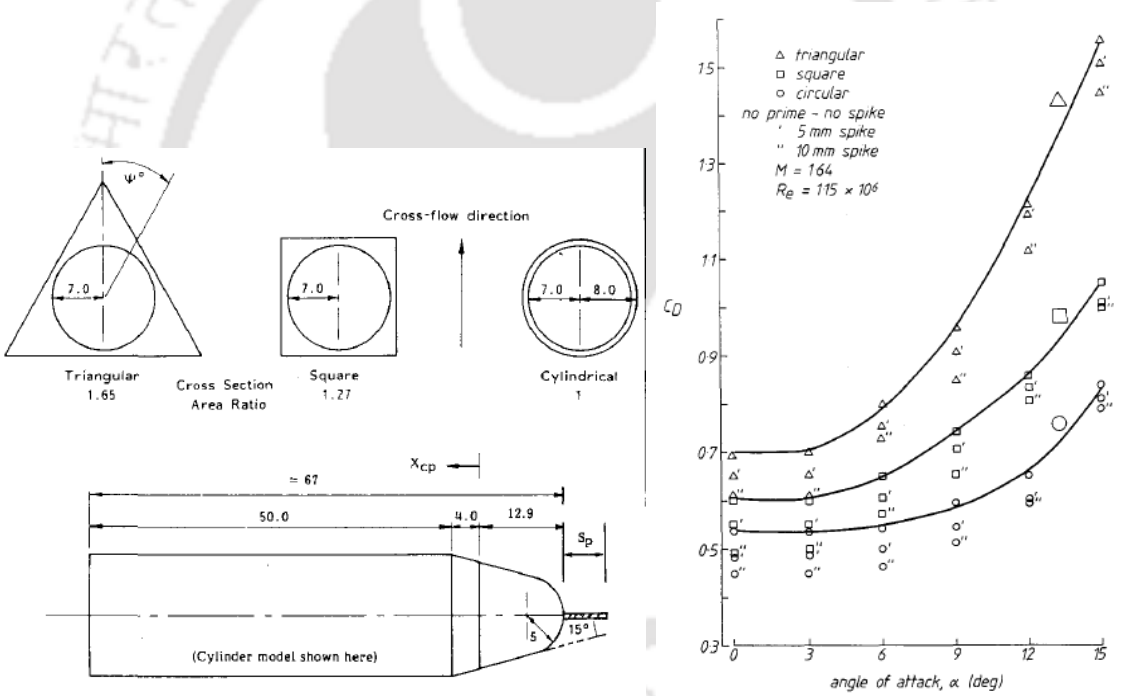

Figure 1.9: [Left] (a) Schematic of test model ([38]) and [Right] (b) Alteration of drag co-efficient with angle of attack for different shapes ([38]).

in the flow field arise from the separation because of the cylindrical test model has a shoulder radius less than the diameter of the afterbody. Later on, Wood [35] classified five types of separated flows which are based on the spike cone angle and spike length. In addition, a semi-empirical correlation was proposed to distinguish the type of separated flows for the hypersonic flow of Mach 10. Further, Zorea and Roam [36] performed an experimental investigation for the prediction of drag force of the spiked body by considering the stability of the object. They chose to have various angles

of attack and freestream Mach numbers for the optimum drag force measurements. It was concluded that there is a particular spike length after which drag reduction would be observed, and the static stability of the spherical object remains unaltered by attachment of the stagnation spike. Furthermore, Reding et al. [37] investigated the design optimization of the high-speed vehicle in the presence of a stagnation spike. On the other hand, Hutt and Howe [38] used three different cross-sections of the blunt-body (circular, triangular and square), as shown in Fig. 1.9 (a) and measured the drag force. In their remarks, they stated that the conical or triangular cross-section body with the stagnation spike, as shown in Fig. 1.9 (b) is a better configuration for lesser drag as it showed improved benefit in the lift as well in comparison with the other two. Shoemaker [39] explored for the optimum drag reduction with different lengths of the spike in supersonic flow of Mach 2.5. It was noticed that the spike effectively reduces the drag when freestream Mach is greater than 1.5. On the other hand, the effect of spike length and freestream Mach number on drag was investigated by Yamuchi [40]. Longer spike lengths were recommended because they create a larger recirculation area near the stagnation region, which intern helps to reduce the drag force. They also mentioned that the drag reduction is higher for the 10° angle of attack case as compared to 0° case for the same spike length and freestream conditions. Further, Hubner [41] showed the feasibility of spike-based drag reduction for a hypersonic flight at Mach 6 for various angles of attack during flow visualization, pressure measurements and temperature measurements. Later, Mikhail [42] performed steady and unsteady numerical investigations for the spiked-nosed projectile in supersonic flow. In these studies, Mikhail considered three different Mach numbers as 1.9, 3.0 and 3.5 to show the oscillations and time-dependent pressure variation. The oscillation frequency of 533 Hz was observed for the freestream Mach of 1.9 as compared to Mach number 3.5. Motoyama et al. [43] carried out experimental investigations in a hypersonic wind tunnel (KOMHYP) at Mach number 7. Both, aerodynamic heating and drag force were measured for various lengths and shapes of the spike for different angles of attack mountings. It was showed that the spike with an aerodisk shape is superior for heat flux and drag force reduction as compared to other shapes of the spike. Later on, Milicev and Pavlovic [44] experimentally measured lift and drag co-efficient for a blunt object at supersonic speed. During these measurements, they mounted the test model at different angles of attack and also considered various spike shapes. Their results emphasized on the spike shape for the amount of drag force reduction. Due to higher heating loads, the spherical tipped spike was recommended instead of other shapes. Further, Menezes et al. [45] performed shock tunnel testing with a 120° angle blunt cone model mounted with a flat disc stagnation spike. As per their measurements, there is 55% reduction in drag force at zero angle of attack for the hypersonic flow

of Mach number 5.75. Later, Asif et al. [46] performed numerical simulations to estimate the drag force for four different spike shapes mounted at the stagnation point. Their results showed that the test model with a hemispherical spike incurs lesser drag, as shown in Fig. 1.10 (a), and encounters maximum lift as compared to other spike mountings as shown in Fig. 1.10 (b). They also mentioned that increasing spike length

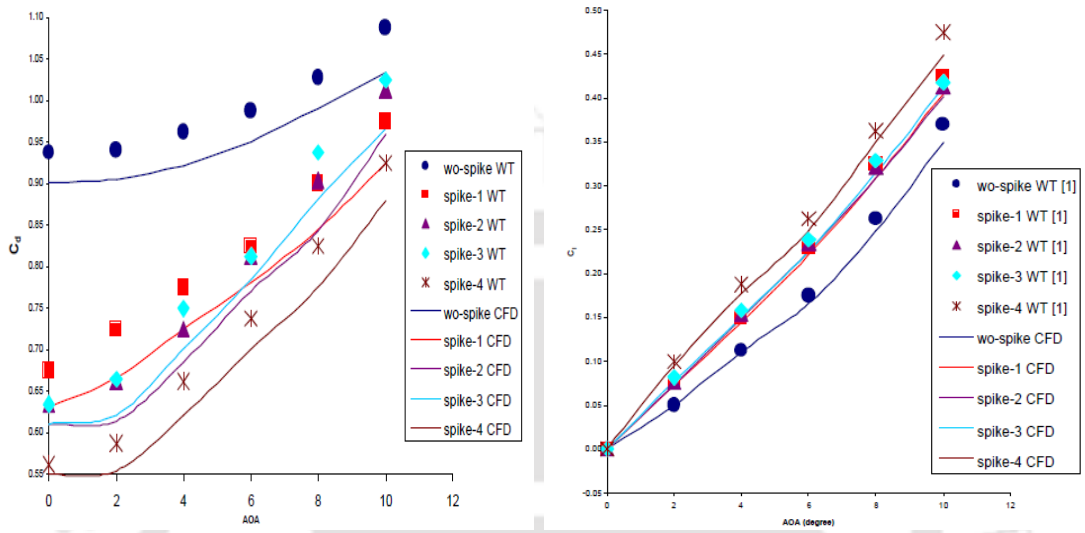

Figure 1.10: [Left] (a)Variation of drag with angle of attack ([46]) and [Right] (b) Alteration of lift ([46]).

increases the lift force and reduces the drag force but at the same time stability of the object diminishes. On the other hand, an experimental investigation by Kobayashi et al. [47] proved that higher spike length introduces instability and pressure fluctuations on the hypersonic vehicle. Therefore, they suggested using a telescopic spike with several disks on the shaft to divide the single separation bubble into multiple cavity conical flows. This arrangement allowed to use spikes of higher length due to lesser fluctuations. Further, Kulkarni et al. [48] used a flat-tip spike to measure the drag force of on a 120° blunt cone in hypersonic flow. Different freestream enthalpies were considered in their experimentation to prove that the drag reduction with the chosen spike remains independent of the freestream stagnation enthalpy. Later, Srinath and Reddy [49] accounted for various spike geometries during their shock tunnel tests for heat flux and drag force measurements. They recommended use of the telescopic spike over the conical tipped spike. Tahani et al. [50] carried out CFD simulations for the analysis of drag force and aerodynamic heating in the case of a blunt object mounted with various shapes of a forward-facing spike. The objective of Mohandas et al. [51] was to estimate drag force in presence of a stagnation spike through numerical simulations for different blunt objects. In these studies, they used two turbulence models to analyze the unsteadiness and to capture the actual dynamics in the flow field. Further,

numerical investigations by Srulijes et al. [52] were also focused to compute the drag force by accounting different spike shapes. Their results were in favor of a disc-shaped spike due to more drag reduction as compared to the spherical and biconical spikes for the same angle of attack. Their important remark was that the type of spike used has no effect on drag reduction for angles of attack more than 40°. Sahoo et al. [53] showed the dominance of spherical and blunt-tipped spike over the conical tipped spike for drag reduction. Similar results are reported by Mehta [54] for Mach 6, & Gerdroodbary and Hosseinalipour [55] for Mach 5.75 at 0° angle of attack. Shape optimization techniques were used by Ahmad and Quin [56] for a spiked body where they concluded that short rounded spikes have more potential for drag reduction than long pointed spikes. Masoud Kharati-Koopaee and Hesam Gazor [57] carried out CFD simulations using commercial solver ANSYS at a Mach number 5.75 for various lengths of the flat and spherical ended spikes. They concluded that the drag reduction is dependent on both the shape and size of the spike. By using a series of round-ended spikes mounted on a hemispherical body, Yadav et al. [58] noticed 44% reduction in drag and 30% reduction in heat flux. In this work, they considered the 5 species model with 17 elementary reactions along with k-ω model of turbulence using ANSYS. But only low stagnation temperatures were considered for those investigations.

In addition to the aerospike, energy deposition technique is also used by various researchers for drag reduction. Both steady and unsteady energy deposition methods were considered for this objective. Initially, Borzov et al. [59] performed experiments with various blunt objects to analyze the drag force reduction by depositing energy at an upstream location. Further, numerical investigations were performed by Levin and Terent'eva [60] for the steady energy addition. They computed the wave drag for a conical body having different cone angles. Further, Levin et al. [61] also worked for heat flux and drag reduction with steady energy deposition by considering the equilibrium model of the air flow. In similar studies, Vlasov et al. [62] proposed a correlation for the gas density at center of the deposited energy for supersonic flow. Later, numerical study by Riggins et al [63] showed that there is possiblities of 30% reduction in the wave drag for steady energy deposition in the hypersonic flow of Mach number 6.1 and 10. They also (Riggins [64]) presented variation in lift force and pitching moment for the different upstream locations of steady energy deposition. Braken et al. [65] produced an arc to virtually create an air-spike during their experiments in RPI HST tunnel for Mach number 10. They measured the drag force with an accelerometer force balance. Computations were also part of their studies to earn an insight about the gas dynamics of this drag reduction technique. Optimization for the maximum drag reduction using the energy deposition technique was an objective of Georgievskii and Levin [66]. The computations with the perfect gas assumption for air flow revealed

that higher drag reduction is possible with a larger amount of energy deposition. Experimental investigations were performed by Erdem et al. [67] for measurement of the drag force experienced by different cone-cylinder configurations as shown in Fig. 1.11 (a). They performed the simulation for the hypersonic flow of Mach 5 with and without energy deposition. They computed the drag force, as shown in Fig. 1.11 (b), for all considered shapes. They recommended to deposit a smaller amount of energy to re-

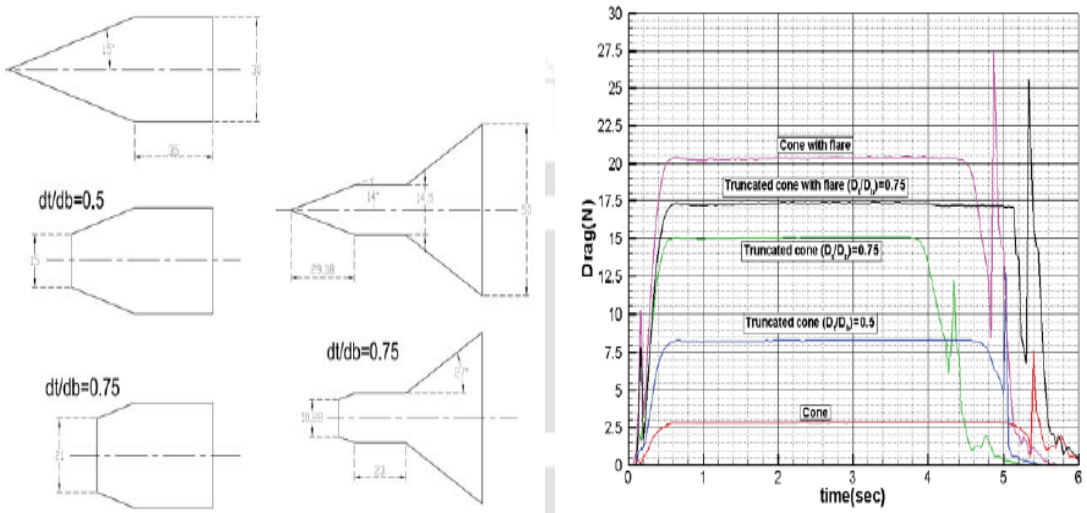

Figure 1.11: [Left] (a) Geometry for different cone configuration ([67]) and [Right] (b) Alteration of drag force for various cone shapes ([67]).

duce the drag force effectively for a space vehicle. Gutierrez and Poggie [68] performed numerical studies with a conical object for the drag reduction in supersonic flow of Mach number 3. In these explorations, off-axis and on-axis steady energy depositions were attempted while estimating the aerodynamic forces on the blunt object. Their results were in favor of the off-axis depositions for better drag reduction as compared to on-axis deposition. Later, Kulkarni et al. [69] conducted experiments with a blunt cone configuration for wave drag reduction by energy addition in HST2 hypersonic shock tunnel. Their focus was to execute energy deposition in the shock layer through the exothermic reactions between chromium platting and nascent oxygen from the post-shock flow. They claimed that there is 47% reduction in the drag for a 60° apex angle blunt cone. Later, Ganesh and Johan [70] performed optimization through numerical simulations for the steady-state energy deposition. They considered various strengths of energy spot, energy radius and upstream deposition lengths for obtaining the maximum drag reduction. Further, Knight [71] and Shneider et al. [72] presented a survey on steady and unsteady energy depositions which were performed with perfect gas assumption. But some researchers explored the same with the real gas model for air flow. In line with this, Siddesh et al. [73] studied the effect of energy deposition on

wave drag and power effectiveness. For this, they adopted a non-equilibrium reacting flow model having the potential to consider five species and eleven chemical elementary reactions. They gave a remark that, for higher freestream stagnation enthalpy, there is 74% reduction in the peak power effectiveness as compared to the lower enthalpy case. Later, hypersonic flow computations with eight species-based non-equilibrium model were performed by Dipankar et al. [74] as well. They compared the drag force reduction for the planet Earth with 5 species-based model and the planet Mars with 8 species-based model. It was concluded that the peak power effectiveness decreases for the Martian atmosphere as compared to the Earth atmosphere for same freestream condition.

In addition to the steady energy depositions, the unsteady energy deposition-based unstructured drag reduction technique is also reported by various researchers. The computational studies by Nedungadi and Lewis [75] were carried out to visualize the flow alterations caused by single blast-based deposition. They accounted for the various parameters on the strength of the low-density vortex and thus on the wave drag.

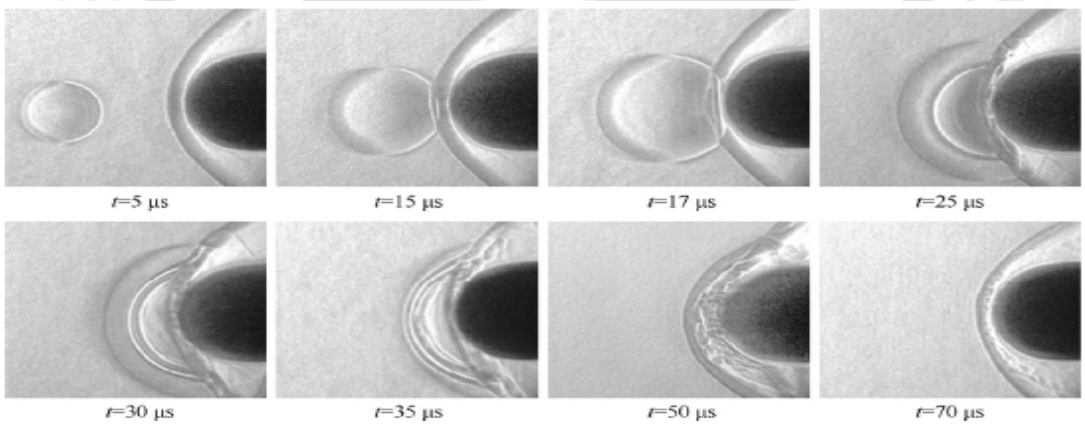

Fig. 5 Schlieren images.

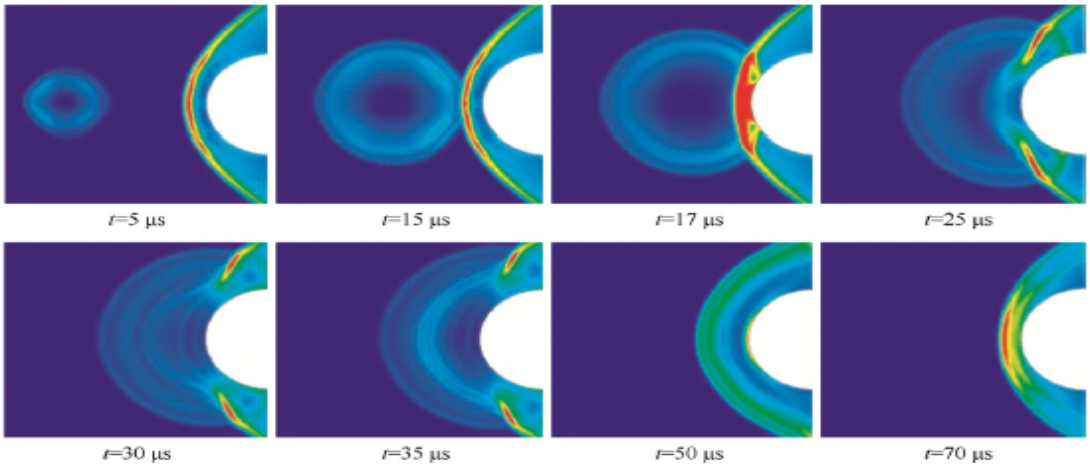

Figure 1.12: Flowfield alteration on a sphere by Yanji et al [78]

Kolesnichenko et al. [76] measured instantaneous drag force by depositing microwave discharge in the supersonic stream. Georgievsky and Levin [77] solved three-dimensional Euler equations numerically for periodic energy deposition upstream of a blunt and sharpened object in supersonic flows. Yanji et al. [78] adopted both experiments and computations for numerical periodic energy deposition to understand the property alterations at the stagnation point of the blunt-body. Their results marked that there is 50% decrease in the stagnation pressure which leads to 81% reduction in the wave drag for given freestream conditions. A novel method of microwave energy deposition-based drag reduction was studied by Knight et al. [79] for reacting flow of Mach 2.1 using 23 species and 238 chemical reactions-based solver. Kremeyer et al. [80] chose a blunted cone configuration to deposit energy pulse upstream along the stagnation streamline for different freestream Mach numbers. They mentioned that drag force reduction for the blunt cone is up to 96%. Here, the cone angle of the blunt object was also varied to arrive at optimum energy-saving efficiency of the energy pulse. Furthermore, Osuka et al. [81] had a cylindrical-flare model to show the flow field alterations by depositing repetitive laser pulses. They varied the nose shape and cone angle of the test model to obtain minimum impingement shock strength. Sakai [82] used different shapes of truncated cone model, as shown in Fig. 1.13, to estimate the drag force at supersonic flow conditions. They altered the truncation ratio of the model and deposited periodic energy pulse to obtain minimum drag. They stated that drag reduction depends on the strength of energy deposition, frequency parameter and the area of truncation. However, the moderate frontal surface area of the truncated cone was found desirable for better drag force reduction. Further, Sasosh et al. [83] performed experimental and numerical investigations to predict the efficiency of the blast wave on a spherical object. They also (Sasosh et al. [84]) extended the study of periodic energy deposition for the variable area truncated cone. The details of the interaction of the blast wave based on single pulse of energy deposition with the bow shock were reported by Taguchi et al. [85]. They performed parametric studies to obtain maximum drug reduction for a sphere by considering a perfect air model. As per their results drag force reduction is proportional to the Mach number for given strength of energy. Kianvashrad and Doyle [86] had the objective to show the non-equilibrium effect of laser energy deposition in supersonic flows through numerical simulation. They adopted three gas models viz a thermally perfect gas model, vibrationally non-equilibrium gas and full non-equilibrium gas. It was noted that the energy efficiency of the deposited pulse is independent of the type of model used. Kianvashrad et al. [87] extended the earlier studies for off-axis and on-axis discharge of energy pulse for all the three models. Periodic energy pulse was deposited by Kim et al. [88] to show the flow field alterations and drag signal for various frequencies

of the laser.

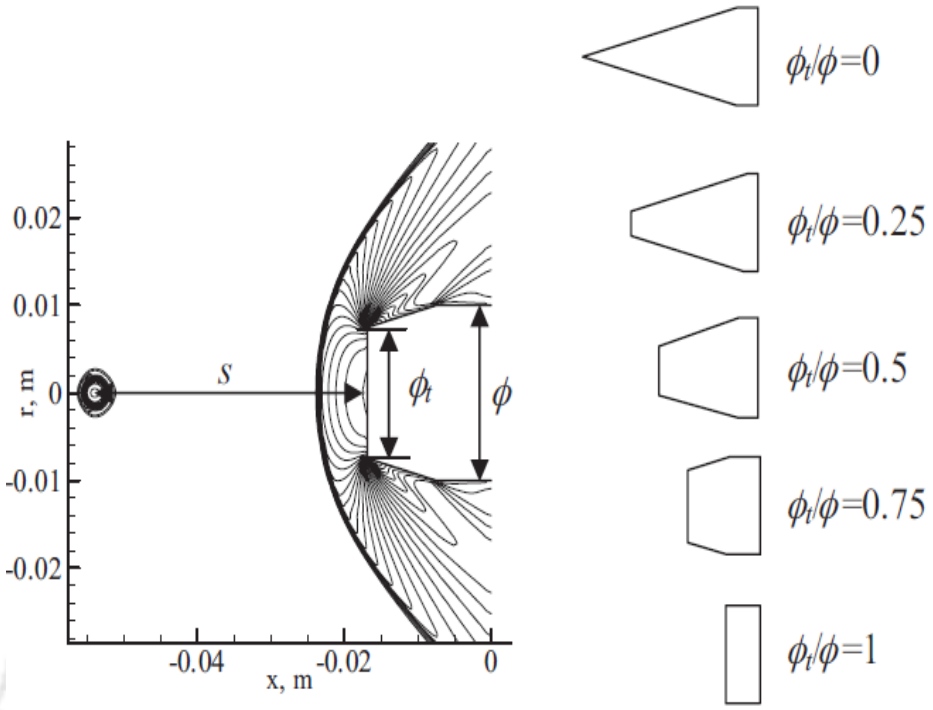

Figure 1.13: Geometry considered for the unsteady energy deposition by Sakai [82]

Further, Adelgren [89] performed experimental investigations to understand the effect of strength of energy spot with laser as a source of energy. Here, thermal lensing phenomenon was observed when the energy pulse interacts with the bow shock. Their results for a spherical object in supersonic flow showed that stagnation pressure reduces by 40%. Lashkov et al. [90] worked on various test models such as cylinder, hemisphere and cone to demonstrate the flow features by depositing microwave discharge along with stagnation streamline. They proposed that the vortex generation after the energy deposition is the main reason for the drag reduction and this condition is followed by every model considered. Later, Zheltovodov and Pimonov [91] carried out numerical simulations for the supersonic flow of Mach number 3.45. A sphere and a conical object were selected for the pulsed periodic energy deposition studies. They altered the source length to understand its effect on drag reduction. Kandala and Candler [92], [93] demonstrated the Edeny type IV Shock-Shock interactions with the help of unsteady pulsed energy deposition. They extended their studies for the flow with ionization as well and noticed the temporal variation in the plasma-based flow field. Sangtbai et al. [94] considered laser energy deposition upstream of different objects like sphere, cone and oblate spheroid. They compared the single and multiple blast waves for drag force reduction and concluded that there is 760%, 460% and 60% energy saving for the sphere, oblate spheroid and cone respectively. Further, the influence of baroclinic

vortex, which emerged due to energy deposition, was investigated by Yousuke Ogino et al. [95]. They arrived at a correlation for the calculation of vorticity and the vortex energy for the perfect gas flow model.

1.4.3 Shock-Shock (S-S) interactions

Earlier Edeny [96] classified six types of interaction of shocks and also presented correlations for the calculation of the heat transfer on the surface. However, Crawford [97] defined all interactions with the help of graphics. Bramlette [98] worked on the prediction of Type III and IV interactions in very simple way. They assumed no interaction required for the shear layer deflection which is required in the exact solution. Then the approximate solution was obtained by taking normalized pressure behind the normal shock in Type III and IV interaction. The predicted surface pressure showed that Type-IV interaction produces higher surface pressure as well as peak pressure as compared to the Type-III interaction. Moreover, Furumoto [99] analyzed the alteration of the pressure and heat flux for Type IV interaction using thermochemical non-equilibrium solver as well as with perfect gas solver. The simulation results showed that there is maximum drag and heat flux when the shock is normal to the body. Further, it was also found that the non-equilibrium real gas model reduces the peak pressure and heat as compared to the non-catalytic wall assumption. They also mentioned that the non-equilibrium model introduces some oscillations during Shock-Shock interaction. Holden [100] performed experiments to determine the aerothermal load in various S-S interactions for the hypersonic flow conditions of Mach 8 to 19 in the 48" and 98" shock tunnels. It was demonstrated that shock structure corresponding to the peak heat loads also suffers with the oscillation, due to which correct measurement of the heat load was not possible. But still the maximum heat load on the cylinder for the complex S-S interaction of Type IV was attempted for measurement. Further, Lind [101] worked to capture the unsteady behavior of the Type IV interaction in the hypersonic flow of Mach 8. Simulations were performed by considering the laminar flow and perfect gas model. Total variation diminishing (TVD) scheme was employed for the above consideration. For time integration in the solver, Euler implicit method was used and the viscous fluxes were centrally differentiated. They mentioned that unsteady behavior due to the S-S interaction is the function of the incident angle of the shock and shock strength, while higher shock strength leads to the oscillatory motion of the peak pressure on the surface of the body. Furthermore, Olejniczak [102] used these pressure oscillations to describe the interaction pattern for the double-wedge geometry. Through numerical simulations for laminar viscous flow for all Edeny Type S-S interactions (IV, V and VI) along with one new interaction.

Boldyrev et al. [103] studied S-S interaction in the hypersonic flow conditions for a cylindrical blunted object and wedge configurations in freestream Mach number of 6 & 16 for air and 6.6 for the carbon dioxide were considered in the study. According to the results, for laminar flow, heat transfer on the surface of the cylinder was in agreement with the theory but: the magnitude of heat transfer at stagnation was found higher than the theoretical calculation for the turbulent flow assumptions.

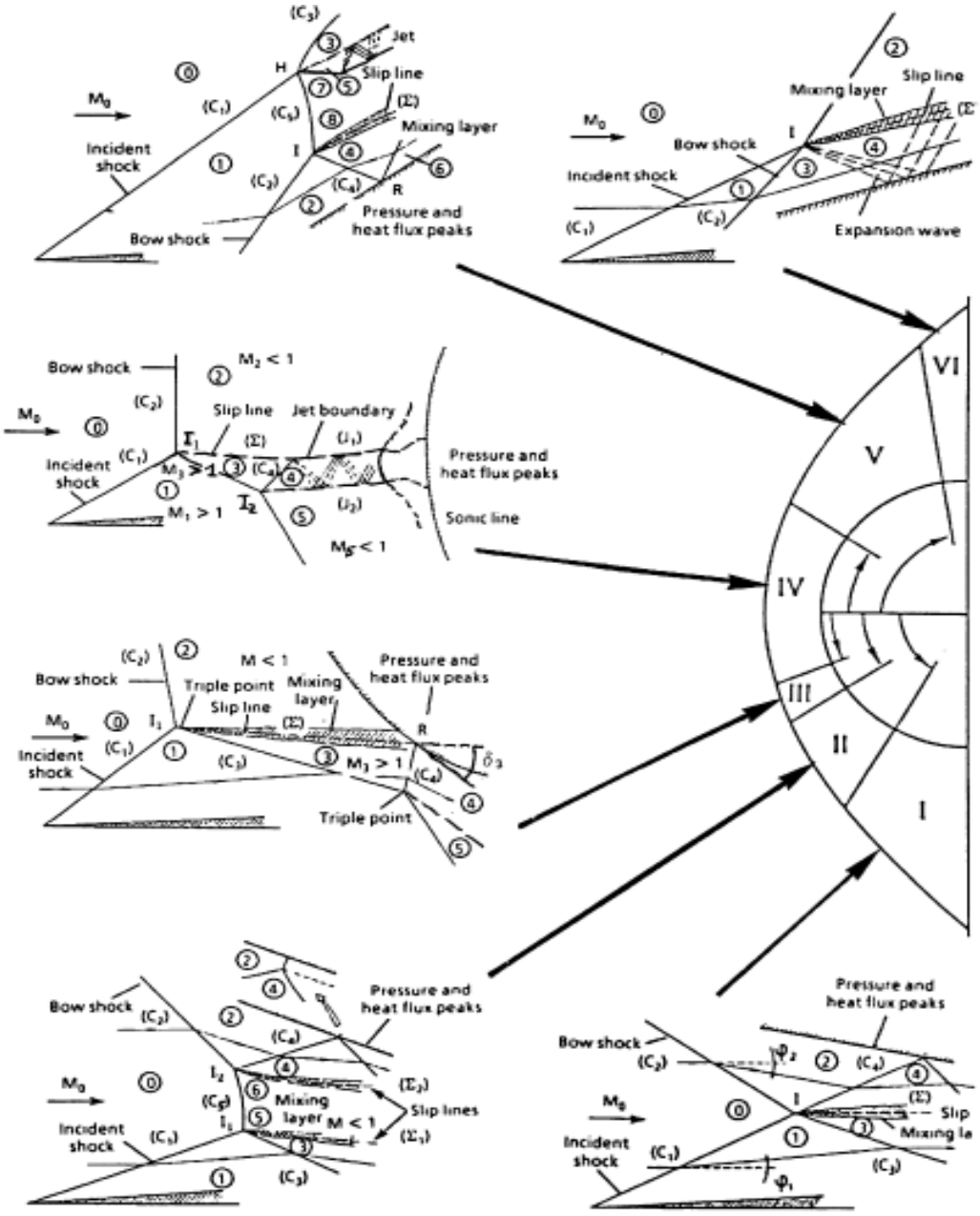

Figure 1.14: Possible Shock-Shock interaction on a high speed object [104]

It was also concluded that the heat flux in the S-S interaction region is higher for larger specific heat ratio gas. Moreover, the maximum heat flux was higher in CO_2 than air condition and these results are consistent with the theoretical results

of Edney. Grasso et al. [104] compute and show the all type of S-S interation on a high speed object as shown in Fig. 1.14. Afterwards, they compared the theoretical and experimental results for the Type III and IV S-S interactions. Their experimental investigations described the transition phenomenon of S-S interaction of Type IV from Type III. They also estimated the maximum/peak heat transfer without and with S-S interaction. They concluded that the aero-thermodynamic load on the body is maximum when the supersonic jet impinges on the surface or transmitted shock is normal to the body, which necessarily corresponds to the S-S interaction of Type IV. Moreover, it may be noted that S-S interaction for the spiked object or for other drag reduction techniques has not been investigated much. Therefore, current focus is on understanding the implication of S-S interaction on the performance of drag reduction techniques.

1.5 Objectives of the present study

In the reported literature, it is found that most of the studies about any drag reduction technique or for S-S interaction are related to non-reacting flows. Hence, it is desirable to revisit performance of a drag reduction technique in the reacting flow situation or with real gas effects. Therefore, the foremost objective of the present study is to develop a reacting compressible laminar flow solver. This solver must be higher-order accurate and should incorporate various species which perform chemical reactions in the high-temperature flow field. Moreover, this solver must handle reacting as well as non-reacting flow situations. In this regard, the temperature-dependent specific heats and transport properties are also essential for the investigations of low as well as high freestream stagnation enthalpy conditions.

Various researchers performed studies for the spike-based flow alteration and drag reduction technique. Most of the researchers worked with the governing parameters, like Mach number and spike length, while obtaining the wave drag reduction for the blunt object. But very few of them attended the calculation of the skin-friction drag and alteration in size of the dead-air region in presence of an aerospike spike. Also, such efforts for the wave drag and heat flux calculations are needed in the reacting flow environment. Thus, the current intention is to focus on flow alteration caused by a forward-facing spike in the reacting high-speed flows. It is well known that any spike separates the flow from its surface and reattaches the same on the object. Hence, knowledge of alterations in the separation and reattachment points, in terms of Shock Wave Boundary Layer Interaction (SWBLI), is highly desirable to address the effect of higher inlet stagnation enthalpies. Present studies are continued for different spike lengths and shapes of the spike tips to predict the drag force for blunt objects in real

gas flows. Further, a novel integration method of spike with counter flow jet technique is also presented to demonstrate a larger magnitude of drag reduction while using smaller spike.

High-speed vehicles encounter various types of Shock-Shock interactions during their flight. Many studies about the Shock-Shock interactions are available in the open literature, but most of those are related to the flat/blunt plate and ramp configuration. In addition to this, a calorically perfect gas model is commonly used for those findings. It is well known that shocks drastically increase temperature and pressure near the blunt surface. This increased temperature may trigger various chemical reactions and might change the shock interactions as well. Hence, for detailed quantification of the Shock-Shock interactions, reacting flow solver is used to study the hypersonic flow over the blunt object in presence of forward-facing spike. It is known that the mounting of a spike introduces an oblique shock which then interacts with the body shock. This interaction is responsible for alteration in the flow field near the object. In addition to that surface properties like pressure would also get altered and affect the drag force experienced by the object. Because of this, spikes of different lengths are accounted to introduce different Shock-Shock interaction patterns to study their effect on the flow field and blunt configuration. Along with this, changes in the size of the recirculation bubble, stationed in the vicinity of the stagnation region, are also investigated for the reacting gas flow in the presence of different Shock-Shock interaction patterns to understand the effect on drag force.

Numerous studies have been noted for unsteady and steady energy deposition-based drag reduction techniques. Most of them are based on wave drag or power effectiveness calculations for different locations of energy deposition or strength. Moreover, those studies are either for non-reacting flow or reacting flow but for lower enthalpy conditions [61, 63]. Therefore present studies are planned for high enthalpy flowfield. Further, unsteady energy deposition has a quite complex mechanism of drag reduction. In this process, the formation of a low-density vortex by the interaction of deposited pulse with the bow shock is reported as a leading factor for the reduction of surface properties. Thus, before the interaction of blast with bow shock, it is essential to carry out a detailed analysis of changes in density, pressure, temperature and species mass fraction inside the deposited pulse along with its size. These changes should be investigated for the reacting as well as non-reacting gas flows to demonstrate the real gas effect. Similar effects with change in energy deposition locations and its strength are to be studied. Comparison between steady and energy deposition techniques is also planned to distinguish their drag reduction mechanisms, associated amount of drag reduction and effectiveness of the deposited energy.

Obviously, single energy pulse deposition is an effective method for drag reduction,

but for a very short time interval. Therefore, periodic pulse energy deposition is needed to be addressed to achieve drag reduction for a prolonged period. But in his case, multiple or repeated blast waves would interact with the bow shock to form a low-density region around the blunt surface. It is essential to quantify the efficiency of deposited energy for a single pulse as well as multiple pulses. Further, higher freestream stagnation enthalpies and different pulsed energy deposition locations are to be accounted to discriminate the changes in the presence of single pulse and periodic pulse depositions.

In line with the above discussion following are the milstones to achieve the desire objectives.

1. Development of an unstructured finite volume Navier-Stokes reacting compressible flow solver which can account five species and eleven elementary chemical reactions.
2. Validation of the in-house developed 2-D axisymmetric flow solver with different literature reported test cases.
3. Aerothermodynamic analysis of the spike-based drag reduction technique for perfect and non-equilibrium gas flows for various lengths and different freestream stagnation enthalpies.
4. Study of Shock-Shock interactions and their effect on the flow field while achieving drag reduction for spiked configurations.
5. Prediction of the drag force in case of different spike shapes and their integration with counter flow jet.
6. Assessment of unsteady energy deposition-based drag reduction technique for various energy deposition locations, energy strengths and different freestream enthalpy conditions.

Organization of thesis

1. Chapter 2 is dedicated to the numerical formulation of the in-house developed reacting compressible flow solver.
2. In chapter 3, aerothermodynamic analysis of the spike-based drag reduction technique for perfect and non-equilibrium gas flows is presented for various spike lengths.
3. Chapter 4, deals with Shock-Shock interactions for the spiked object to benchmark the drag reduction criteria.

4. Chapter 5, covers investigations with different shapes of the spike tips and their integration with counter jet injection for drag reduction in high enthalpy hypersonic flows.

5. Assessment of unsteady energy deposition based drag reduction technique for various deposition locations and energy strengths is the part of the chapter 6. This chapter also compares the effectiveness of steady and unsteady energy deposition techniques for reacting flows. Further, relative advantage of periodic energy deposition over single pulsed energy deposition is evaluated in the same chapter.

6. The thesis ends with conclusions and scope of future in chapter 7.

CHAPTER 2

NUMERICAL METHODOLOGY

This chapter deals with the numerical formulation of the present reacting compressible flow solver which accounts five species (O_2, O, N_2, N and NO) and eleven elementary chemical reactions. Detailed procedure of cell-centered finite volume method (FVM) and its implementation in the present solver is also explained here. Further, computations of convective and viscous fluxes along with all the boundary conditions are part of this chapter. Moreover, the solution procedure of various types of gas models, temporal discretization method and the treatment of source terms are also emphasized in detail.

2.1 Governing equations

The governing equations for the calorically perfect gas assumption are the mass, momentum and energy equations which are also known as the Navier-Stokes (N-S) equations for compressible flow. This assumption also needs support of the equation of state (EOS) as a closure. But for reacting gas flow model, species continuity equations are also needed along with the N-S equation for the laminar flow simulations. This consideration adds extra terms of convective species fluxes which are due to the absolute velocity of the given species. Further, species diffusion fluxes should also be addressed which are due to the mass diffusion velocity of the species. The energy equation also needs to be modified by adding the partial enthalpy of each species which arises due to the concentration gradient and diffusion terms of the species. Moreover, consideration of different reactions should also be part of combined equations to account for the change in concentration of the species due to their participation in chemical reactions. Therefore it can be seen that complexity of the solver increases when we account for chemical reactions. Hence, the combined form of species continuity equa-

tions with chemical source terms and the Navier-Stokes equations for two dimensional axisymmetric laminar reacting flow solver is given below:-

$$\frac{\partial U}{\partial t} + \frac{\partial E_c}{\partial x} + \frac{\partial F_c}{\partial y} + \alpha S_I = \frac{\partial E_v}{\partial x} + \frac{\partial F_v}{\partial y} + \alpha S_v - S \tag{2.1}$$

Here, U is the conservative variables vector, E_c and F_c are the convective/inviscid fluxes in x and y direction respectively, α is a numeric constant which is one for axisymmetric cases and zero for the two-diamensional cases and S_I is source term considered for the inviscid axisymmetric cases. Further, E_v and F_v are the viscous fluxes in the x and y directions, while S_v is the source term considered for the viscous axisymmetric cases. Reaction effect introduces an extra source term which is mentioned as S. These terms are given as follows,

$$U = \begin{bmatrix} \rho \\ \rho u \\ \rho v \\ \rho E \\ C_1 \\ . \\ . \\ C_{N-1} \end{bmatrix}, E_c = \begin{bmatrix} \rho u \\ \rho u^2 + p \\ \rho uv \\ (\rho E + p)u \\ uC_1 \\ . \\ . \\ uC_{N-1} \end{bmatrix}, F_c = \begin{bmatrix} \rho v \\ \rho uv \\ \rho v^2 + p \\ (\rho E + p)v \\ vC_1 \\ . \\ . \\ vC_{N-1} \end{bmatrix}, E_v = \begin{bmatrix} 0 \\ \tau_{xx} \\ \tau_{xy} \\ u\tau_{xx} + v\tau_{xy} - q_x - \sum_{i=1}^{N} h_i C_i \overline{u}_{\ i} \\ -C_1 \overline{u}_{\ 1} \\ . \\ . \\ -C_{N-1} \overline{u}_{\ N-1} \end{bmatrix},$$

$$\mathrm{F}_v = \begin{bmatrix} 0 \\ \tau_{xy} \\ \tau_{yy} \\ u\tau_{xy} + v\tau_{yy} - q_y - \sum_{i=1}^{N} h_i C_i \overline{v}_{\ i} \\ -C_1 \overline{v}_{\ 1} \\ . \\ . \\ -C_{N-1} \overline{v}_{\ N-1} \end{bmatrix}, S_I = \frac{1}{y} \begin{bmatrix} \rho v \\ \rho uv \\ \rho v^2 \\ (\rho E + p)v \\ vC_1 \\ . \\ . \\ vC_{N-1} \end{bmatrix},$$

$$S_v = \frac{1}{y}\begin{bmatrix} 0 \\ \tau_{xy} - \frac{2}{3}y\frac{\partial(\mu v/y)}{\partial x} \\ \tau_{yy} - \tau_{\theta\theta} - \frac{2}{3}\mu(\frac{v}{y}) - \frac{2}{3}y\frac{\partial(\mu v/y)}{\partial y} \\ u\tau_{xy} + v\tau_{yy} - q_y - \frac{2}{3}\frac{\mu v^2}{y} - \frac{2}{3}y\frac{\partial(\mu v^2/y)}{\partial y} - \frac{2}{3}y\frac{\partial(\mu uv/y)}{\partial x} - \sum_{i=1}^{N} h_i C_i \overline{v}_i \\ -C_1\overline{v}_1 \\ . \\ . \\ -C_{N-1}\overline{v}_{N-1} \end{bmatrix} -$$

Here, the state or physical variables are density (ρ), velocity with two components u and v in x and y directions respectively, pressure (p), temperature (T), total internal energy (E) and internal energy (e). Total energy is calculated as, $e + \frac{1}{2}(u^2 + v^2)$ where $e = \sum_{i=1}^{N} e_i \frac{C_i}{\rho MW_i}$ and e_i represents the molar internal energy of i^{th} species and can be calculated as $h_{fi}^0 + \int_{T_R}^{T} C_{pi} dT - R_u T$. Expression for the calculation of pressure is given by Eq(2.2)

$$p = R_u T \sum_{i=1}^{N} \frac{C_i}{MW_i} \tag{2.2}$$

Presently temperature is calculated from the known total energy of the control volume using Eq(2.3) iteratively with the help of Newton-Raphson method.

$$\rho e = \sum_{i=1}^{N} \left[\frac{C_i}{MW_i} \left(\int_{T_R}^{T} C_{pi}\, dT + h_{fi}^0 \right) \right] - p \tag{2.3}$$

Here, C_i, MW_i, h_{fi}^0 and C_{pi} are the mass concentration, molecular weight, heat of formation and molar specific heat at constant pressure for a particular species i respectively; while T_R is the reference temperature (298.5 K). In the present flow solver, components of shear stress are calculated as

$$\tau_{xx} = \mu\left(\frac{4}{3}\frac{\partial u}{\partial x} - \frac{2}{3}\frac{\partial v}{\partial y}\right), \tau_{xy} = \mu\left(\frac{\partial u}{\partial y} + \frac{\partial v}{\partial x}\right), \tau_{yy} = \mu\left(\frac{4}{3}\frac{\partial v}{\partial y} - \frac{2}{3}\frac{\partial u}{\partial x}\right), \tag{2.4}$$

$$\tau_{\theta\theta} = \mu\left(-\frac{2}{3}\left(\frac{\partial u}{\partial y} + \frac{\partial v}{\partial x}\right) + \frac{4}{3}\frac{v}{y}\right)$$

Here, dynamic viscosity (μ) and specific heats (C_p, C_v) are calculated by the polynomial fit of temperature as described in the literature [105]. The terms h_i over here is the molar specific enthalpy of i^{th} species. Heat flux has two components as q_x and q_y, as mentioned in column E_v and F_v and these are calculated by the expression given by $k\frac{\partial T}{\partial x}$ and $k\frac{\partial T}{\partial y}$ respectively. Here, conductivity (k) is evaluated by the temperature based polynomial as mentioned in open literature [105]. The mass diffusion velocity in x direction, $\tilde{u}_i$, and in y direction, $\tilde{v}_i$, are calculated by scalar continuity equation using Fick's law of mass diffusion as:-

$$\tilde{u}_i = -\frac{D_{im}}{Y_i}\frac{\partial Y_i}{\partial x}, \tilde{v}_i = -\frac{D_{im}}{Y_i}\frac{\partial Y_i}{\partial y} \tag{2.5}$$

Here, Y_i is the mass fraction of the i_{th} species. The value of the diffusion coefficient (D_{im}) is dependent on the size of species. But for multispecies mixture where one component is present in large amount (like in air, nitrogen species (N_2) is abundant), diffusion coefficient for the minor species can be neglected. This assumption reduces the complexity and error of descretisation as well as reudces the computational time. Thus present solver includes diffusion coefficient of only nitrogen species (N_2) which is taken as $5 \times 10^{-5} m^2/s$ for a fixed temperature condition. Further, procedure to treat the chemical reactions is presented in the following subsections.

2.2 Chemical kinetics

For the consideration of chemical reactions in the flow field, mixture of five species and eleven elementary reactions is accounted in the present solver. These species are O_2, O, N_2, N and NO. Chemical reactions considered are nine dissociation reactions (given below),

$$O_2 + M \rightleftharpoons 2O + M(N), \quad N_2 + M \rightleftharpoons 2N + M(O), \quad NO + M \rightleftharpoons N + O + M(O_2),$$
$$N + N_2 \rightleftharpoons N + N + N, \quad O_2 + O \rightleftharpoons 2O + O, \quad O_2 + O_2 \rightleftharpoons 2O + O_2,$$
$$O_2 + N_2 \rightleftharpoons 2O + N_2, \quad N_2 + N_2 \rightleftharpoons 2N + N_2, \quad NO + M \rightleftharpoons N + O + M(O).$$

and two exchange or Zel'dovich reactions (as given below)

$$O + N_2 \rightleftharpoons N + NO, \quad O + NO \rightleftharpoons N + O_2.$$

Considaration of these chemical reactions introduces an extra of source term (S) in equation 2.1, which is given as

$$S = \begin{bmatrix} 0 \\ 0 \\ 0 \\ 0 \\ S_1 \\ . \\ . \\ S_{N-1} \end{bmatrix}$$

Here, S_j is the rate of change of molar concentration for each j^{th} species in the chemical reactions. A set of N_R elementary reversible reactions involving N species may in general be represented as:-

$$\sum_{j=1}^{N} \nu_{ij}^{'} n_j \rightleftharpoons \sum_{j=1}^{N} \nu_{ij}^{''} n_j \tag{2.6}$$

where i = 1,2,...,$\mathrm{N_R}$ and $\nu_{ij}^{'}$ and $\nu_{ij}^{''}$ are the stoichiometric coefficients for species j appearing as a reactant in the i^{th} forward and backward reactions respectively. Further, $n_j = \frac{C_j}{MW_j}$ is the molar concentration for species j. The rate of change of molar concentration of species j is then given by summing up the changes due to all reaction steps,

$$S_j = MW_j \sum_{i=1}^{N_R} \left[\left(\nu_{ij}^{''} - \nu_{ij}^{'} \right) \left(k_{fi} \prod_{l=1}^{N} n_l^{\nu_{il}^{'}} - k_{bi} \prod_{l=1}^{N} n_l^{\nu_{il}^{''}} \right) \right] \tag{2.7}$$

Here, k_{fi} and k_{bi} are the forward and backward reaction rate constants which are calculated using the Arrhenius rate expression

$$k_i = A_i T^{m_i} e^{\frac{-E_i}{R_u T}} \tag{2.8}$$

Where E_i represents the activation energy, while A_i and m_i are constants. The reactions and the corresponding rate constants are given in Table 2.1.

Table 2.1: Chemical reactions and specific reaction-rate constants for chemical reaction calculations [106]

No.	Forward reaction	k_{fi} (cm^3/mole sec)	k_{bi} (cm^3/mole sec) or (cm^6/$mole^2$ sec)
1	$O_2 + M \rightleftharpoons 2O + M(N)$	$3.6 \times 10^{18} T^{-1.0} e^{-5.95\times10^4/T}$	$3.0 \times 10^{15} T^{-0.5}$
2	$N_2 + M \rightleftharpoons 2N + M(O)$	$1.9 \times 10^{17} T^{-0.5} e^{-1.13\times10^5/T}$	$1.1 \times 10^{16} T^{-0.5}$
3	$NO + M \rightleftharpoons N + O + M(O_2)$	$3.9 \times 10^{20} T^{-1.5} e^{-7.55\times10^4/T}$	$1 \times 10^{20} T^{-1.5}$
4	$O + NO \rightleftharpoons N + O_2$	$3.2 \times 10^{9} T^{1} e^{-1.97\times10^4/T}$	$1.3\times10^{10} T^{1.0} e^{-3.58\times10^3/T}$
5	$O + N_2 \rightleftharpoons N + NO$	$7.0 \times 10^{13} e^{-3.8\times10^4/T}$	1.56×10^{3}
6	$N + N_2 \rightleftharpoons N + N + N$	$4.085\times10^{22} T^{-1.5} e^{-1.13\times10^5/T}$	$2.27 \times 10^{21} T^{-1.5}$
7	$O_2 + O \rightleftharpoons 2O + O$	$9.0 \times 10^{19} T^{-1.0} e^{-5.95\times10^4/T}$	$7.5 \times 10^{16} T^{-0.5}$
8	$O_2 + O_2 \rightleftharpoons 2O + O_2$	$3.24 \times 10^{19} T^{-1.0} e^{-5.95\times10^4/T}$	$2.7 \times 10^{16} T^{-0.5}$
9	$O_2 + N_2 \rightleftharpoons 2O + N_2$	$7.2 \times 10^{18} T^{-1.0} e^{-5.95\times10^4/T}$	$6 \times 10^{15} T^{-0.5}$
10	$N_2 + N_2 \rightleftharpoons 2N + N_2$	$4.7 \times 10^{18} T^{-0.5} e^{-1.13\times10^5/T}$	$2.72 \times 10^{16} T^{-0.5}$
11	$NO + M \rightleftharpoons N + O + M(O)$	$7.8 \times 10^{22} T^{-1.5} e^{-7.55\times10^4/T}$	$2.0 \times 10^{20} T^{-1.5}$

2.3 Finite volume method

Most CFD solvers use Finite volume method (FVM) for the simulation of fluid flow problems. This method is necessarly a procdure to handle single or system of partial differential equations (PDE) in form of algebraic eqations. At first, this method devides the whole computational domain into number of small control volume (CV) or cells. This subdivision eliminates the non-overlapping of the smaller CVs. Now, each control volume is used for the application of Gauss divergence theorem as it converts volume integral into the surface integral. Further, these surface integrals are solved as fluxes at the face at each finite volume. Due to this procedure, FVM is accurate and compitable with the structured as well as unstructrued meshes. Also, it is quite easier to deal with complex geometries using FVM. According to the solution procedure, this method can be devided in to two groups i.e. cell vertex approach and cell centred approach. In cell vertex approach, all values of variables are stored at the computational node or corner point of that control volume. However, in cell centered approach it is stored at the centroid point of that computational cell. Cell centred method is more accurate and quite easy to implement, therefore this approach is adopted for the present computations.

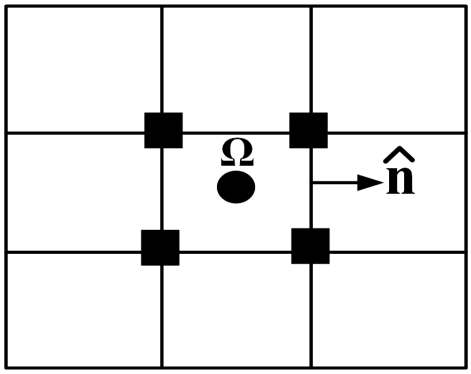

Figure 2.1: Representation of cell centered FVM scheme

2.4 Theoretical formulation of cell centered FVM

The governing equation for non-equilibrium flow, as given by Eqn 2.1, can be written as:

$$\frac{\partial U}{\partial t} = -\left(\frac{\partial (E_c - E_v)}{\partial x} + \frac{\partial (F_c - F_v)}{\partial y} + \alpha(S_I - S_v) + S\right)$$

Integrating the above equation we get:-

$$\int_\Omega \frac{\partial U}{\partial t} \mathrm{d}\Omega = -\int_\Omega \left(\frac{\partial (E_c - E_v)}{\partial x} + \frac{\partial (F_c - F_v)}{\partial y} + \alpha(S_I - S_V) + S\right) \mathrm{d}\Omega \tag{2.9}$$

Above Eqn 2.9 represents the integral form of 2-D axisymmetric N-S equation of which left hand side term shows the variable vector and right hand side term denotes the flux vectors and source terms. Now, let's consider only left hand side (LHS) of Eqn 2.9:-

$$LHS = \int_\Omega \frac{\partial U}{\partial t} d\Omega = \frac{\partial}{\partial t} \int_\Omega U d\Omega$$

$$LHS = \frac{d}{dt}(\bar{U}\Omega)$$

$$LHS = \Omega \frac{d}{dt}\bar{U} \tag{2.10}$$

Here, $\bar{U} = \frac{\int_\Omega U d\Omega}{\int_\Omega d\Omega}$.

Taking terms of the right hand side (RHS) of Eqn 2.9:-

$$RHS = \int_{\Omega} \Big(\frac{\partial (E_c - E_v)}{\partial x} + \frac{\partial (F_c - F_v)}{\partial y} + \alpha (S_I - S_v) + S \Big) d\Omega \tag{2.11}$$

By help of ∇ operator, above integral form of equation can be rewritten in divergence form as:-

$$RHS = \int_{\Omega} \Big(\nabla . (H_c - H_v) + \alpha (S_I - S_v) + S \Big) d\Omega$$

Here, $H_c = [E_c \ F_c]$, $H_v = [E_v \ F_v]$ and $\nabla = [\frac{\partial}{\partial x} \ \frac{\partial}{\partial y}]$.
Above formulated equation can be rewritten as:-

$$\int_{\Omega} \Big(\nabla . (H_c - H_v) \Big) d\Omega = - \int_{\Omega} \Big(\alpha (S_I - S_v) + S \Big) d\Omega \tag{2.12}$$

Applying discrete Gauss divergence theorem to the Eqn 2.12:-

$$RHS = \int_{\Omega} \nabla . (H_c - H_v) d\Omega = \int_{S} (H_c - H_v) . \hat{n} dS$$

$$\int_{S} (H_c - H_v) . \hat{n} \, \mathrm{d}S = \sum_{J=1}^{n_f} (H_c - H_v)_J . \hat{n}_J \, \Delta S_J = \sum_{J=1}^{n_f} (H_{c_\perp} - H_{v_\perp})_J \, \Delta S_J \tag{2.13}$$

Here,

$$\hat{n} = [n_x, n_y]$$

Where, $\hat{n}$ is the unit normal vector pointing outward of the control volume. The components of the this unit normal vector in x and y directions are n_x and n_y respectively. Here, ΔS_J is treated as the length of the face of control volume for the two-dimensional case and $H_{c\perp}$ and $H_{v\perp}$ are the inviscid and viscous normal fluxes crossing the faces of a CV. These terms can be written as:

$$\mathrm{H}_{c_\perp} = \begin{bmatrix} \rho u_\perp \\ \rho u u_\perp + p n_x \\ \rho v u_\perp + p n_y \\ (\rho e + p) u_\perp \\ C_1 u_\perp \\ . \\ . \\ C_{N-1} u_\perp \end{bmatrix}, \mathrm{H}_{V_\perp} = \begin{bmatrix} 0 \\ n_x \tau_{xx} + n_y \tau_{xy} \\ n_x \tau_{yx} + n_y \tau_{yy} \\ n_x \Theta_x + n_y \Theta_y \\ 0 \\ . \\ . \\ 0 \end{bmatrix}$$

During flux calculations, the contravariant velocity $u_\perp$ is used which can be written in terms of the normal vector as:-

$$u_\perp = u.n_x + v.n_y$$

The energy equation includes work done by shear force and heat transfer (q_x and q_y) for the non-reacting considaration. But for the reacting condition, the temperature effect on chemical reaction may add the effect of partial enthalpy transport of species in the heat flux. This term of energy flux is mainley due to the mass diffusion of the different species. It might have significant effect on the total enthalpy as well as flowfield and should not be neglected. Thus energy equation for the reacting simulation also includes the enthalpy transport of each species. Hence the corresponding terms can be written as:-

$$\begin{aligned} \Theta_x &= u\tau_{xx} + v\tau_{xy} - q_x - \sum_{i=1}^{N} h_i C_i \overline{u}_{\ i} \\ \Theta_y &= u\tau_{yx} + v\tau_{yy} - q_y - \sum_{i=1}^{N} h_i C_i \overline{v}_{\ i} \end{aligned} \tag{2.14}$$

The source terms, as mentiond in the right hand side of Eqn (2.12), can be treated as:-

$$\int_\Omega \Big(\alpha(S_I - S_v) + S \Big) d\Omega = \alpha(\Omega \overline{S} + \Omega \overline{S}_c) \tag{2.15}$$

where,

$$\overline{S} = \overline{S}_I - \overline{S}_v$$

Therefore, from Eqn (2.10), (2.13) and (2.15), the final integral form of the gov-

erning equation (2.9) is:-

$$\Omega_i \frac{d\overline{U}_i}{dt} + \sum_{J=1}^{n_f} (H_{c\perp J} - H_{v\perp j})\, \Delta S_J + \Omega_i \overline{S}_{ci} + \alpha \Omega_i \overline{S}_i = 0$$

$$\frac{d\overline{U}_i}{dt} = -\frac{1}{\Omega_i} \sum_{J=1}^{n_f} (H_{c\perp J} - H_{v\perp j})\, \Delta S_J - \overline{S}_{ci} - \alpha \overline{S}_i = R(\overline{U}_i) \tag{2.16}$$

2.5 Spatial discretization

The Eqn 2.16 represents semi-desretized form of the reacting comppressible flow solver. This descritization procedure arrives at a residual term $R(\overline{U}_i)$ as mentioned in Eqn 2.16. For the calculation of this residual term, it is nessesary to evaluate the inviscid and viscous fluxes at the face of the control volume. It also needs the computations of time marching and the treatment of source terms. Thus, the accuracy of present solver solely depends on the startegy of discretisation of these terms which are mentaioned in the following subsections.

2.5.1 Convective flux computation schemes

Non-linear hyperbolic nature of the present governing equations introduces several discontinuties in the solutions even though initial data is continuous. However, these discontinuities can be captured with the help of various shemes which are based on the direction of propagation of information in the flow field. This is well known as the upwind scheme. Hence, present cell centered FVM formulation uses different types of upwind schemes for the calculation of the convective or inviscid fluxes. In present solver, four different types of schemes are used which are AUSM [107], AUSM+ [108], Van Leer [109] and Rusanov [110] as listed in the Appendix. Considaration of various chemical reactions leads to changes in the species during flow. Thus, these schemes are well formulated and descretized to adopt for the reacting gas as well non-reacting gas flows.

2.5.2 Solution reconstruction for higher-order spatial accuracy

The flow variables to be assigned on right and left sides of the faces of a CV is a requirement of the upwind scheme. For the first order spatial accuracy, these flow variables are evaluated by extrapolating the cell centroidal values of left and right side of the cell faces. But, accuracy of the solution obtained by first order schemes is lower.

Therefore, higher order spatial descretization is incarporated in present solver to enhance the accuracy of the solutions. Herein, second-order accurate is obtained through piece-wise linear reconstruction technique [111]. In this reconstaruction method, the solution is assumed to be piece wise linearly distributed over the control volume. The calculation procedure for this method is described below:-

$$U_L = U_{I_{cell}} + \psi(\nabla U_{I_{cell}}.\vec{r}_L)$$
$$U_R = U_{J_{cell}} + \psi(\nabla U_{J_{cell}}.\vec{r}_R)$$

Here, U_L and U_R are the values of variables at left and right states respectively, ψ is a limiter function, and $\nabla U_{I_{cell}}$ is the derivative of U at the cell centroid I, which can be detremined as:-

$$U_{I_{cell}} = \left[\frac{\partial U}{\partial x}, \frac{\partial U}{\partial y}\right]^T$$

Further, $\vec{r}_L$ and $\vec{r}_R$ represent the vectors pointing from the cell-centroid towards the face centroid as presented in Fig.2.2. Demerit with considaration of the second order solutions is the oscillation near the high gradient locations or near the discontinuity such as in regions with shock. This phenomena is refferd as the monotonicity loss which can be limited by incorporating the limiter functions (ψ). Limiter function produces non-increasing maxima and non-decreasing minima and restricts to generate new local extrema. It ascertains that, reconstructed left and right flow variables do not exceed the maximum and minimum of the corresponding cell centroidal values. In the present solver, Venkatakrishnan's limiter is incorporated as it assures better convergence along with the oscillation free solution. According to this methodology the limiter function is calculated as:-

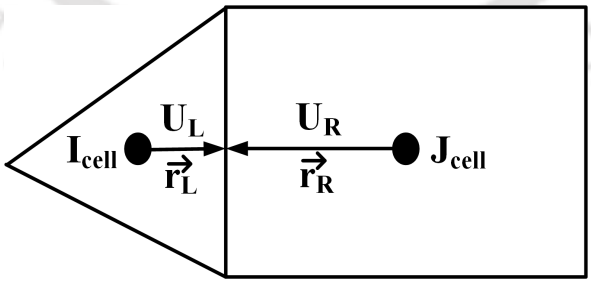

Figure 2.2: Linear reconstruction for the cell centered scheme

$$\psi = \begin{cases} \left[\frac{(\Delta_{1,max}^2+\epsilon^2)\Delta_2+2\Delta_2^2\Delta_{1,max}}{\Delta_{1,max}^2+2\Delta_2^2+\Delta_{1,max}\Delta_2+\epsilon^2}\right] & \text{if } \Delta_2 > 0 \\ \left[\frac{(\Delta_{1,min}^2+\epsilon^2)\Delta_2+2\Delta_2^2\Delta_{1,max}}{\Delta_{1,max}^2+2\Delta_2^2+\Delta_{1,max}\Delta_2+\epsilon^2}\right] & \text{if } \Delta_2 < 0 \\ 1 & \text{if } \Delta_2 = 0 \end{cases}$$

where $\Delta_{1,max} = U_{max} - U_{I_{cell}}$ and $\Delta_{1,min} = U_{min} - U_{I_{cell}}$. Here, U_{max} and U_{min} are the maximum and minimum values of all surrounding cells J, including the cell I itself, and are expressed as:-

$$U_{max} = max(U_{I_{cell}}, max_J U_{J_{cell}})$$
$$U_{min} = min(U_{I_{cell}}, min_J U_{J_{cell}})$$

The quantity Δ_2 is determined as $\Delta_2 = \nabla U_{I_{cell}}.\vec{r}_L$. Further, the term ϵ^2 can be generalised as $\epsilon^2 = (K\Delta h)^3$. Here, K is a constant of order one (generally taken as 2) and Δh is square root of area in two-dimensional cases.

2.5.3 Calculation of viscous fluxes

The evaluation of the viscous flux is essential for the treatment of residual term as appeared in the Eqn 2.16. Although descritisation procedure of convective and viscous fluxes is entireley diifferent but the considered control volume, for descritization, is kept as same. This improves the consistency and simplicity of flux calculation as well as descretization structure. As the viscous flux is calculated at the face of the cell, so all values of variables and their single derivatives should be known at the cell face. In the present FVM, flow variables at cell face are calculated by simply averaging right and left cell values, which can be formulated as:-

$$U_{IJ_{face}} = \frac{1}{2}(U_{I_{cell}} + U_{J_{cell}})$$

The procedure for calculation of gradient of the flow variable is based on Gauss divergence theorem [112]. Initialy all dervatives are calculated at the cell centre and then these values are assigned to the corresponding node points of the cell by area weighted averaging. After this, the node values are averaged to get the gradient at the respective faces. This process of handling of derivatives is essential to avoid the decoupling of evaluated gradients at the boundaries as it usually happens in the simple cell averaging method.

2.6 Boundary conditions

Well posed problem requires correct and proper implementation of the boundary condition to the computational control volume. Otherwise it may lead to the incorrect or non-physical results. Thus, this subsection describes the different boundary conditions and their incarporation startegy in the present solver.

2.6.1 Free-slip wall or symmetry boundary

As the name implies "free-slip wall" means there is free movement of the fluid over the slippery surface. This happens because of the absence of friction on the surface which leads to zero frictional or viscous or shear force on the inviscid wall. Hence, non-zero velocity should be ensured along the wall surface which is also known as tangential component ($\vec{V}_{II}$) of the velocity. This type of wall should be impermeable, so normal component of the velocity ($\vec{V}_{\perp}$) at inviscid wall must be zero. This can be summarised as:-

$$\vec{V}_{II} \neq 0 \text{ and } \vec{V}_{\perp} = 0$$

Similar strategy is also applied for the symmetry wall boundary condition. As there no flux crosses the boundry then normal velocity remains zero at symmetry boundary condition. Thus the inviscid wall and symmetry boundary conditons are same but their physical significance is different. The implementaion of these boundary conditions is done by the mirror or ghost cell approach which is described below.

Mirror or Ghost cell approach

This approach utilises a dummy or ghost cell at the symmetry or inviscid wall boundary for the handling of normal velocity ($u_{\perp}$). All other flow properties like pressure, temperature, enthalpy, entropy etc are taken from the adjecnt interior cell near the boundary of the computational domain and are assigned to the ghost cell. This procedure permits the evalution of the convective or inviscid fluxes at the wall boundary and thus accounts the propagation of wave. This technique is repersented in Fig.2.3 and can be formulated as below:-

$$u_{\perp_G} = -u_{\perp_I}$$
$$u_{II_G} = u_{II_I}$$
$$p_G = p_I$$
$$\rho_G = \rho_I$$

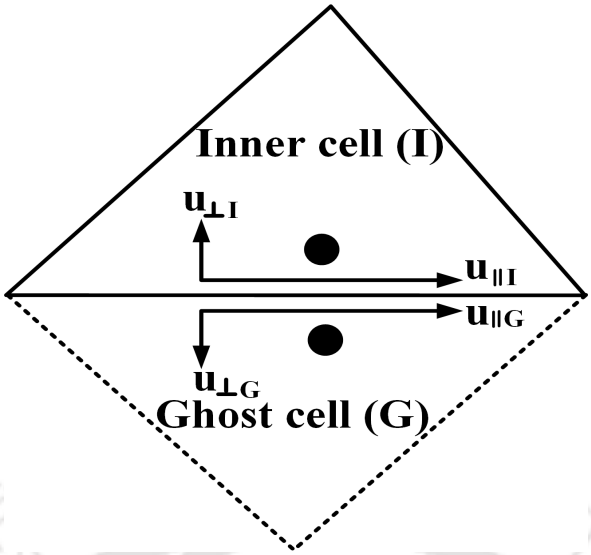

Figure 2.3: Mirror or Ghost cell approach

2.6.2 No-slip wall boundary

This condition permits no movement of fluid along the wall. This is due to the presence of friction at the surface which introduces high viscous forces at the wall boundary. For implementation of this boundary condition, tangential velocty (u_{II}) near the wall baoundary is set to be zero. As obvious that the wall is impermeable, so normal velocity ($u_{\perp}$) is also set to zero at the wall. Further, the pressure calcultaion is done by extrpolating variables from the adjecent inner cell of the viscous wall boundary. However, temperature value is calculated according to the boundary condition as isothermal or adiabatic. For isothermal wall boundary condition, the temperature value is kept fxied or constant for the viscous wall. The mass consentrations of species are also set to fixed values for this condition. However, for the adiabatic wall boundary condition the gradient of temperature normal to the wall, along with the species gradient, is set to zero.

2.6.3 Supersonic inlet boundary

As per characteristics theory [113], all eigenvalues have the same sign for the supersonic inlet. Also, there is an upstream influence of the fluid during inlet to the computational domain. Hence, all conservative variables are fixed to the adjecent interior cell at the supersonioc inlet.

2.6.4 Supersonic outlet boundary

Supersonic outlet boundary condition also has same sign of the eigenvalues as that of supersonioc inlet boundary. But, still we evaluate all flow variables at the outer face

from the adjecent innner cell of outlet boundary rather fixing them. In the present formulation startegy, zeroth-order extrapolation is used for the evaluation.

2.7 Temporal discretization

The methodology of temporal desretisation is essential for the requirement of steady state solution. This method converts ordinary differential equations (ODE) into the system of single or multiple algebaraic equations which are obtained by the spatial discretisation. Let us reconsider the semi-descretised form of equation as mentined in Eqn 2.16. Here, the convective ($H_{C\perp}$) and viscous ($H_{v\perp}$) flux vectors can be added into a single flux vetor as $H_\perp$. Thus $H_\perp$ can be written as $H_\perp = H_{C\perp} - H_{v\perp}$ and final form of Eqn 2.16 can be viewed as:-

$$\frac{d\overline{U}_i}{dt} = -\frac{1}{\Omega_i}\sum_{J=1}^{n_f} H_{\perp_J}\,\Delta S_J - \overline{S}_{ci} - \alpha\overline{S}_i = R(\overline{U}_i) \tag{2.17}$$

Commonly there are two methods for the time marching which are explicit and implicit. Sometimes, combination of these two methods, known as semi-implicit approach, is also used for the fast convergence and accurate solutions. The explicit method provides accurate and stable solution at the expense of larger calculation time. Courant-Friedrichs-Levy (CFL) condition is generally used for the calulation of the time step (Δt) for the explict procedure. This condition provides very small time step and offers higher computational time for the inviscid as well as viscous simulations. For the present solver, this time step is calculated for every control volume using the expression as given below:-

$$\Delta t_i = \frac{\Gamma\sqrt{A_i}}{[\sqrt{(u_i^2 + v_i^2)} + a_i]}$$

Here, Γ is CFL number while A_i, a_i, u_i and v_i respectively are area, acoustic velocity, flow velocity in x and y direction for every i^{th} computational cell. The constant value of CFL number is selected as less than one for every simulations. Here, the time step can be selected by calculating Δt for every i^{th} cell or as the global minimum value. However, imlicit method uses bigger time step and saves the computaional time for the simulations and also provides unconditinally stable solution. In view of this, present solver is based on the semi-implicit time integration approach to insure fast and stable solutions. For the non-equilibrium reacting flows, the reaction is very fast and marked with very low time scale as compared to the flow time scale. Thus,

implemntaion of the explicit time descretisation method is essential for the efficient and stable solutions. However, the imlicit time marching is used for the descretisation of source term only as given by Bussing and Murman[114]. This is done to reduce the computational time of the simulations. The descretisation precidure of semi-implicit time marching method is given below. The semi-desritised form of Eqn 2.17 can be written as:-

$$\frac{U_i^{n+1} - U_i^n}{\Delta t} = -\frac{1}{\Omega_i}\Big(\sum_{J=1}^{n_f} H_{\perp_J}\,\Delta S_J\Big)^n - \overline{S}_{ci}^{n+1} - \alpha\overline{S}_i^n \tag{2.18}$$

Here, the source term $\overline{S}_{ci}$, which is produced by the chemical reactions, is linearized using Newton's method as:-

$$\overline{S}_{ci}^{n+1} = S_{ci}^n + \left(\frac{\partial S_{ci}}{\partial U}\right)^n \Delta U + O(\Delta U)^2 \tag{2.19}$$

Put this value of Eqn 2.19 in Eqn 2.18 and perform mathematical operations as given below:-

$$\frac{U_i^{n+1} - U_i^n}{\Delta t} = -\frac{1}{\Omega_i}\Big(\sum_{J=1}^{n_f} H_{\perp_J}\,\Delta S_J\Big)^n - \left[S_{ci}^n + \left(\frac{\partial S_{ci}}{\partial U}\right)^n \Delta U + O(\Delta U)^2\right] - \alpha\overline{S}_i^n \tag{2.20}$$

$$\frac{U_i^{n+1} - U_i^n}{\Delta t} - \left(\frac{\partial S_{ci}}{\partial U}\right)^n \Delta U = -\frac{1}{\Omega_i}\Big(\sum_{J=1}^{n_f} H_{\perp_J}\,\Delta S_J\Big)^n - S_{ci}^n - \alpha\overline{S}_i^n \tag{2.21}$$

$$\frac{U_i^{n+1} - U_i^n}{\Delta t} - \left(\frac{\partial S_{ci}}{\partial U}\right)^n (U_i^{n+1} - U_i^n) = -\frac{1}{\Omega_i}\Big(\sum_{J=1}^{n_f} H_{\perp_J}\,\Delta S_J\Big)^n - S_{ci}^n - \alpha\overline{S}_i^n \tag{2.22}$$

$$\frac{U_i^{n+1} - U_i^n}{\Delta t}\left[I - \Delta t\left(\frac{\partial S_{ci}}{\partial U}\right)^n\right] = -\frac{1}{\Omega_i}\Big(\sum_{J=1}^{n_f} H_{\perp_J}\,\Delta S_J\Big)^n - S_{ci}^n - \alpha\overline{S}_i^n \tag{2.23}$$

Here, I is the identity matrix. $\frac{\partial S_{ci}}{\partial U}$ is the jacobian matrix which is evaluated using following expression:

$$\frac{\partial S_{ci}}{\partial U} = \begin{bmatrix} 0 & 0 & 0 & 0 & 0 & . & . & 0 \\ 0 & 0 & 0 & 0 & 0 & . & . & 0 \\ 0 & 0 & 0 & 0 & 0 & . & . & 0 \\ 0 & 0 & 0 & 0 & 0 & . & . & 0 \\ \frac{\partial S_1}{\partial \rho} & \frac{\partial S_1}{\partial (\rho u)} & \frac{\partial S_1}{\partial (\rho v)} & \frac{\partial S_1}{\partial (\rho E)} & \frac{\partial S_1}{\partial C_1} & . & . & \frac{\partial S_1}{\partial C_{N-1}} \\ \frac{\partial (.)}{\partial \rho} & \frac{\partial (.)}{\partial (\rho u)} & \frac{\partial (.)}{\partial (\rho v)} & \frac{\partial (.)}{\partial (\rho E)} & \frac{\partial (.)}{\partial C_1} & . & . & \frac{\partial (.)}{\partial C_{N-1}} \\ \frac{\partial (.)}{\partial \rho} & \frac{\partial (.)}{\partial (\rho u)} & \frac{\partial (.)}{\partial (\rho v)} & \frac{\partial (.)}{\partial (\rho E)} & \frac{\partial (.)}{\partial C_1} & . & . & \frac{\partial (.)}{\partial C_{N-1}} \\ \frac{\partial S_{N-1}}{\partial \rho} & \frac{\partial S_{N-1}}{\partial (\rho u)} & \frac{\partial S_{N-1}}{\partial (\rho v)} & \frac{\partial S_{N-1}}{\partial (\rho E)} & \frac{\partial S_{N-1}}{\partial C_1} & . & . & \frac{\partial S_{N-1}}{\partial C_{N-1}} \end{bmatrix}$$

The elements of the jacobian matrix is calculated by chain rule of differentiation as follows:-

$$\left.\frac{\partial S_j}{\partial T}\right|_{Ci,i=1...,N-1} = W_j \sum_{i=1}^{N_R} (v_{ij}^{''} - v_{ij}^{'}) \left[\frac{K_{fi}}{T} \left(m_{fi} + \frac{E_{fi}}{R_u T} \right) \prod_{l=1}^{N} n_l^{v_{il}^{'}} - \frac{K_{bi}}{T} \left(m_{bi} + \frac{E_{bi}}{R_u T} \right) \prod_{l=1}^{N} n_l^{v_{il}^{''}} \right] \tag{2.24}$$

$$\left.\frac{\partial S_j}{\partial \rho u}\right|_{\rho,\rho E,C_{i,i=1...,N-1}} = -\frac{u}{\rho C_v} \left.\frac{\partial S_j}{\partial T}\right|_{C_{i,i=1...,N-1}} \tag{2.25}$$

$$\left.\frac{\partial S_j}{\partial \rho E}\right|_{\rho,\rho E,C_{i,i=1...,N-1}} = \frac{1}{\rho C_v} \left.\frac{\partial S_j}{\partial T}\right|_{C_{i,i=1...,N-1}} \tag{2.26}$$

$$\left.\frac{\partial S_j}{\partial C_i}\right|_{\rho,\rho E,C_{i,i=1...,N-1}} = W_j \sum_{k=1}^{N_R} \left[(v_{ki}^{''} - v_{ki}^{'}) \left(\frac{v_{ki}^{'} K_{fk}}{C_i} \prod_{l=1}^{N} n_l^{v_{kl}^{'}} - \frac{v_{ki}^{''} K_{bk}}{C_i} \prod_{l=1}^{N} n_l^{v_{kl}^{''}} \right) \right] - \frac{e_i - e_N}{\rho C_v} \left.\frac{\partial S_j}{\partial T}\right|_{Ci,i=1...,N-1} \tag{2.27}$$

2.8 Gas models

Selection of the gas models in supersonic/hypersonic flow regimes is very essential to predict the correct flow field around the object. In present investigations, both low as well as high enthalpy are simulated to manifest the real gas effect. In view of this, various gas models are integrated in the present solver and are used as per our choice/requirements. The details of these gas models and their incarporation procedure in the present solver is presented in below section:-

2.8.1 Calorically perfect gas model

Perfect gas model holds good when the intermolecular forces between molecule is negligible. In this model specific heat at constant pressure (C_p), specific heat at constant volume (C_v) and specific heat ratio (γ) are considerd as 1.005 J/Kg/K, 0.716 J/Kg/K and 1.4 respectvely. This model uses ideal gas eqation as given in Eq. 2.28 for the calculations of the flow variable. Some researchers [115] used this model to perform the non-reacting flow simulations.

$$pv = n\overline{R}T \tag{2.28}$$

Here, p is the pressure, v is the volume, n is number of moles, T is the temperature and $\overline{R}$ is the universal gas consatnt which can be used as $\overline{R} = R * MW$. Here, R is the charectrictic gas constant and MW is the molecular weight of the gas. Further, this gas model uses following expressions to calculate specific internal energy (e), acoustic speed (a) and enthalpy (h).

$$e = RT/(\gamma - 1), a = \sqrt{\frac{\gamma p}{\rho}}, h = \gamma RT/(\gamma - 1) \tag{2.29}$$

Here, ρ is the density of the gas. Sutherland's viscosity model [116] is used for the calculation of the dynamic or absolute viscosity (μ) in present solver. The generalised dimensionless form of this equation can be written as:-

$$\frac{\mu}{\mu_{ref}} = \left(\frac{T}{T_{ref}}\right)^{3/2} \left(\frac{T_{ref} + S}{T + S}\right) \tag{2.30}$$

Here, μ_{ref} is reference abolute viscosity of air at fixed temperature which is equal to 17.16$\times$ 10^{-6} N s/m^2, T_{ref} is the reference temperature which is taken as 273.15 K and S represents Sutherland's constant which is considered as 110.56. Prandtl number is taken as 0.71 for air.

2.8.2 Reacting gas model

Simulations of lower enthalpy flow can be well handeled by the calorically perfect gas model. But for high speed or high temperature flow field, as encontered in the hypersonic flow regimes, this model no longer remains valid. Thus it is necessary to incorporate reacting gas model for correct prediction of the flow field at high enthalpy conditons. For this Navier-stokes equation is solved along with the species conservation equation as mentioned in the Eq 2.1. The details of calculations of flow variables and

tarnsport properties (μ, K) for this model are described in the section 2.1.

2.8.3 Frozen gas model

The fluid in the frozen gas model is treated as the non-reacting mixture because it does not account any chemical reactions in the flow field. Thus source term due to the presence of chemical reactions is not considered while applying frozen gas model. Moreover all other thermo-physical parametres are calcultaed in similar manner as discussed in the reacting gas model. This model is also a part of the present solver but investigation is performed using two models only i.e. perfect and reacting gas.

CHAPTER 3

AEROTHERMODYNAMIC ASSESSMENT OF SPIKED CONFIGURATION FOR DRAG REDUCTION AT HYPERSONIC SPEEDS

In the present investigation, the aerothermodynamic analysis is performed for blunt-body configurations with spikes mounted in view of drag reduction effectiveness. The in-house perfect gas and chemical non-equilibrium solvers are utilized for this purpose. This analysis revealed that flow separation and associated shock restructuring are responsible for drag reduction. Two vortices are observed in the separation zone for shorter spikes while three vortices are observed for longer spike simulations. The downstream shift of upstream influence location on the spike and upstream shift of flow reattachment location as well as the shock impingement point on the surface of the blunt-body have been marked for high enthalpy freestream conditions. These alterations in the flow field and the related reduction in separation bubble size led to a reduction in the effectiveness of the spike in reducing the drag force. Around $13-16\%$ *reduction in the effectiveness has been registered for* 4.0 *MJ/kg case and sharp spike mounting. Such a reduction in effectiveness is noted to be lower for longer spikes. These real gas effects are seen to be responsible for an increase in wave drag and friction drag for high enthalpy flow over a spiked configuration. Therefore it is recommended to account for the real gas effects while considering spike as a drag-reducing device.*

Kumar S, Kulkarni V, Jammy S P. "Aerothermodynamic Assessment of Spiked Configuration for Drag Reduction at Hypersonic Speeds", ***Journal of Aerospace Engineering***, 2020 Nov 1;33(6):04020076.

3.1 Introduction

Objects experiencing hypersonic flows such as long-range missiles, space planes, reusable launch vehicles, re-entry vehicles etc. have blunt shaped configurations. Such configurations have numerous advantages, like reduced load on the thermal management system [117], accommodating extra payloads [118] and to help deceleration during the re-entry phase of the vehicle, to name a few. However, these blunt configurations inherit major disadvantages associated with upstream formation of strong bow-shocks. The bow-shock induces a large wave drag, which is advantageous during the descent phase of the flight but increases the fuel consumption during ascent and cruise phases. To overcome the limitations caused due to the presence of bow shock, structured/passive and un-structured/active methods are used to alter the location and shape of the bow-shock and hence the aerothermodynamic properties of the fluid in the shock layer or flowing over the vehicle surface. The un-structured approaches reported in the literature are, injecting a supersonic jet counter to the flow [119] or concentrated energy deposition along the stagnation streamline [120]. Whereas passive approaches use a retractable aerospike at the nose [121] or a forward-facing cavity [122] to alter the flow structure and thereby the properties. For drag reduction, there is also a possibility of using a combination of the active and passive methods as reported in the literature [123]. Reducing the wave drag by using a spike is the simplest and cost-effective choice by converting the bow shock into a system of weak shocks, hence it is the central theme of present studies. For the spiked body, as shown in Fig. 3.1,

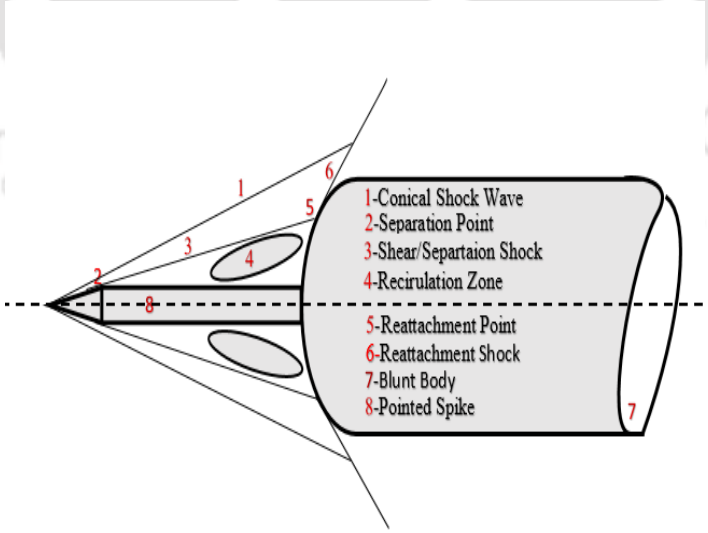

Figure 3.1: Schematics of flow over the spiked body

the flow separation on the surface of the spike leads to the formation of recirculation regions or dead air zone, near the original stagnation point. Such formation of the

separation bubble results in lower pressures and temperatures and consequently helps in reducing the drag incurred by the spacecraft. The size of this separation zone is inversely proportional to the drag force acting on the vehicle and is a driving force for numerous studies.

From the literature, it can be seen that many numerical or experimental studies are reported for the spiked bodies in order to reduce the aerodynamic load in supersonic/hypersonic flow regime. Most studies mainly focused on changing the length and shape of the spike in combination with freestream Mach number while assuming a perfect gas model for simulations. However, this assumption works well only for the low enthalpy flows because specific heats (C_p, C_v) remain constant and no chemical reactions can occur. But for high enthalpy flows, the total temperature is very high and hence temperature around the blunt surface rises to a level where specific heats would change and chemical reactions can also take place. Gauer and Paull [124] attempted to address this issue for high enthalpy flows with spiked-configurations, but there are still gaps in the literature which need to be addressed. Thus, the study of chemical non-equilibrium flow is necessary for better prediction of flow field and drag in these high-temperature flow conditions. Alteration in the wave drag and skin-friction drag with the stagnation enthalpy is still an open area for investigation to understand the real gas effects. The changes due to real gas effects would be dependent on spike length, hence its variation needs to be studied. Further accurate prediction of the drag force is necessary because it helps in determining the realistic fuel requirement, possible thrust generation and feasible amount of payload. Since the drag incurred by the spacecraft depends upon separation and reattachment points, hence a close view of migration of these points on the body surface is essential in the presence of real gas effects. This understanding would also be helpful in getting the shape and size of the recirculation bubble. For the better insight of the flow physics, results obtained with perfect gas assumption are compared with those from the reacting flow solver in the present investigations. The geometry considered and the results obtained are discussed in the following sections.

3.2 Geometry and solver validation

A spherical configuration of radius 36 mm, vertex angle (θ) 66° and total projected diameter (D) 38 mm has been considered for

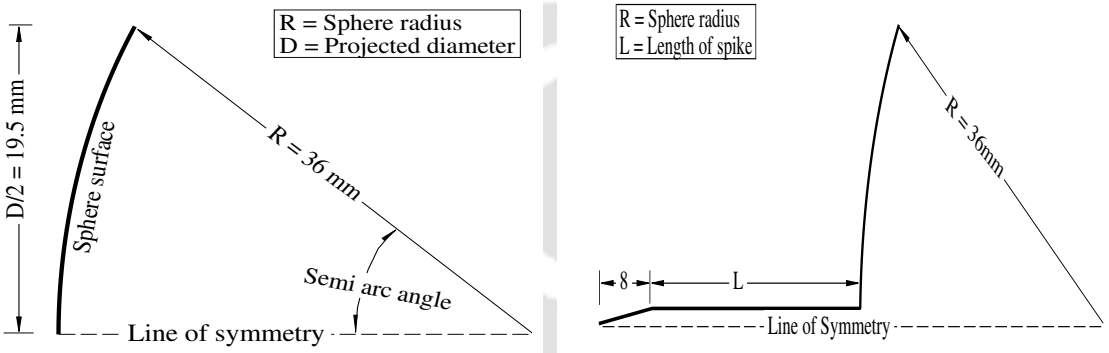

Figure 3.2: Definition of the present model [Left] (a) for the spherical body and [Right] (b) for the spiked body

the present studies (Fig.3.2 (a)). The geometry of the spike adopted here has cylindrical shape of 2 mm diameter (Fig.3.2 (b)). The same configuration was used in the experiments by D'Humieres and Stollery [125]. Several simulations are performed without spike and with different lengths of spike to diameter of the body ratios (L/D=0.125, 0.25, 0.5, 0.75, 1.0, 1.25, 1.5 and 2.125).

Initial simulations are carried out for the spherical blunt-body without spike [125]. Freestream conditions for Mach number and temperature are 8.2 and 89.3 K respectively. Choice of the grid is shown in Fig. 3.3 (a) for the case of blunt-body without spike and Fig. 3.3 (b) for the case of blunt-body with the spike. Only half part of the computational domain is meshed considering the axisymmetric flow over spiked or unspiked object for zero degree angle of attack. Hence symmetry boundary condition remains the obvious option for the domain axis.

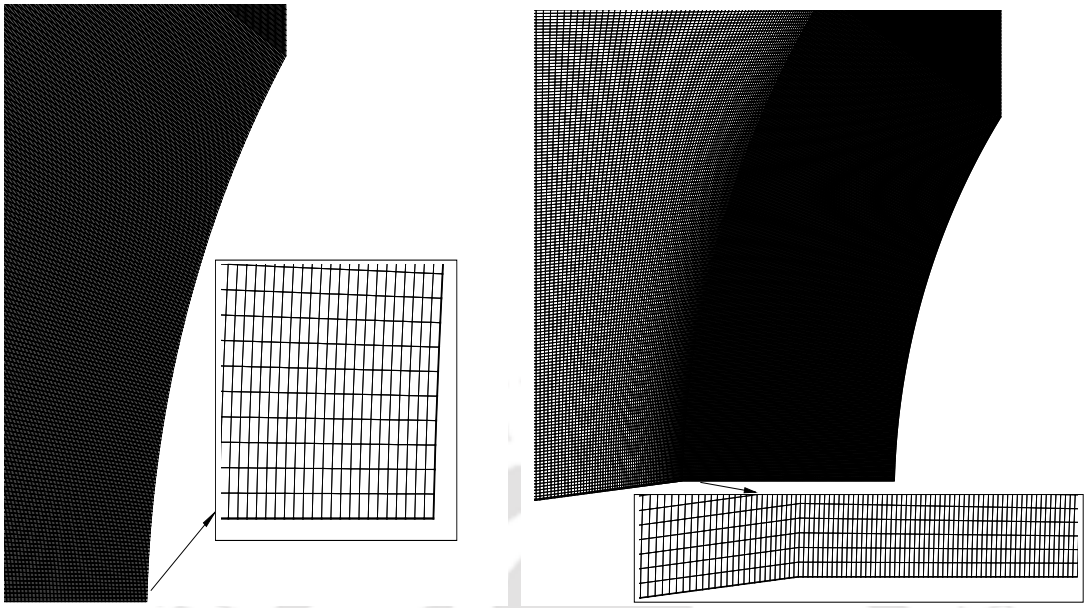

Figure 3.3: Structured grid for the [Left] (a) Spherical body with zoom view at the stagnation point and [Right] (b) Spiked body with zoom view on the spike surface

Here, isothermal (300 K) no-slip wall boundary condition is applied on the blunt-body with or without spike. Known hypersonic flow conditions are imposed at the inlet while supersonic outlet boundary condition is used for the domain outlet. Here Billig's correlations [126] are considered for the validation of inhouse reacting flow solver. This is an empirical relation which requires only Mach number and geometry details to calculate shock shape. These correlations give the shock shape and shock stand-off distance and are entitled as:-

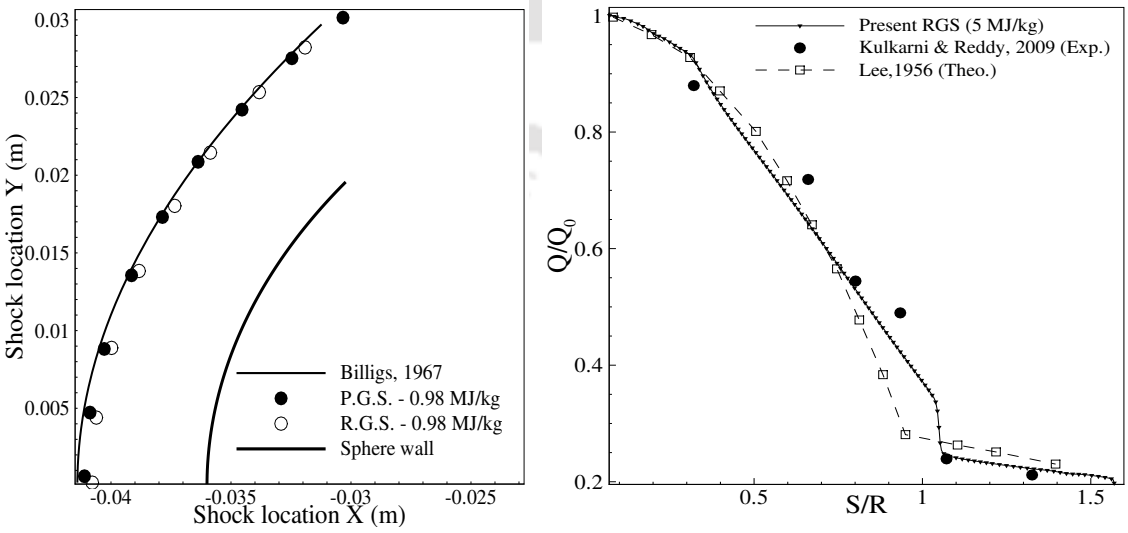

Figure 3.4: Validation of present solver [Left] (a) Shock shape with the Billigs correlation (H_0=0.98 MJ/kg) and [Right] (b) Heat flux with the experimental and theoretical results for higher freestream enthalpy (H_0=5 MJ/kg)

$x = R + \Delta - R_c \cot^2\beta((1 + \frac{y^2 \tan^2\beta}{R_c^2})^{\frac{1}{2}} - 1)$ in which $\Delta/R = 0.143exp(3.24/M^2)$ and $R_c/R = 1.143exp(0.54/(M-1)^{\frac{6}{5}})$ where, Δ is the shock stand-off distance, β is the wave angle, R is the radius of spherical body and x and y are the coordinates of shock. For the spherical body, the comparison of computed shock shape with the one obtained with Billig's correlations is shown in Fig. 3.4 (a). It is evident here that, the empirical shock shape matches very well with the shape obtained from the perfect gas solver (P.G.S.). Minor discrimination noticed near the stagnation region for the shape obtained from real gas solver (R.G.S.) is mainly due to temperature dependent specific heats. Further, validation for the present R.G.S. is carried out for

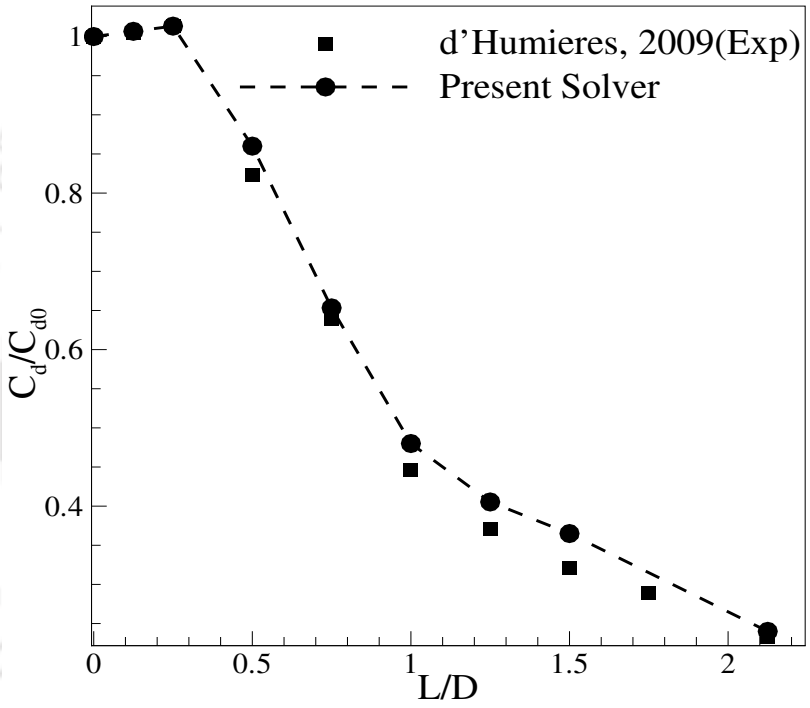

Figure 3.5: Comparision of dimensionless drag with the experimental results

the high enthalpy inflow condition (5.0MJ/kg) and geometry used by Kulkarni and Reddy [127]. For this, Mach 8.0 hypersonic flow over a blunt cone of nose radius 30 mm, base diametre 70 mm and cone angle 60° is simulated. Computed results of wall heat flux are compared with experimental [127] and theoretical results [128] in Fig. 3.4 (b). The compared results show very good agreement and accuracy of the present solver. Validation studies are then extended for the drag reduction cases using various spike lengths. For these simulations, the structured grid-based computational domain of the spiked body is used (Fig. 3.3 (b)). Normalized drag coefficient obtained from the computation against the spike length, in comparison with the experimental findings, is shown in Fig. 3.5. It can be seen that computed results match very well with the experimental results [125]. Here the conical shock wave is noticed for the

initial spike lengths of 0.125D and 0.25D, but still, there is no drag reduction in those cases. The same situation was also observed by D'Humieres and Stollery. Further, with increase in the spike length reduction in drag force is marked for all the increments in the length and this is consistent with the literature reported findings. Thus magnitude and trend for the drag reduction are in good match between the literature reported experimental studies and the present CFD studies. Thus validated in-house solver is used for further investigations.

3.3 Grid independence study

Grid independence study has also been performed for checking the sensitivity of the results obtained from the present solver. For this, four different types of grid are used for the above said purpuse. Details like total number of cells and hight of the first cell near stagnation region are mentioned in the Table 3.1.

Table 3.1: Size of different grid used for the grid independence

Type	No. of Cells	X	Y
Grid 1	17 K	$7.8\text{x}10^{-3}$	$7.2\text{x}10^{-2}$
Grid 2	38 K	$3.4\text{x}10^{-4}$	$8\text{x}10^{-3}$
Grid 3	62 K	$6.2\text{x}10^{-5}$	$9\text{x}10^{-4}$
Grid 4	98 K	$2.7\text{x}10^{-5}$	$7\text{x}10^{-5}$

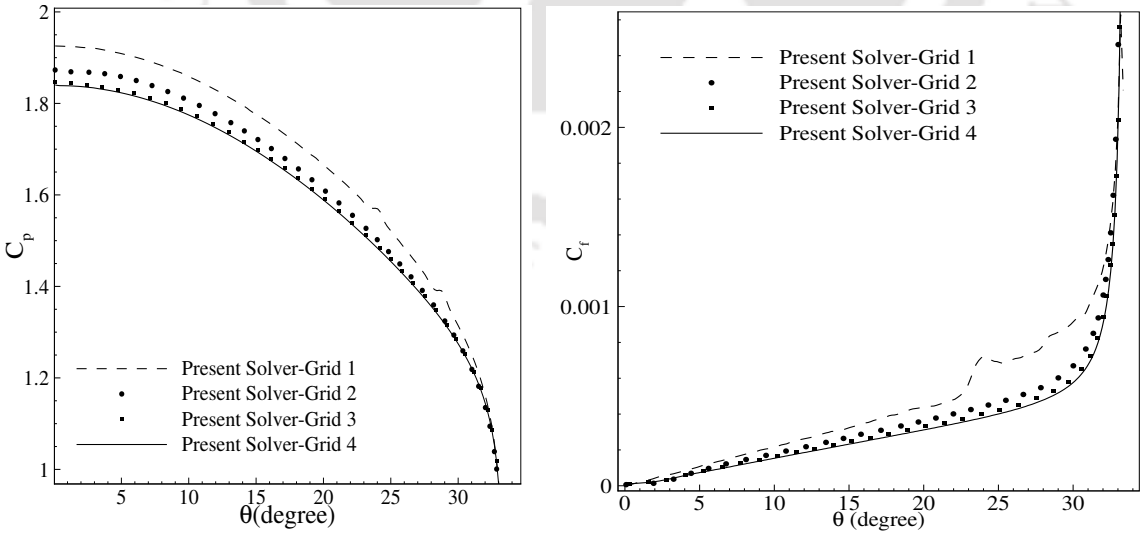

Figure 3.6: Grid sensitivity for the [Left] (a) Surface pressure and [Right] (b) Surface shear stresses

Simulations are done for the spherical object (Fig.3.3 (a)) and same freestream condition as mentioned in literature [125]. Thus obtained surface pressure and surface

shear stress are shown in terms of pressure coefficient and skin-friction coefficient in Fig.3.6 (a) and Fig.3.6 (b) respectively. It is clear from these figures that the result bears mesh independence beyond the mesh size corresponding to Grid 3. Such Grid independence studies are performed for other cases also and the most appropriate Grid is used for further simulations.

3.4 Results and discussion

3.4.1 Aerothermodynamics of the flow over unspiked body

Hypersonic flow over the blunt-body forms a strong bow shock which changes its dynamics in the reactive environment. To investigate this, three different (low, medium and high) freestream stagnation enthalpy conditions (Table 3.2) are considered in the present studies. The lowest stagnation enthalpy condition (0.98 MJ/kg) corresponds to a minor variation in specific heats with no chemical reactions, hence this condition

Table 3.2: Different freestream conditions for the simulation of reacting flow

No.	$T_{0\infty}$ (K)	P_∞ (Pa)	T_w (K)	h_0 (MJ/kg)	Re_∞ (per m)	Y (O_2)	Y (N_2)
1	1290.21	950	300	0.98	$9.01\text{x}10^6$	0.235	0.765
2	2282.78	950	300	2.00	$3.92\text{x}10^6$	0.235	0.765
3	4269.38	950	300	4.00	$1.75\text{x}10^6$	0.235	0.765

would have resemblance with the perfect gas assumption. Intermediate stagnation enthalpy condition (2.0 MJ/kg) has strong specific heat variation with no chemical reactions. The highest stagnation enthalpy condition (4.0 MJ/kg) accounts for variation in specific heats and also chemical reactions. Figure 3.7 shows the shock shape (evaluated using the Billig's correlation) for all the cases given in Table 3.2. As seen here, the shock shape obtained from Billig's correlation agrees well for the perfect gas flow model but not for the reacting gas flow model at the same total temperature of the lowest value (Fig. 3.7). Further, there is a deviation between the predicted and computed shock shapes for higher total temperature conditions as shown in Fig. 3.7. These changes are mainly due to the temperature dependent specific heats (C_p, C_v) of the flowing gases and chemical reactions among them. Shock gets closer to the blunt-body in the presence of such real gas effects; this difference between the dissociating flow and the perfect gas flow can be effectively seen in the temperature contour as shown in Fig.3.8 (a).

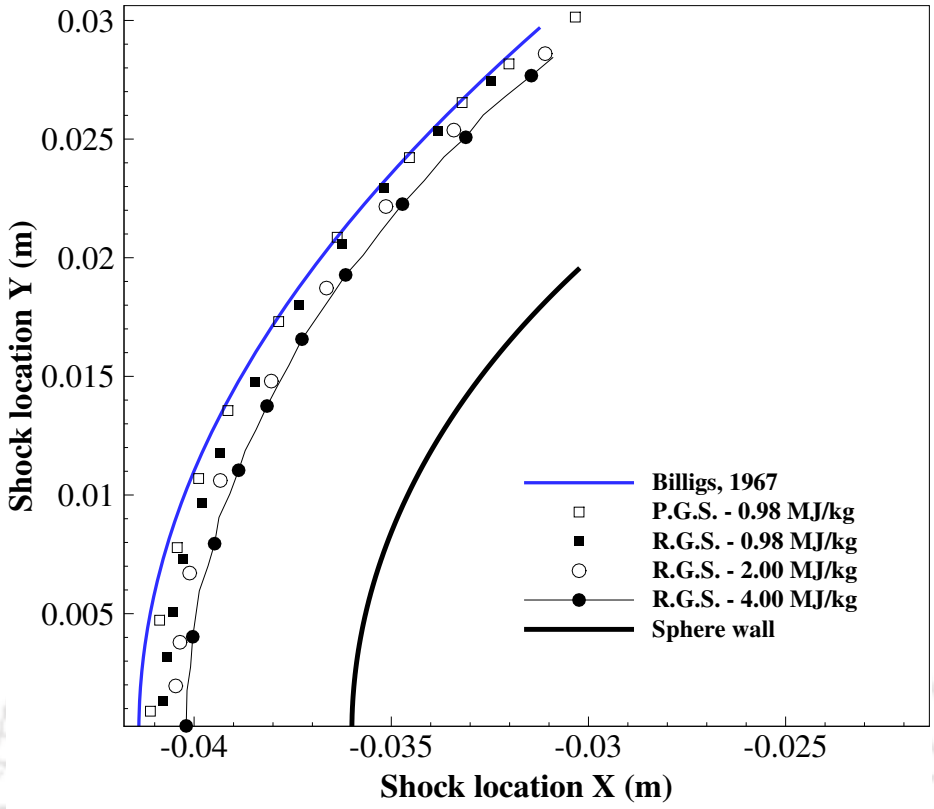

Figure 3.7: Alteration of the shock shape for various stagnation enthalpy.[P.G.S. - Perfect gas solver and R.G.S. - Reacting gas solver]

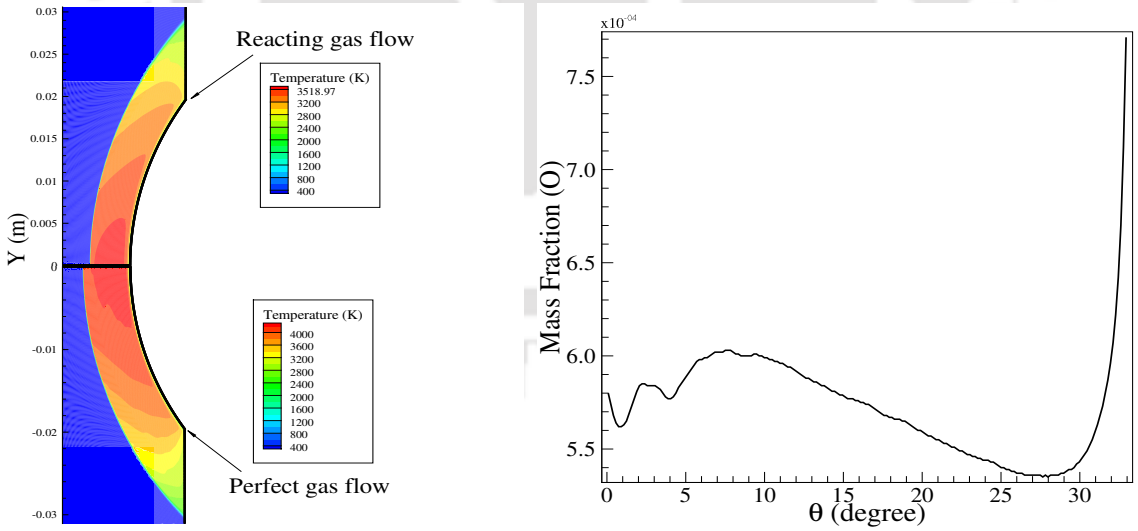

Figure 3.8: [Left] (a) Temperature conture for perfect and reacting gas flow for the enthalpy of 4.0 MJ/kg and [Right] (b) Variation of dissociatied species (O) at total freestream enthalpy of 4.0 MJ/kg

It is evident here that the changes in the specific heats and chemical reactions decrease the total temperature at the stagnation point and in general the static temperature in the shock layer. For the highest enthalpy simulation (4.0 MJ/kg), dissociation

of O_2 into O is clearly seen in Fig.3.8 (b). Such gas dynamic changes alter the surface flow properties, and for further analysis, the variation of coefficient of pressure (C_p) over the surface is as shown in Fig. 3.9. Here, C_p is evaluated as the ratio of difference between surface pressure & freestream pressure to the freestream dynamic pressure and is given by,

$$C_p = \frac{2(P - P_\infty)}{\rho_\infty {U_\infty}^2} \tag{3.1}$$

Computed result of C_p shows that inlet stagnation enthalpy does not alter the surface pressure for calorically perfect gas model, but it gets affected in the reacting flow case. There is a minor rise in the pressure of about 0.67% for inlet enthalpy of 0.98 MJ/kg at the stagnation point. The changes in peak pressure value obtained are higher at higher enthalpy like, 1.3% for 2.0 MJ/kg and 2.1% for 4.0 MJ/kg compared to the perfect gas solver. This difference is noticed at all the surface locations of the object.

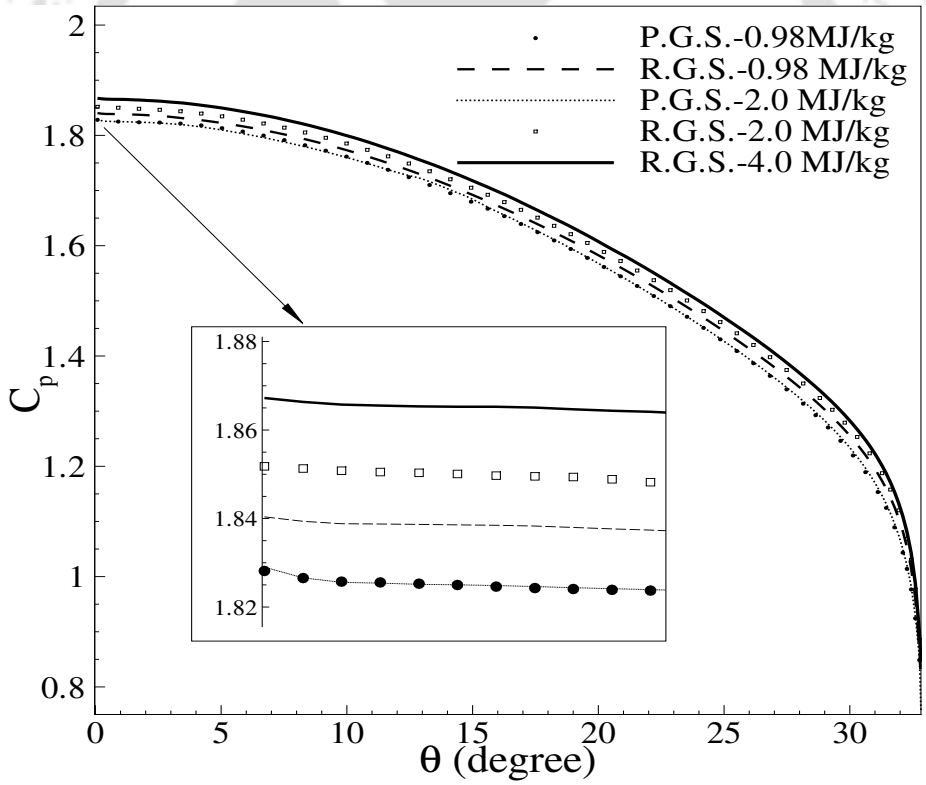

Figure 3.9: Effect on the surface pressure for the unspiked body.[Zoom view at the stagnation point]

Hence increase in pressure increases the drag force on the object for real gas flow. For the lowest total enthalpy simulations, there is almost no difference between the drag force obtained from perfect and real gas models, which is approximately 79.20 N. On the other hand, real gas effects lead to a drag force of 80.63 N for 2.0 MJ/kg and 81.78

N for the 4.0 MJ/kg compared to the perfect gas case (79.40 N and 79.77 N for the 2.0 MJ/kg and 4.0 MJ/kg respectively). It is clear that the drag force is higher due to real gas effects and it varies with the stagnation enthalpy which is consistent with the wall pressure variation (Fig. 3.9). We have already discussed that R.G.S. predicts

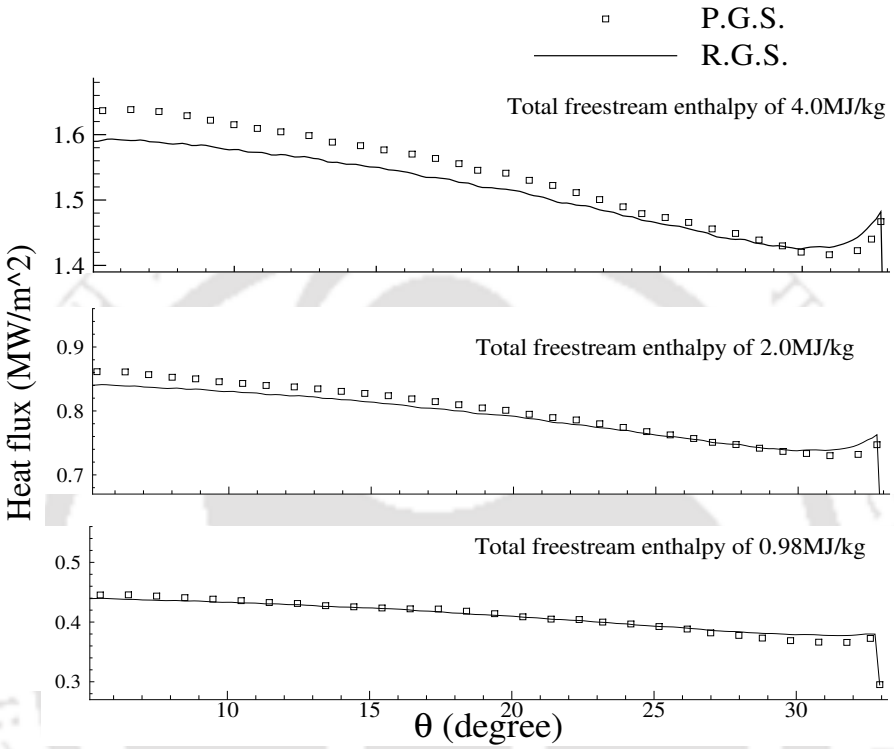

Figure 3.10: Variation of heat flux at all enthalpy

lesser flow-field temperature as compared to the P.G.S. at the higher enthalpy cases (Fig.3.8 (a)). Hence, magnitude of the heat flux on the blunt object is also lesser as shown in Fig. 3.10. There is 2.38% and 3.8% reduction in computed heat flux for the higher freestream stagnation enthalpy of 2.0 MJ/kg and 4.0 MJ/kg.

3.4.2 Aerothermodynamics of spiked body

(A) Real gas effects on pressure variation

The pressure variation on the spike and blunt body assembly resembles with the pressure variation over an object which encounters shock wave boundary layer interaction (SWBLI) [129]. Here as well in Fig.3.11 (a), initially pressure decreases and then remains constant on the spike surface till a specific point which is invariantly referred as the upstream influence location in the terminologies of SWBLI. Beyond this definite point, pressure starts to increase and attains a plateau which continues from the spike surface to the blunt-body.

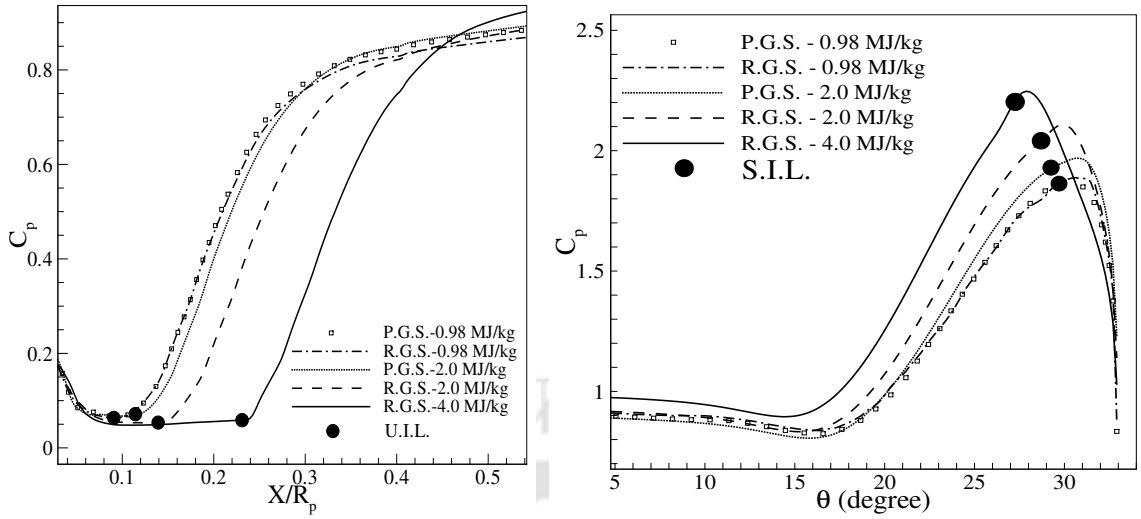

Figure 3.11: Closeup of C_p on the [Left] (a) Spike surface (U.I.L. - Upstream Influence Locations) and Right[] (b) Body surface (S.I.L. - Shock Impingement Locations)

Here the plateau pressure region partially wets the spike and partially the blunt surface (Fig.3.11). Presence of such plateau in the pressure plot is an indication of existence of separation zone. However, further details like the size of the separation zone cannot be furnished from the pressure plot. Beyond the plateau region, pressure increases and attains a peak at the shock impingement point. Further downstream of this point, pressure decreases on the blunt surface. This pressure variation is consistent for all the enthalpy cases and is seen with either gas flow model. While extracting the real gas effects from the pressure plots, it is found that, for low freestream enthalpy of 0.98 MJ/kg case, both perfect and reacting flow solvers predict same location of the upstream influence and the shock reattachment. This is due to minor variation in specific heats and the viscosity at low total temperature; further, the temperature in the flow field remains low and insufficient to trigger the chemical reactions. However, the real gas effects become prominent with increase in stagnation enthalpy. As a result of this, the upstream influence location (U.I.L.) is noticed to shift downstream of the spike tip with the increase in freestream stagnation enthalpy (Fig.3.11 (b)). Moreover, there is upstream shift of shock impingement location (S.I.L.) in the presence of real gas effects. It can be interpreted here that, the energy consumed due to the presence of endothermic reactions in real gas flow keeps the stagnation region temperature well below the same predicted by the perfect gas flow model. Hence, the shock layer density remains higher in case of real gas flow simulations. This high density or low specific volume fluid in the shock layer suppresses the swelling of the primary bow shock. These changes in density would ultimately lead to the noticeable shift of UIL and SIL. Hence, an inward shift of critical locations, noticed from the pressure variation, hints about the decrease in the separation zone size.

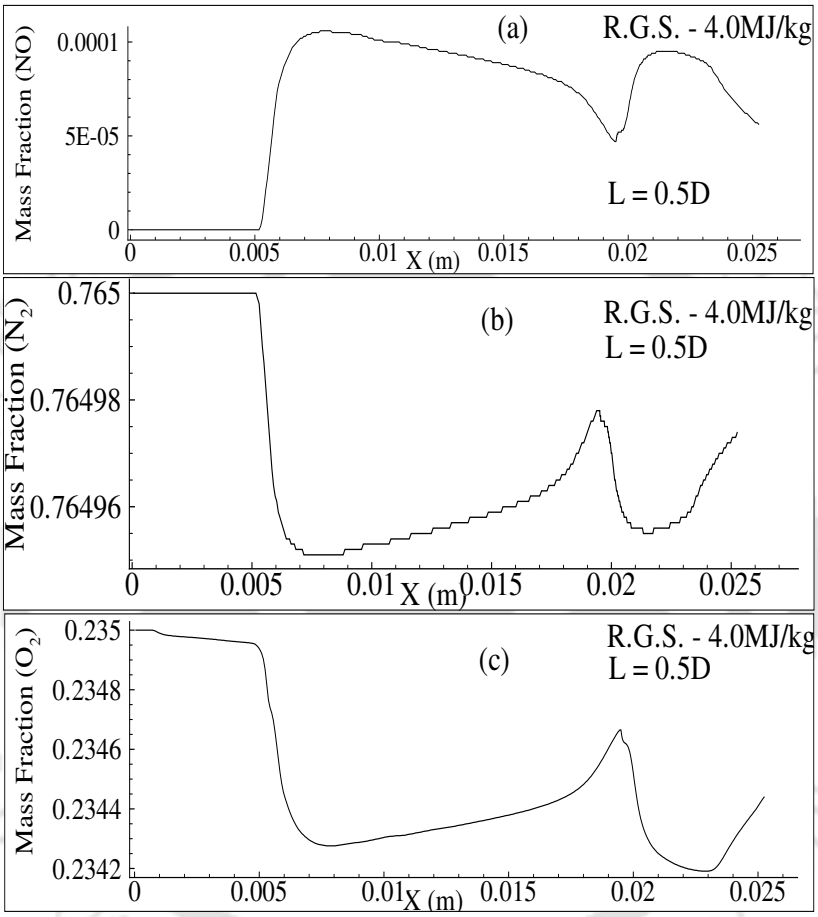

Figure 3.12: Variation of different species for the spike length of 0.5D

Such major deviation of these locations from low enthalpy perfect gas model is only due to the alteration in viscosity which happens to be the function of temperature. The composition of this gas would change in high enthalpy flows which further complicates the viscosity variation in the boundary layer. In a particular case of 4.0 MJ/kg stagnation enthalpy, dissociation of O_2 has been noticed. From the Fig. 3.12, it is evident that dissociation of O_2 starts at 0.7 mm from the spike tip while the same for N_2 starts at 5.0 mm due to requirement of higher static temperature for its dissociation. But, the presence of NO due to recombination of O and N is also clear from Fig. 3.12. Thus, high enthalpy flow partially retrieves the energy from such recombination reactions which start at a distance 5.1 mm from the spike tip.

Therefore, it is clear from the species variation that, there exists a mixture of gases at the upstream influence location for 4.0 MJ/kg stagnation enthalpy case. However, for 2.0 MJ/kg, the temperature in the flow field does not support any reaction but still influences variation in the specific heats (C_p, C_v). This change leads to alteration in the shock structure. Thus, change in viscosity and specific heats in the presence of real gas effects alter the dynamics of the boundary layer which in turn helps to shift the upstream influence and shock impingement locations with the increase in stagnation enthalpy.

(B) Real gas effects on flow separation

Change in the upstream influence and shock impingement locations with change in stagnation enthalpy indicate an alteration in separation zone size. Investigations are then carried out to examine the real gas effects on the size of the recirculation zone. Here, separation and reattachment locations are initially marked from the skin friction plot or variation of wall shear along the surface. These are the special points which bear zero value of skin friction coefficient (C_f). Variations of the C_f for smaller spike (L=0.5D) and for larger spike (L=1.5D), along the spike and the blunt-body, are shown in Fig. 3.13 (a) and Fig. 3.13 (b) respectively. Only one set of separation and reattachment points has been detected here for the smaller spike but there are two such sets for the longer spike. Streamline pattern for these two spike cases reveals that there are two vortices for the shorter spike (Fig.3.14 (a)), out of which eye of one vortex, which is smaller in size, is near the spike mounting location or at the spike-body junction. The other or larger vortex is found away from the short spike surface. This vortex actually recasts the shock structure and is mainly responsible for the drag reduction. In case of longer spike, two small vortices are noticed (Fig.3.14 (b)) among which one is positioned at the spike-body junction while the other is exclusively on the spike surface. Here for longer spike case as well, the larger vortex, which remains away from the body, can be seen to restructure the shock pattern necessary for drag reduction. These vortex structures, for any spike length, are seen to be independent of the gas flow model. But the separation or reattachment locations and hence the size of the recirculation zone are seen to be influenced by the real gas effects. Delay in upstream influence location with the increase in stagnation enthalpy, which hinted for the delay in separation, gets confirmed from the C_f plot. These real gas effects are further demonstrated through Fig. 3.15 which shows the separation streamline around most upstream separation point. But for 0.98 MJ/kg case, separation length is found to be same for the perfect and real gas flows (Fig. 3.15 (a)) because there is no chemical reaction and less variation of specific heats for this low-enthalpy situation. The properties do vary for the stganation enthalpy of 2.0 MJ/kg where separation point for this case also shifts downstream for real gas in comparison of perfect gas as

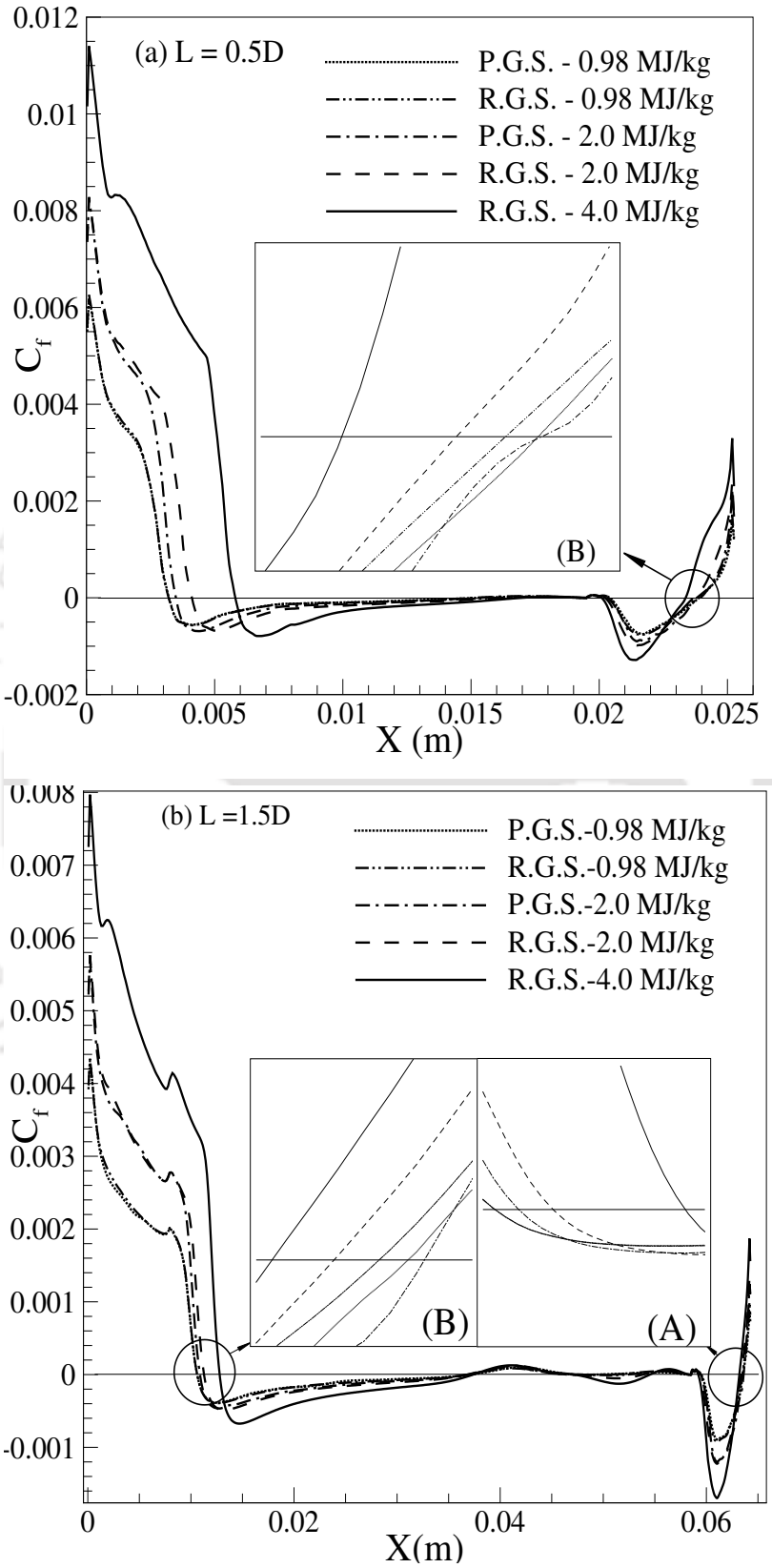

Figure 3.13: Effect of real gas flow on C_f for [Top] (a) L=0.5D and [Bottom] (b) L=1.5D.[Zoom view of C_f=0 at the (A) spike surface, and (B) body surface]

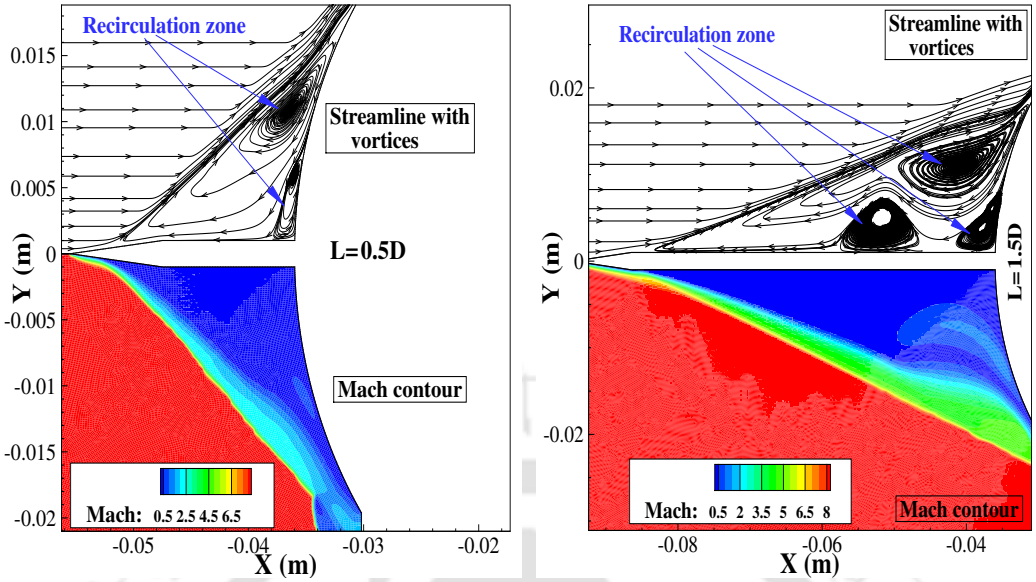

Figure 3.14: Streamline and Mach contour for [Left] (a) L=0.5D and [Right] (b) L=1.5D.

shown in the Fig. 3.15 (b) and Fig. 3.15 (c) respectively. Further, there is 5.81 mm downstream shift of this location as seen in Fig. 3.15 (d) for 4.0 MJ/kg case. Hence it is also clear from Fig. 3.12 and Fig. 3.15 that the reactions (both dissociation and recombination reaction) take place before the separation location. Thus the influence of freestream total temperature on the most upstream separation location is evident here. It should be noted that the most upstream separation and most downstream reattachment points are bound by the larger vortex. Hence, alteration in the location of the most upstream separation point also alters the most downstream reattachment point and hence the impingement location of the conical shock wave. Streamwise distances between the flow separation location on the spike tip and the reattachment point on the blunt surface are summarised in Table 3.3. Here it is noticed that for the smaller spike, there is difference of 1.9° in the reattachment point for 4.0 MJ/kg case but no such discrimination in this angle is registered for the perfect gas model. Here the size of dead air region can be defined as the streamwise distance between upstream most separation point and downstream most flow reattachment point. There is reduction in this the size of dead air region obtained from the reacting flow solver and this reduction is higher at the elevated enthalpy for same spike length. For lower enthalpy, there is less than 0.5% discrimination in the size of dead air region for all the spike lengths between real and perfect gas flow solver based predictions. However, 15.10% reduction in the size of the dead air region for smaller spike at 4.0 MJ/kg stagnation enthalpy is seen due to real gas effects. Thus the inward migration of separation and reattachment locations decreases the size of dead air region for any spike length with

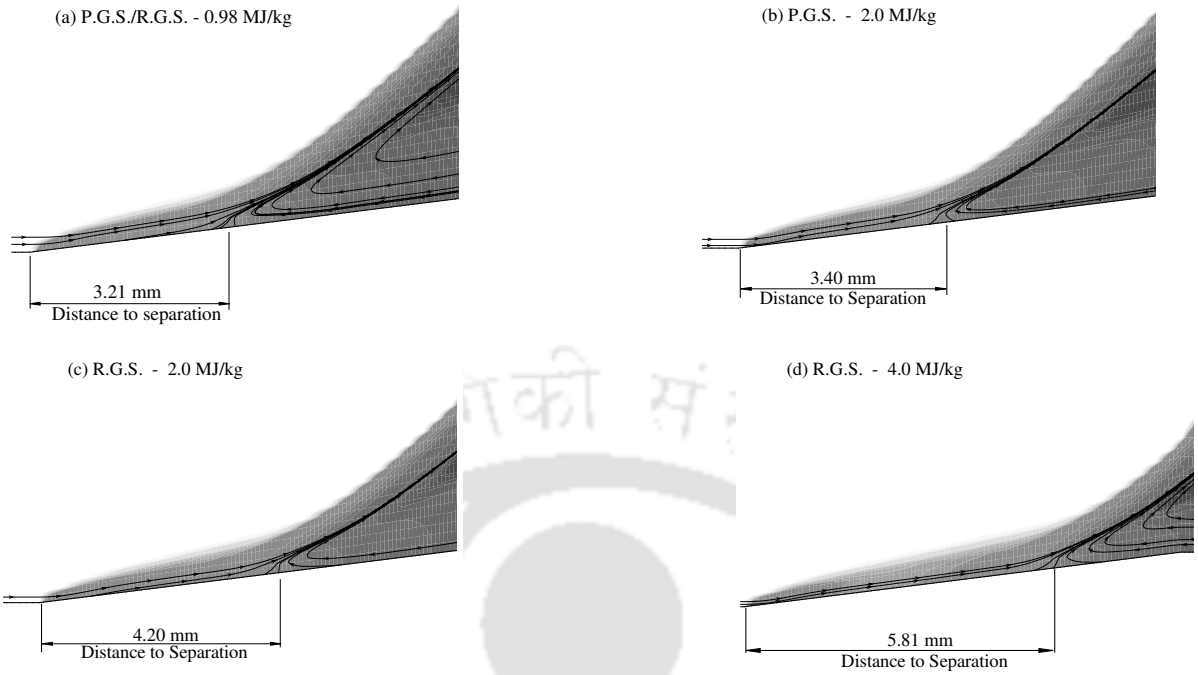

Figure 3.15: Migration of Separation point for spike length of 0.5D for the stagnation enthalpy of (a) 0.98 MJ/kg, (b) 2.0 MJ/kg (P.G.S.), (c) 2.0 MJ/kg (R.G.S.), and (d) 4.0 MJ/kg.[Distance is measured from spike tip]

Table 3.3: Migration of separation and reattachment point for various length of spike

	Separation point from spike tip (mm)			Reattachment point on body (degree)		
Length	P.G.S./R.G.S. 0.98 MJ/kg	R.G.S. 2.0 MJ/kg	R.G.S. 4.0 MJ/kg	P.G.S./R.G.S. 0.98 MJ/kg	R.G.S. 2.0 MJ/kg	R.G.S. 4.0 MJ/kg
L=0.5D	3.21	4.20	5.81	28.9	28.2	27.0
L=1.0D	7.30	8.18	9.87	30.9	30.2	29.4
L=1.5D	10.15	11.03	12.50	31.5	30.9	30.6

real gas effects. Further, it can also be noted that the flow separation location gets more influenced than the shock impingement or flow reattachment location due to change in stagnation enthalpy of the flow for any spike length.

3.4.3 Real gas effects on drag reduction

For a blunt body with or without spike, the total drag incurred is the sum of the wave drag and skin-friction drag. Here, the wave drag coefficient is calculated as $2F_d/(\rho_\infty U_\infty^2 A_p)$ where A_p is the projected area of the spherical body and F_d is wave/pressure drag force. The local skin friction force is obtained from the simulations, which is then integrated to arrive at the total shear force incurred by the object. Thus obtained total

Table 3.4: Alteration of wave drag (WD), skin friction drag (SFD) and total drag reduction for various length of spike

Conditions	L=0.5D			L=1.0D			L=1.5D		
	WD	SFD	$\%C_d$	WD	SFD	$\%C_d$	WD	SFD	$\%C_d$
P.G.S.-0.98 MJ/kg	1.23	0.0072	14.67	0.70	0.011	52.53	0.51	0.012	64.93
R.G.S.-0.98 MJ/kg	1.23	0.0072	13.27	0.73	0.011	50.86	0.56	0.012	61.93
P.G.S.-2.00 MJ/kg	1.22	0.0069	13.17	0.72	0.013	51.34	0.53	0.016	63.68
R.G.S.-2.00 MJ/kg	1.40	0.013	6.12	0.82	0.028	43.53	0.63	0.021	56.93
R.G.S.-4.00 MJ/kg	1.47	0.031	1.20	0.89	0.034	38.63	0.72	0.036	49.40

drag on the blunt-body is found to increase with an increase in stagnation enthalpy. It is evident in the present work that the total drag on the spherical body increases by 3.10% for the freestream enthalpy of 4.0 MJ/kg. With spike mounting, it is expected to have a reduction in the total drag force. But, it has been noticed that the effectiveness of spike in reducing the total drag force depends upon the freestream stagnation enthalpy. The modification in drag reduction for the spiked blunt body is summarised in Table 3.4 for different lengths of the spike. This table gives the variation of wave and friction drag with enthalpy where both are seen to be increasing with it. For the lowest enthalpy case, both the gas flow models give approximately the same drag reduction for all spike lengths. But, the amount of drag reduction decreases in the reacting flow case because of the reduced dead air region size and downstream shift of the conical shock wave with an increase in freestream total enthalpy. About $13-16\%$ decrease in the drag reduction for all spike lengths in case of 4.0 MJ/kg stagnation enthalpy conditions is observed.

3.5 Conclusions

The in-house chemical non-equilibrium and perfect gas flow solvers are validated and then employed for drag reduction studies for high enthalpy laminar flows. In the simulations carried out without a spike using the real gas solver, the wave drag increases with an increase in the freestream stagnation enthalpy. However, in the simulations with the spike included, shock restructuring is found to be responsible for the drag reduction. Both, perfect and real gas flow solvers predict the same flow field for a given spike length. Two and three vortices are observed in the recirculation zone for shorter and longer spikes respectively. However, the size of this separation zone is found to be influenced by the freestream stagnation enthalpy for real gas flows. This is due to the fact that, the upstream most separation point and downstream most flow reattachment point are found to shift inward. For low enthalpy flow case with

0.98 MJ/kg freestream stagnation enthaply, no changes in the flow field are observed. In the simulations with high freestream stagnation enthaply (4.0 MJ/kg), a 15.10% reduction in the size of dead air region is noticed. This smaller separation zone delays the formation of oblique shock and increases its strength due to real gas effects. The increase in pressure inside the separation zone and higher pressure at the shock impingement location lower the effectiveness of spike as a drag reducing agent for a blunt body. The skin friction component of the total drag is noticed to be enhanced with spike for real gas flows but it is negligible in magnitude in comparison with the wave drag. In all, around $13 - 16\%$ reduction in effectiveness is registered with the non-equilibrium flow solver for 4.0 MJ/kg free stream conditions. Hence, the real gas efects are important in simulations while considering the spike as a passive technique for reducing drag of a hypersonic blunt-body. The percentage of drag reduction offered by a spike decreases with increase in freestream stagnation enthalpy for real gas flows.

CHAPTER 4

DRAG OF A SPIKED BODY IN CHEMICALLY REACTING HYPERSONIC FLOW

Presence of a forward facing spike can increase or decrease the drag force incurred by the blunt object since it depends on the recirculation size and type of Shock-Shock interaction. Thus, prime objective of this chapter is to relate the Shock-Shock interaction and recirculation zone size for mounting a stagnation spike with the amount of drag experienced. Spike of lengths $0.125D$*,* $0.2D$*,* $0.25D$*,* $0.3D$*,* $0.4D$*,* $0.5D$*, and* $0.6D$ *are considered herein for alteration of the flowfield around the blunt object. No recirculation zone is observed for the shock standoff spike (*L=$0.125D$*) but the skin friction drag is found to be greater than the wave drag for this spike. Further, a small recirculation is noticed for the spike length of* $0.2D$ *which initiates the Shock-Shock interaction. On the other hand, strong Shock-Shock interaction, for* L=$0.25D$*, leads to rise in the peak or reattachment pressure on the object. This spike witnesses increase in total drag on the blunt object due to smaller recirculation zone and strong S-S interaction. However, development of larger recirculation suppresses the total drag on the object, even in presence of the strong S-S interactions for spike length of* $0.3D$ *and* $0.4D$*. Further, a longer spike leads to the weak interaction and bigger size of recirculation to witness the drag reduction. Exergy destruction is also investigated for the performance analysis of all spikes. Combination of spike with counterflow jet is also studied to demonstrate the drag reduction criteria for a blunt object.*

Kumar, S. and Kulkarni 2020, "Drag of a Spiked Body in Chemically Reacting Hypersonic Flow", ***Journal of Spacecraft and Rockets***, 57(5), pp.1092-1097

4.1 Introduction

Strong shock is inherent to the flights which experience the hypersonic flow regime. Enhanced drag force is an obvious outcome in the presence of such strong shocks. Various techniques have been proposed for the reduction of high drag force. Spike based drag reduction is simple for implementation and the cheapest technique among all. Therefore attachment of a sufficiently large spike in the stagnation region is generally adopted to reduce the drag force. However, the amount of drag reduction is determined by the spike length. Further, it has been noticed that a small sharp spike does not always reduce the drag. The decrement [125] or increment [130, 131] of the drag depends on the spike geometry. Most previous investigations focus on the usefulness of a spike for drag reduction. Very few studies have been performed for the mounting of a short spike since it might increase the drag. Therefore, increment of drag with short spike and associated gas dynamic perspective need detailed investigations. Aditionally, discussion is also required to understand the flow physics with a minimum length spike. Moreover, the relevance of the Shock-Shock (S-S) interaction for the drag incurred by a spiked object should also be examined.

Therefore, CFD based investigations are planned to understand the flow physics in terms of the S-S interaction for a spiked configuration to disclose the criterion for drag reduction. For this, a viscous non-equilibrium hypersonic flow solver, which can handle five species and eleven elementary chemical reactions, has been employed to identify the reason for increment/reduction of the drag force for a spiked object. These studies are further extended for various spike lengths as well. Exergy destruction has also been used in the present study for the thermodynamic analysis of the flow over a spiked body. Details of the flow field and its analysis is presented in the following sections.

4.2 Geometry and solver validation

The geometry selected for the present study features a spherical object of radius 36 mm, the vertex angle (θ) of 66° and the total projected diameter (D) of 39 mm. A cylindrical spike having 2 mm diameter (d) and a fixed semi vertex angle of 7.125° [125] is attached to this object. Freestream conditions for the simulations have been given in Table 5.1. The spike length values (L) used for the validation include L=0.125D, L=0.25, L=0.5D, and L=0.75D. The structrued body fitted grids are

Table 4.1: Details of freestream conditions

M	$P_\infty(Pa)$	$T_\infty(K)$	Y_{O2}	Y_{N2}	Y_N	Y_O	Y_{NO}
8.2	950	89.3	0.765	0.235	0.00	0.00	0.00

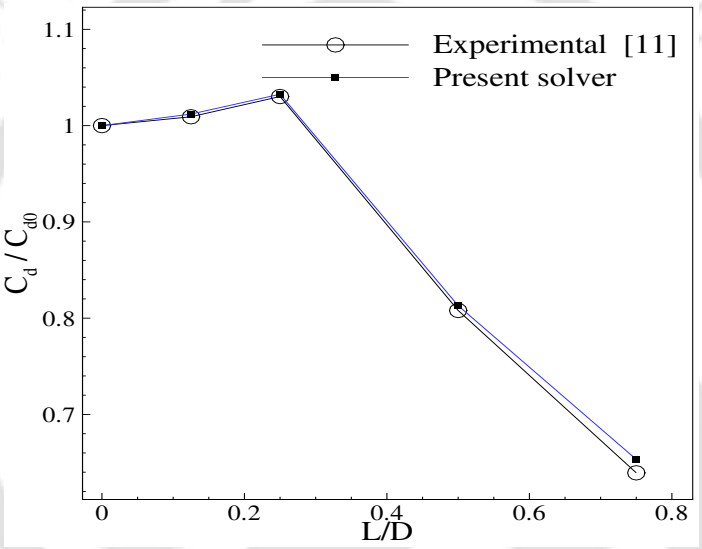

Figure 4.1: Validation with the experimental results [125]

employed for the present simulations. These grids are made sufficiently fine and adopted close to the wall so as to capture the flow physics properly. The drag force is obtained from the computations and the drag reduction/increment is compared with the corresponding experimental results for the same configuration [125]. This comparision has been shown in Fig. 4.1. It is observed that the spikes shorter than 0.25D increased the drag force, while the longer spikes (L>0.25D) reduced the drag force. Thus, the magnitude and the trend of the drag force, predicted from the present studies, are in good agreement with the findings reported in literature. Hence, the present solver has been considered for further investigations.

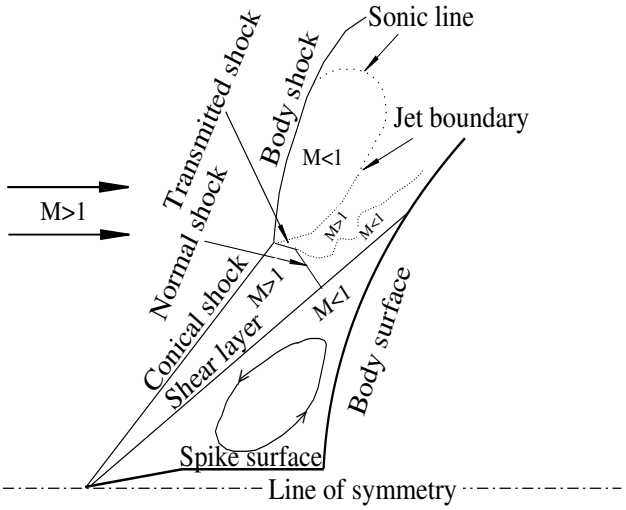

Figure 4.2: Possible Shock-Shock interaction for a spiked object

4.3 Results and discussion

4.3.1 Modification in shock structure with spike

Previous investigations have shown different S-S interaction patterns for double wedge or double cone objects. In the present study, similar phenomenon has been explored for the spiked configuration. The schematic of the flow field for such a spiked object has been shown in Fig. 4.2. A spike attachment leads to a flow separation on the spike and a reattachment on the body surface. This flow separation generates a complex shock structure and leads to interaction among them. The location and the strength of the interaction depend on various parameters like spike shape, spike length, freestream conditions, etc. For the smallest spike (L = 0.125D), no alteration in the forebody bow shock (Fig. 4.3 (b)) can be seen, since the shock stand off distance (SSOD) is 4.83 mm and the spike length is almost the same (4.85 mm). Hence, the entire spike remains in the shadow of the strong bow shock. However a small recirculation is evident at the spike base, which leads to a slight pressure decreament in the stagnation region (Fig. 4.4) in comparison to the no spike case. Further, for the spike length of 0.2D, which is greater than the SSOD, slight modification in the forebody shock (Fig. 4.3 (c)), in terms of its shape being conical, has been noticed. This oblique shock merges downstream with the bow shock and initiates a S-S interaction. At the same time, a small recirculation formed on the spike is seen to be growing and more decrement in the wall pressure is observed with respect to the previous spike length. Plateau pressure on the spike is the evidence of the extent of this increased recirculation zone

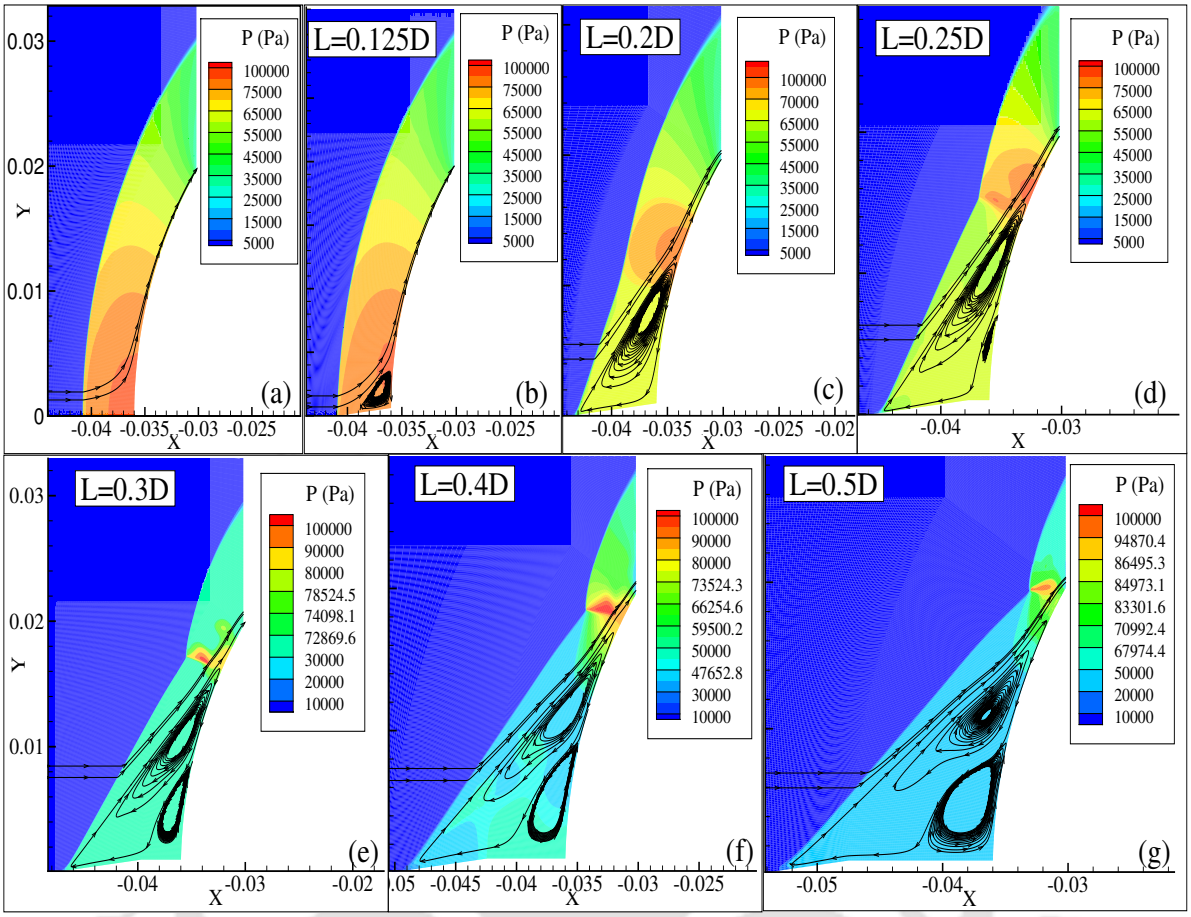

Figure 4.3: Pressure contour with recirculation zone for various spikes

(Fig. 4.4). Larger flow separation has been observed for the next spike length of 0.25D (Fig. 4.3 (d)). This spike alters the relative direction of the forebody oblique shock as well as S-S interaction. This interaction is responsible for the generation of a complex shock structure as shown in Fig. 4.5 (a). Here, the intersection of two shock waves generates a normal shock, which is oriented towards the object. This interaction increases the peak pressure on the body, which is evident from Fig. 4.4. The Mach contour for the spike length of 0.25D shown in Fig. 4.6 further elucidates this theory. Here, under expanded supersonic jet bounded by two adjacent subsonic regions can be observed. This flow pattern causes the compression of the supersonic jet due to which it undergoes alternate expansion and compression. Such shock structure corresponds to a stronger S-S interaction [96, 102]. Further increment in spike length (L=0.3D) again alters the relative orientation of both the forebody shock waves. This change shifts the interaction location further downstream; however it still retains its strength as shown in Fig. 4.5 (b) and Fig. 4.6 (b). Since the interaction of the shock waves happens closer to the object, it leads to a higher pressure on the object (Fig. 4.4). Besides, the seeding of another vortex in the recirculation zone has been observed for this spike

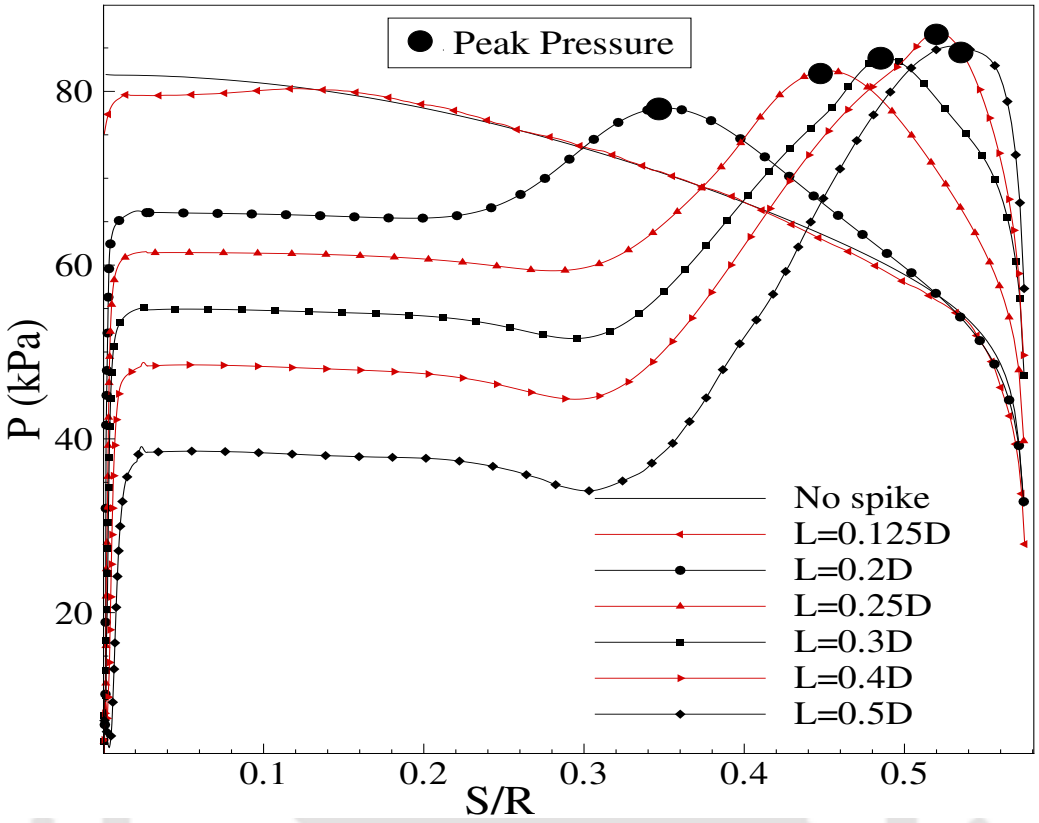

Figure 4.4: Pressure variation on the spike and blunt body

length (Fig. 4.3 (e)). The presence of this vortex rapidly decreases the pressure near the stagnation region. For higher spike length (L=0.4D), the S-S interaction shifts further closer to the body (Fig. 4.6 (c)). Such a proximal interaction along with the presence of a strong normal shock (Fig. 4.5 (c)) leads to the maximum rise in the peak pressure for this spike. On the other hand, the development of both the vortices in the dead air region leads to more flatter and lower plateau pressure on the spike surface (Fig. 4.4). Beyond this spike length (L>0.4D), bigger recirculation zone expells the conical shock wave farther from the body, which alters the relative direction of both the forebody shock waves, reconstructing a new shock at the interaction location. It is evident that the normal shock at the interaction region is replaced by an oblique shock (Fig. 4.5 (d)), which shrinks the supersonic jet bounded by the subsonic region as shown in Fig. 4.6 (d). This corresponds to a weak S-S interaction. On the other hand, higher spike length causes an interaction closer to the body generating higher pressure (Fig. 4.4). However, due to the weak interaction pattern, the peak generated pressure is found to be lower than that observed in the previous case. Beyond this spike length, the recirculation size plays a dominant role in the reduction of pressure around the stagnation region. Therefore, a prolonged plateau pressure, which is lower in magnitude is obtained on the spike surface as well as in the stagnation region for

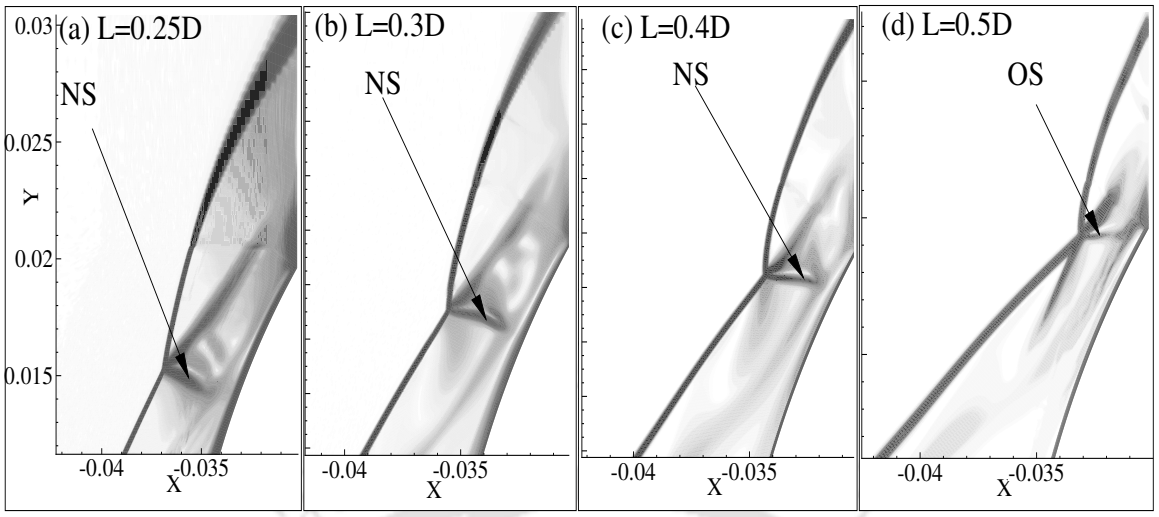

Figure 4.5: Closer view of S-S interaction from computed Schlieren image (NS: Normal Shock, OS: Oblique Shock)

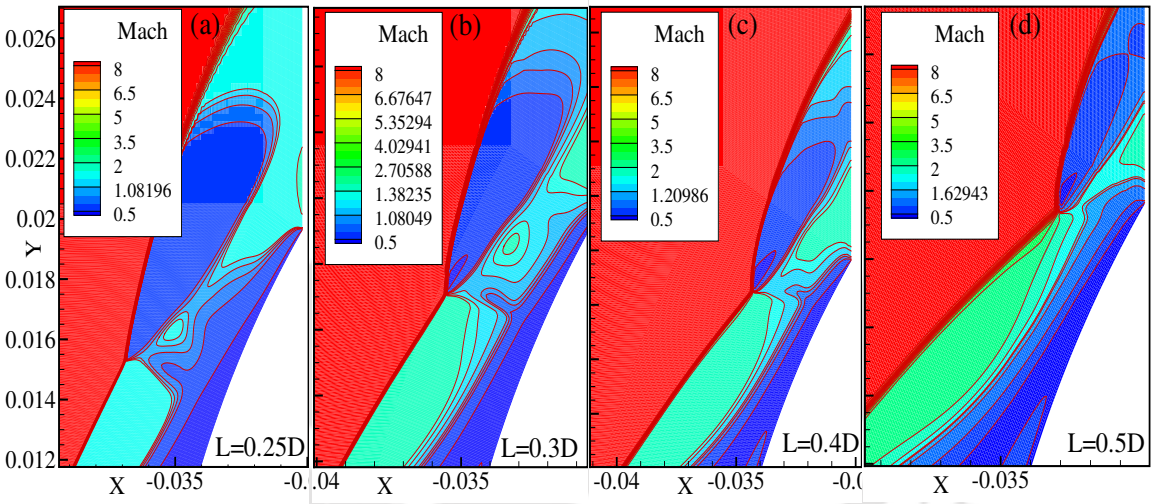

Figure 4.6: Closer view of S-S interation from computed Mach contour

all longers spikes.

4.3.2 Alteration of drag with spike length

The non-equilibrium simulation and experimental investigations show that the total drag increases for the spike lengths of L=0.125D, and L=0.25D. Here, the total drag is sum of wave drag and skin-friction drag. The simulation for L=0.125D shows a pressure decrement in the stagnation region caused by the seeding of a recirculation zone. This leads to a decrease in the computed wave drag coefficient, C_{dw}, (2.53%) for this initial spike (Fig. 4.7 (a)). However the presence of higher wall shear leads to a higher (77.32%) shear drag coefficient, C_{df}, (Fig. 4.7 (a)). The dominance of C_{df} leads to a higher total drag on the object (Fig. 4.7 (b)). It can be concluded

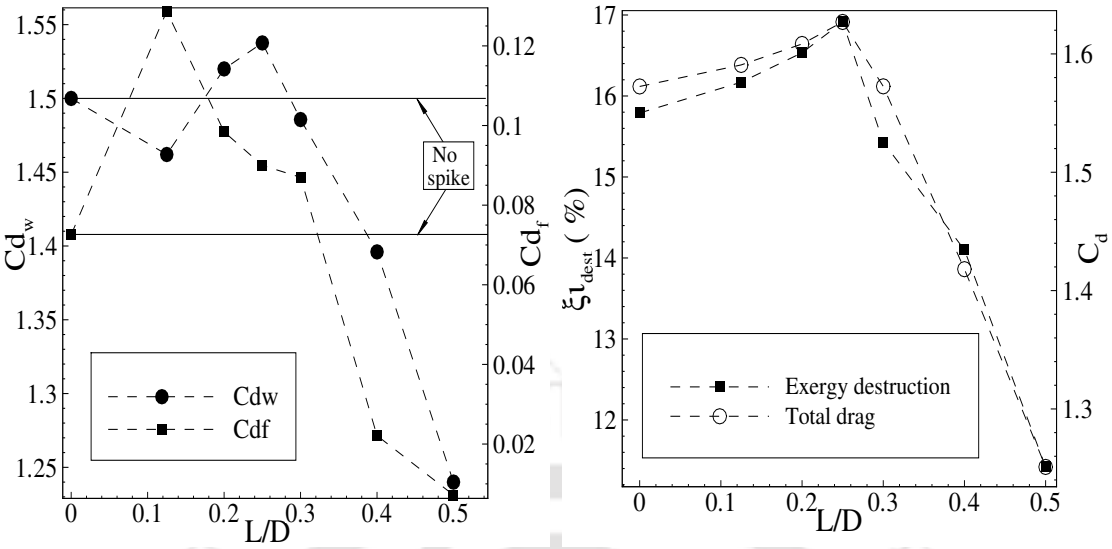

Figure 4.7: [Left] (a) Variation of wave and skin-friction drag coefficients with spike length and [Right] (b) Variation of exergy destuction (in %) and total drag (C_d) with spike lengths

that when the spike length is equal to or less than the SSOD, the skin-friction drag remains prominent. Furthermore, as the recirculation size grows with the increase in spike length, a reduction in the wall shear as well as in the C_{df} is observed. For the spike length of 0.25D, the strong interaction among the shocks leads to a maximum wave drag (1.82%), while the C_{df} is observed to be higher (24.1%) than the no spike case (Fig. 4.7 (a)). Their combined effects lead to a total drag increase of 3.5% on the body (Fig. 4.7 (b)). Thus, the total drag increase for this spike is due to the stronger S-S interactions. For L=0.3D, an even stronger interaction has been observed (Fig. 4.5 (b)). However, the seeding of the second recirculation (Fig. 4.4 (d)) along with the first bigger recirculation has been found to be decrease the body pressure near the stagnation region. This causes a slight decrement in the computed wave drag as compared to the no spike case.

Table 4.2: Details of the flow field and the drag for various spike lengths

Flow conditions	0<L<0.125D	0.125D<L<0.25D	0.25D<L<0.4D	L>0.4D
Recirculation	No (Seeding)	Yes (1, Small)	Yes (2, Developing and seeding)	Yes (2, Big)
S-S interaction	No	Initiation	Yes (Stronger)	Yes (Stronger to weaker)
Peak pressure	No	Appear	Yes (Increases)	Yes (Decreases)
Total drag	Increases	Increases	Transition	Decreases

Thus, an increment in the computed wave drag on the body has been observed until the seeding of the second recirculation bubble. After this length (L>0.3D), both recirculation zones start growing and contribute to the lessening of the pressure near the stagnation part of the object. Althoug, the peak pressure on the surface increases,

the dominance of the decreased pressure near the stagnation region reduces the total drag by 9.82%. This shows that two recirculation zones dominating the effect of the S-S interaction induce the drag reduction on the body. Table 4.2 presents the details of flow field and the drag incurred by the blunt object selected for thus study. This reveals the criterion for drag enhancement or reduction for the spiked body of various spike lengths. This study is further extended to access the performance of a spike using the thermodynamic parameter "exergy". Steady-state exergy equation has been used for the calculation of exergy destruction. Its variation with different spike lengths has been shown in Fig. 4.7 (b). This graph clearly indicates an increment in exergy destruction with an increases in the drag force for initial spike lengths. Further increment in spike length has been observed to decrease the drag as well as the exergy destruction.

4.3.3 Chance of drag reduction with a short spike

Mounting a spike is a widely accepted technique to reduce the drag force. However, the discussion in the previous section suggests that the drag force increases when the spike length is equal to or smaller than 0.25D for the present object. Nonethless,

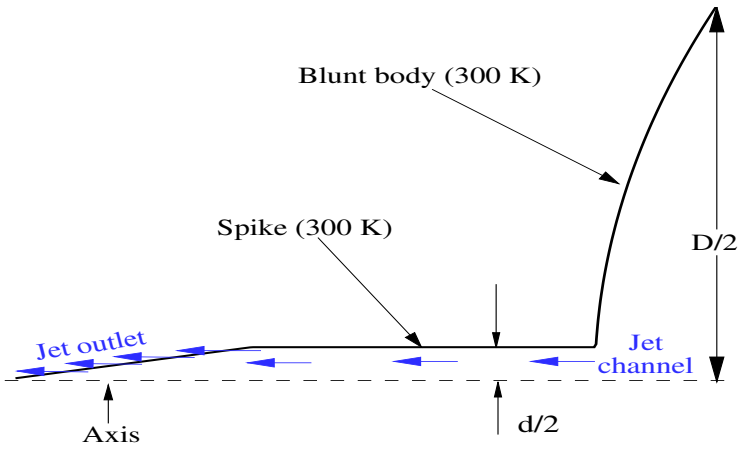

Figure 4.8: Schematic of the jet channel for spike with jet case

this length can serve as a better alternative to increase the drag for applications like aerobraking. Although, the spikes longer than this critical length are required for cruise or launch vehicles to achieve a drag reduction. However, in case an active drag reduction technique is integrated with a passive one, the same smaller spike can be used to achieve the drag reduction as well as the drag increase depending on the activation strength. For this objective, a counter-flow jet based drag reduction technique is integrated within the spiked body (Fig. 4.8). Here, the strength of the jet is de-

fined using the jet pressure ratio (pr) as a ratio of the total pressure of the jet (P_{0j}) to the freestream pitot pressure (P_{0f}). The root of the spike is selected as the jet enterance and spike tip is serve as the jet outlet of this integrated configuration. The jet is injected at an angle of 0 degree to the base. Simulations are carried out with a sharp spike of a length of 0.25D, the unit Mach of jet is used with the jet strength or pressure ratio of 5. For this, the computed Mach contour has been shown in Fig. 4.9 (a). Due to the addition of the jet, the expansion of the flow takes place at the spike

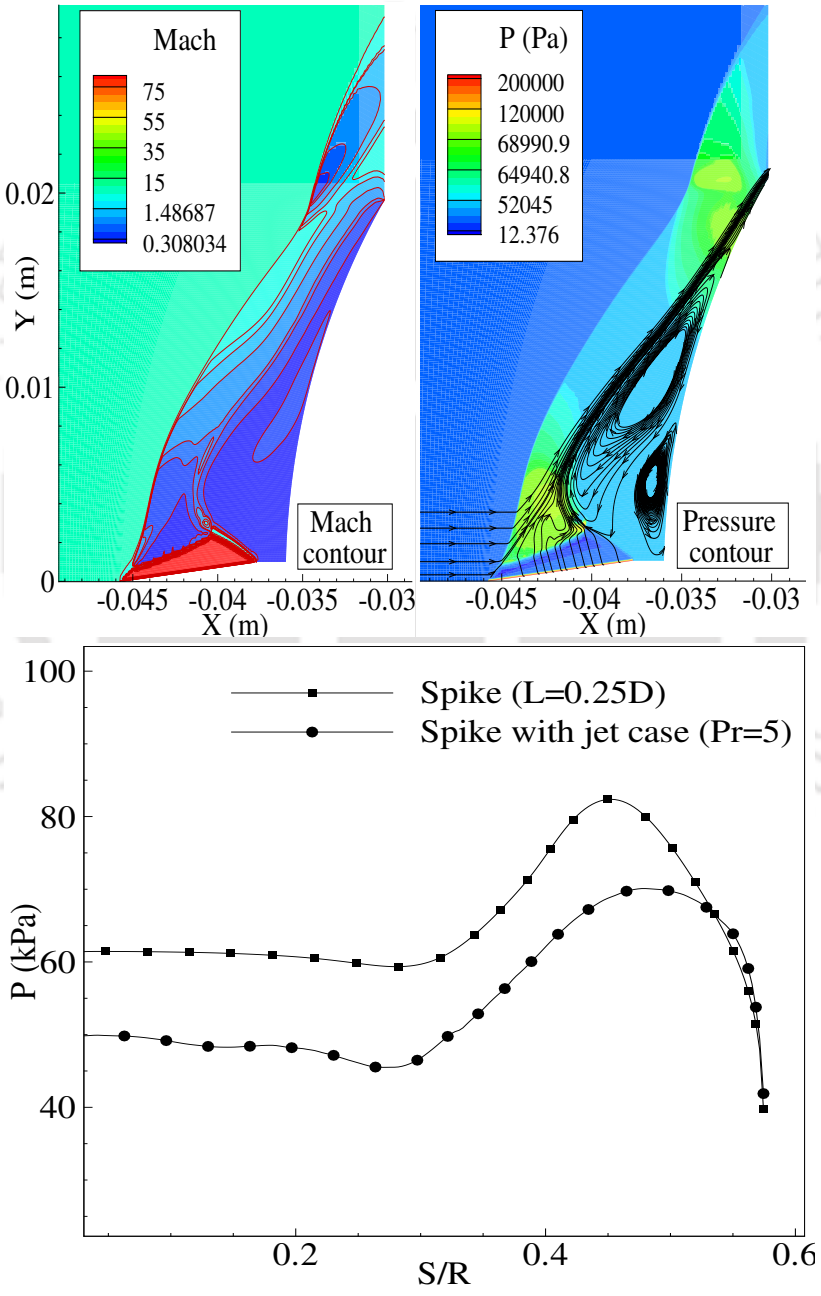

Figure 4.9: [Top] (a) Mach and pressure contours for spike with jet case and [Bottom] (b) Comparison of wall pressure for a spike and spike with jet case

tip. This expansion increases the Mach number and deflects the conical shock wave

away from the body. From the pressure contour (Fig. 4.9 (a)), it can be seen that there are two vortices for this arrangement, while a single vortex structure has been noticed for the sole spike arrangement (Fig. 4.3 (d)). Thus, the integration of spike with jet suppresses the strong S-S interaction observed for the sole smaller spike. This change has led to the restructuration of the shock waves and weakening of the S-S interaction. Such alteration in the interaction pattern decreases the peak pressure on the surface, as shown in Fig. 4.9 (b). Further, the object experiences less pressure due to the generation of two vortices in the stagnation region. For this arrangement, the magnitude of the total drag reduction is 16.50% for the jet pressure ratio of 5 with this spike. Hence, it can be considered that the addition of a jet with a short spike is equivalent to attaching a larger spike to a blunt object.

4.4 Conclusions

Present computational investigations are carried out to understand the gas dynamic reasons behind the increment of total drag force with short spike. Simulations with the in-house viscous non-equilibrium solver for the spike of lengths 0.125D, 0.2D, and 0.25D, attached to a blunt object, showed a drag force increase. In case of a spike shorter than the SSOD (L=0.125D), despite the wave drag reduction, a frictional drag increase has been observed to be increasing the total drag force. For other spike lengths, the drag force alteration has been noticed due to two reasons i.e. the increase in the wall pressure due to S-S interaction and the presence of a low pressure recirculation region. For other short spikes (L=0.2D and L=0.25D), a strong S-S interaction has been accounted responsible for the increase in the wave and friction drags. In case of a shorter spike, an increase in the length till 0.25D helped to grow a recirculation bubble, but brought the strong S-S interaction towards the surface and led to a drag force increment. The exergy destruction has also been observed to be higher for these spike lengths (L<0.25D). The appearance of a second recirculation bubble for the spikes longer than 0.25D leads to a larger overall dead air zone and thus weakens the S-S interaction. Therefore, drag reduction has been noticed for these spike configurations. The flow field, supported by these spikes, actually reduced the exergy destruction. It has also been noticed that if an integrated active drag reduction technique like a counter flow injection can weaken the S-S interaction, it can also help to reduce the drag for short spikes, which otherwise increase the drag force.

CHAPTER 5

EVALUATION OF DRAG FOR SPIKES OF DIFFERENT GEOMETRY AND SPIKE WITH JET IN NON-EQUILIBRIUM HYPERSONIC FLOW

The drag offered by a spike on a blunt object solely depends on the length of spike as well as the shape of the spike tip. Hence, this chapter is devoted to investigation of the drag force for various shapes of spike tip. For this three different shapes of the spike tip such as spherical or rounded, sharp or conical and flat tip are selected for the drag force calculation in reacting hypersonic flow. The length of spike (L) is kept as $1.5D$ *which is same for all spike tips. Both lower and higher freestream stagnation enthalpies are considered herein for checking the performance of the spike in reacting environment. It can be noted that flat tipped spike is more effective for higher drag reduction as compared to other spikes at same freestream conditions. Novel combination of two drag reduction techniques, such as spike with counter-jet, is also studied for higher drag reduction while using shorter spike (*L*=*$0.5D$*). The studies showed that even small pressure ratio (*PR*=*0.1*) gives larger drag reduction for this integrated unit. Different diameters of the jet are also considered for better performance of the spike at fixed enthalpy.*

Kumar S. and Kulkarni V. "Evaluation of Drag for Spikes of Different Geometry and Spike With Jet in Non-equilibrium Hypersonic Flow", (Under preparations)

5.1 Introduction

High speed vehicle always suffers from the high temperature effect due to enormous conversion of the kinetic energy into heat energy near its vicinity. Hence, such vehicles are designed with blunt shaps to lower the surface heating load or heat flux. But, this advantage has a cost of higher wave and frictional drag on the blunt object. Therefore drag reduction also remains a topic of investigation for hypersonic flow regimes. Among the various methods of drag reduction, mounting a metallic spike at the stagnation point is simple and cost-effective to implement. In the presence of a spike, strong bow shock wave gets converted into weak shocks around the blunt object. This modification helps in reducing the pressure on the body and hence the wave drag. Numerous researches have worked in both experimental and numerical fields for spiked body aerodynamics at supersonic as well as hypersonic flow regimes. Studies with spikes of different shape [[35] - [52] - [53]] are also reported for the spike-based passive drag reduction technique.

Various experimental and numerical explorations are part of the open literature that studies the spike-based drag reduction technique in the supersonic/hypersonic flow regimes. Most of the studies focused on different spike lengths and various freestream parameters for their objectives. Further, the investigations from the numerical perspective have an assumption of the calorically perfect gas flow. But, lesser attention is noticed about the performance alteration of a spike in the presence of real gas effects. Hence, the main objective of the present investigation is to study the flowfield alteration and drag reduction by using various spike shapes in the reacting environment. In this regard, three different shapes of the spike tip such as spherical, conical and flat are considered herein. Different freestream stagnation enthalpies are accounted to demonstrate the real gas effects on the flow field and drag force. The performance in terms of drag reduction is compared and presented to ensure the better shape of the spike in reacting hypersonic flow conditions. Further, the combination of two drag reduction techniques is also studied for the greater magnitude of the wave drag reduction. For this, the spike-based passive drag reduction method is integrated with the counter-flow jet based active drag reduction technique. Different jet diameters are considered for their effect on the drag reduction on the blunt-body. The non-equilibrium flow solver discussed earlier is employed for these studies.

5.2 In-house solver validation

The geometry for validation of the present solver is taken as spherical object of radius 20 mm. A cylindrical shape of spike is fitted at the stagnation point of this object.

The length of the spike is taken as 1.5 times the diameter of the blunt object. The tip of the spike has spherical shape with the base diameter equal to 10% of the object diameter. Freestream conditions used for present validation have hypersonic flow of

Table 5.1: Details of freestream conditions

Mach number	Pressure (Pa)	Temperature (K)	Y (N_2)	Y (O_2)
6.0	525.6898	54.87	0.765	0.235

Mach number 6.0. Details of the inflow conditions are mentioned in Table 5.1. The same object with spike and freestream condition was considered by Kalimuthu [132] for their experimentation. In the current simulation, symmetry boundary condition is applied at the axis of the spherical object. Further, No-slip isothermal wall (300 K) boundary condition is imposed for the spike and body surface. Initially, simulation is carried out for spherical object or spike-off case for which magnitude of drag coefficient (C_d) is obtained as 0.91. The spherical tipped spike of length 1.5D is attached at the

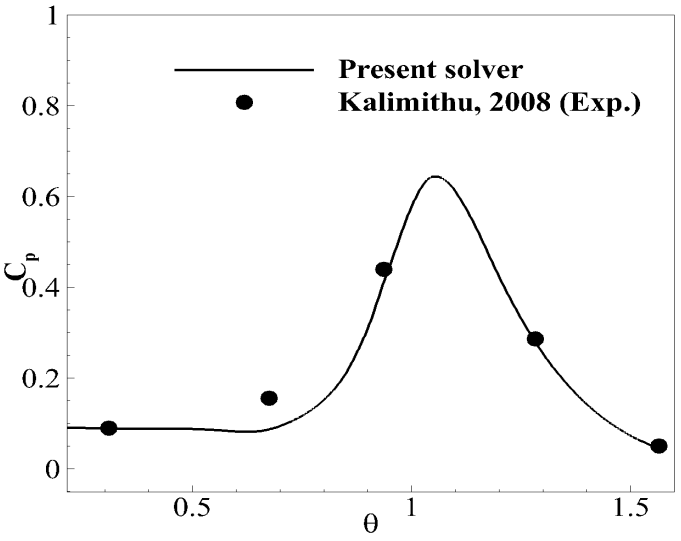

Figure 5.1: Validation of present solver with the experimental results

stagnation point of this object, i.e. spike-on case, during the second set of simulations. The obtained results in terms of variation of pressure coefficient along the surface are compared with the corresponding experimental results (Fig.5.1). It can be seen that results obtained by the present solver are in better agreement with the experimental results [132]. The drag coefficient (C_d) is also calculated and it is found to be 0.261 for this spike test case. Further, the experimental value of C_d for the spike-off and spike-on test cases are 0.90 and 0.268 respectively for the same freestream conditions. There is drag reduction of 70.70% after the spike attachment, which is same as the

experimental observations and present numerical predictions. Thus computed results match very well with the experimental results.

5.3 Grid independence study

A structured grid domain is selected for the present finite volume-based viscous compressible flow simulations. Different grid sizes are considered herein for the grid independence studies. The object size, spike shape and freestream conditions are same as discussed above. Four different sizes of grids viz Grid 1 (121422 Nodes), Grid 2 (224682 Nodes), Grid 3 (368050 Nodes) and Grid 4 (518599 Nodes) are taken. The surface pressure (in kPa) is computed for all the grids and plotted for its variation along the spherical surface (Fig. 5.2). It can be seen that the surface pressure variations obtained for Grid 3 and Grid 4 are approximately same. Such grid independence tests are performed for other spiked geometries as well and the grid independent results are considered for further analysis.

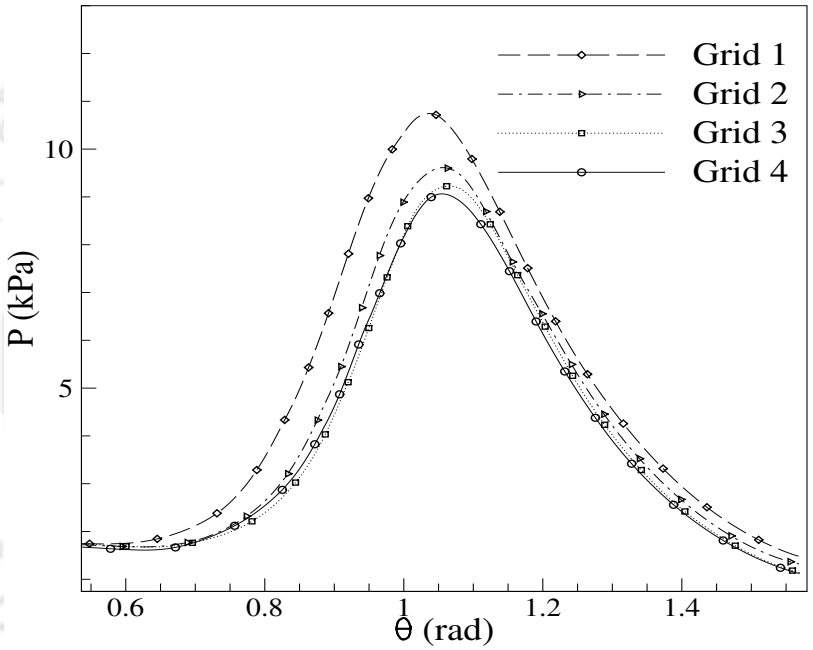

Figure 5.2: Grid independence study for the spherical tip spike body

5.4 Results and discussions

5.4.1 Flowfield with spike of spherical tip

Initially round ended spike of length L=1.5D and base diameter 5% of object diameter is selected for the flow modification around the blunt object. Different freestream stag-

nation enthalpies are considered herein for the computation of the drag force. Higher enthalpy is considered by increasing the freestream temperature only which is shown in Table 5.2. The freestream Mach number and the static pressure is taken as constant for all enthalpies which are 6.0 and 525.69 Pa. Simulation for lower freestream stagnation enthalpy (FSE) case (0.45 MJ/Kg) shows that there is early separation

Table 5.2: Different freestream conditions for the simulation of reacting flow

No.	T_∞ (K)	P_∞ (Pa)	Mach No.	H_0 (MJ/kg)	Y (O_2)	Y (N_2)
1	54.87	525.69	6.0	0.45	0.235	0.765
2	242.69	525.69	6.0	2.00	0.235	0.765
3	500.00	525.69	6.0	4.00	0.235	0.765

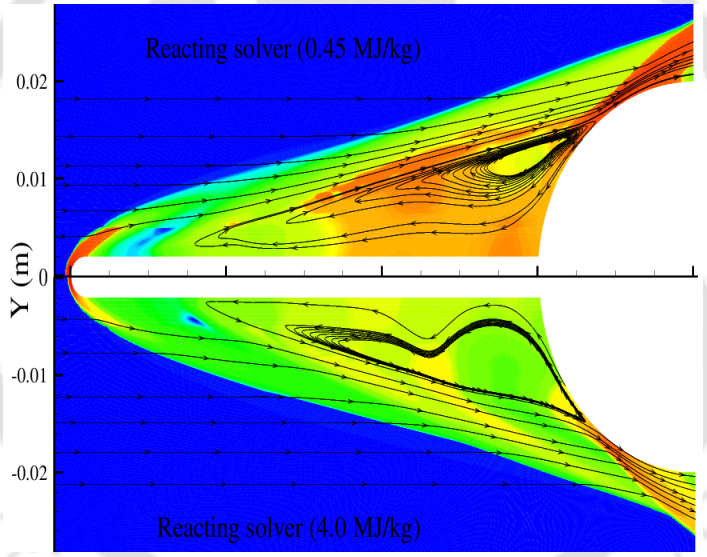

Figure 5.3: Pressure contour for the spherical end spiked body.

of flow from the spike tip. This ensures the presence of recirculation zone and decrement of the pressure as shown in pressure contour Fig. 5.3. Further, higher FSE (2.0 MJ/Kg and 4.0 MJ/Kg) reconstructs the shock structure, for the same spike, and delays the flow separation on the spike surface. This phenomenon leads to early impingement of shock on the blunt-body. Thus the appearance of conical shock wave is delayed for higher stagnation enthalpy condition. This reconstruction of shock due to decrease in the size of the recirculation zone near the stagnation region can be seen from the pressure contour (Fig. 5.3). These alterations in the flowfield are because of the consideration of temperature-dependent specific properties in the real gas flow solver. Moreover, various dissociation and recombination chemical reactions also lead to the downstream shift of the separation shock and thus available space for recir-

culation is lesser for the higher enthalpy case as compared to the lower one. These changes in the flow structure are sufficient to alter the surface pressure and drag force. Here, coefficient of the pressure (C_p) is evaluated by the ratio of difference in surface pressure & freestream static pressure to the freestream dynamic pressure and formulated as $C_p = 2(P - P_\infty)/(\rho_\infty {U_\infty}^2)$. The variation of the C_p is plotted for all the FSE cases in Fig. 5.4. It should be noted that the pressure on spherical object increases with higher FSE. This increase in surface pressure is seen at all the locations of the

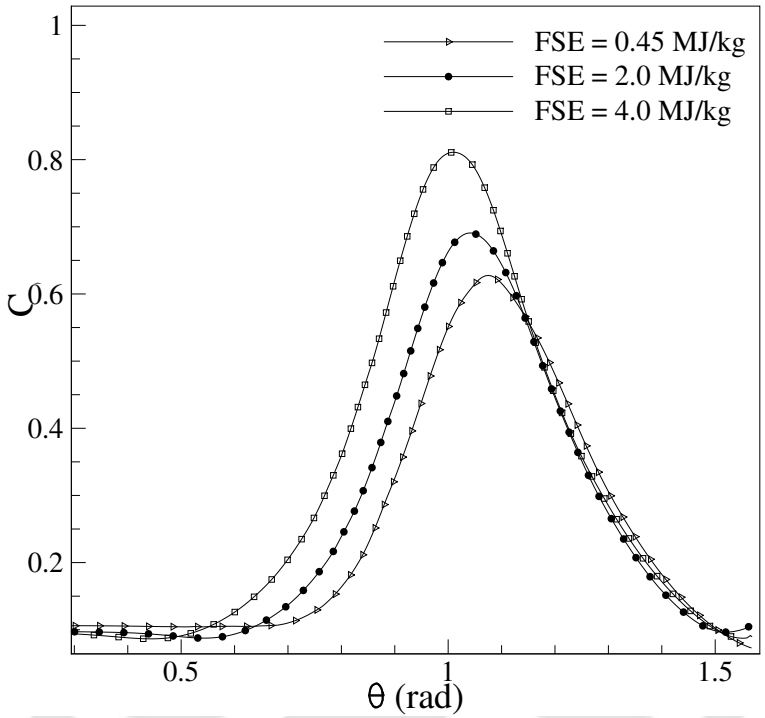

Figure 5.4: Surface prerssure variation for rounded tipped spike.

spherical object which includes the reattachment also. The enhancement of pressure is sufficient for the increase in wave drag force on that blunt body. The drag force is 3.98 N, 4.45 N and 5.66 N for the FSE of 0.45 MJ/Kg, 2.0 MJ/Kg and 4.0 MJ/kg respectively. It can be observed that there is 42.20% increment in the drag force for higher FSE of 4.0 MJ/kg in the presence of a spike. This shows that the effectiveness of the round-ended spike decreases for the real gas flow at higher FSE consideration.

5.4.2 Flowfield with spike of conical tip

Investigations are further extended for the wave drag prediction with a conical tipped spike. The semi-apex angle of the spike is taken as 10° and spike length (L) is taken as 1.5D. Same lower and higher FSE cases are considered here as well which are discussed earlier for fixed Mach 6. Higher FSE leads to downstream shift of the conical shock wave as compared to lower FSE (0.45 MJ/Kg). As a result, the size of low-density

gas region gets decreased for higher FSE (4.0 MJ/Kg). This decrement offers higher pressure on the blunt object as well as on the spike surface. The Fig. 5.5 shows variation of surface pressure (C_p) for all three enthalpy cases. The trend of pressure variation is consistent with the spherical tipped spike mounting. However, the magnitude of surface pressure at every point is higher for all enthalpy cases as compared to the spherical tipped spike case. Such higher surface pressure offers higher drag force for

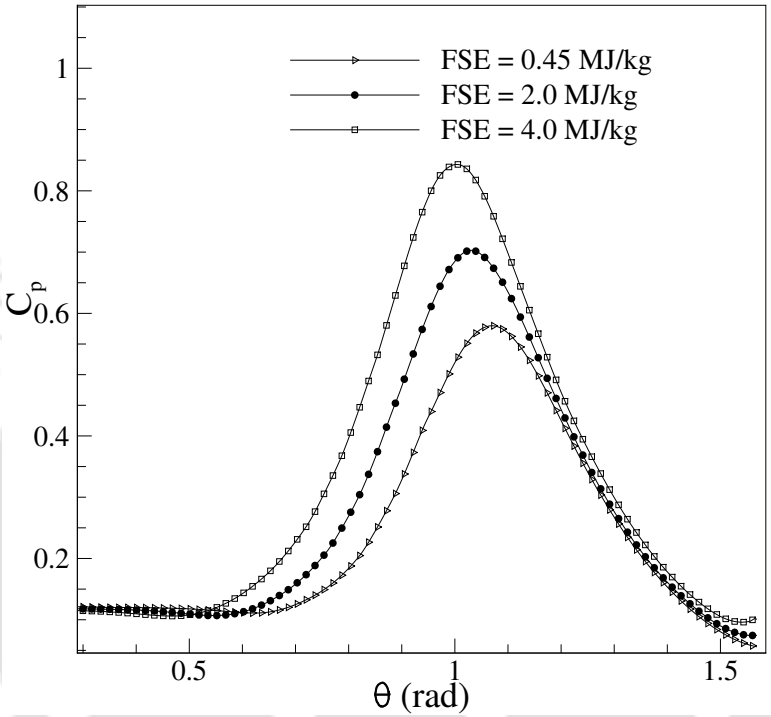

Figure 5.5: Surface prerssure variation for conical tipped spike.

the conical spike case. The calculated wave drag for initial enthalpy case (0.45 MJ/kg) is 3.84 N while for the higher enthalpy (4.0 MJ/kg) case it is 5.96 N. There is 54.40 % increment in the drag force for higher FSE condition when spike tip is of conical shape. It can be concluded that the degradation in the performance of conical ended spike is more than the spherical ended spike for the higher FSE case.

5.4.3 Flowfield with spike of flat tip

Studies are further carried out for the same body but with spike end condition as flat. The same length of spike i.e. L = 1.5D is taken and investigated for the same freestream condition as mentioned above. A similar effect on the flow field is observed with this spike shape. The conical shock wave and the size of recirculation zone are altered with FSE as seen already. The plots of co-efficient of pressure with various FSE are shown in Fig. 5.6. The trend of the pressure profile is consistent with the previous cases of spike. But, the magnitude of the pressure at all locations of the

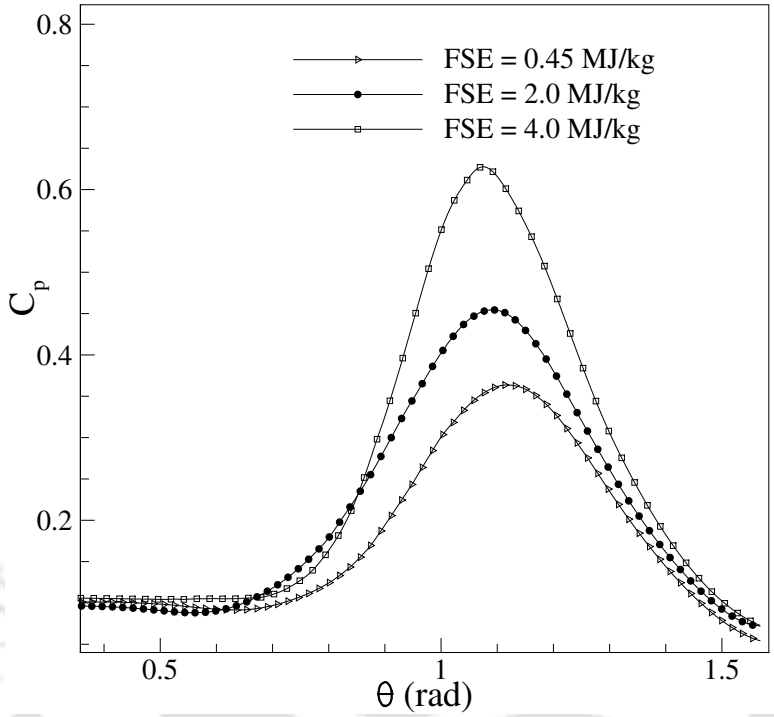

Figure 5.6: Surface prerssure variation for flat tipped spike.

object is lesser as compared to the spherical and conical tipped spikes. This reflects larger recirculation size, in the stagnation region, in the presence of flat ended spike as compared to other two spikes. The incurred drag forces are 2.2 N, 2.9 N and 3.88 N for the FSEs of 0.45 MJ/Kg, 2.0 MJ/Kg and 4.0 MJ/Kg respectively. This magnitude of the drag force is lower than the previously considered spikes. Here as well increment in the drag force by 76.36% is noticed when FSE is increased from 0.3 MJ/kg to 4.0 MJ/kg.

5.4.4 Comparision of spike shapes

Higher FSE leads to increases in the pressure and thus drag force on the spherical object. However, we have to select one spike shape for better performance. Because of this, the surface pressure profile for all three spikes is compared for the highest enthalpy condition of 4.0 MJ/Kg as shown in Fig. 5.7. It can be seen that a conical-ended spike offers highest pressure and a flat-ended spike offers lowest pressure on the spherical object. Also, the magnitude of the reattachment or peak or maximum pressure is lower for the flat-ended spike as compared to the other two. These differences are due to the size variation of the recirculation zone near the stagnation region. Further, percentage wave drag reduction is calculated for all three spike shapes at the initial enthalpy case. It can be noted that there is 70.70%, 68.5% and 78.87% reduction in the wave drag for the spherical, conical and flat-ended spikes respectively. Here,

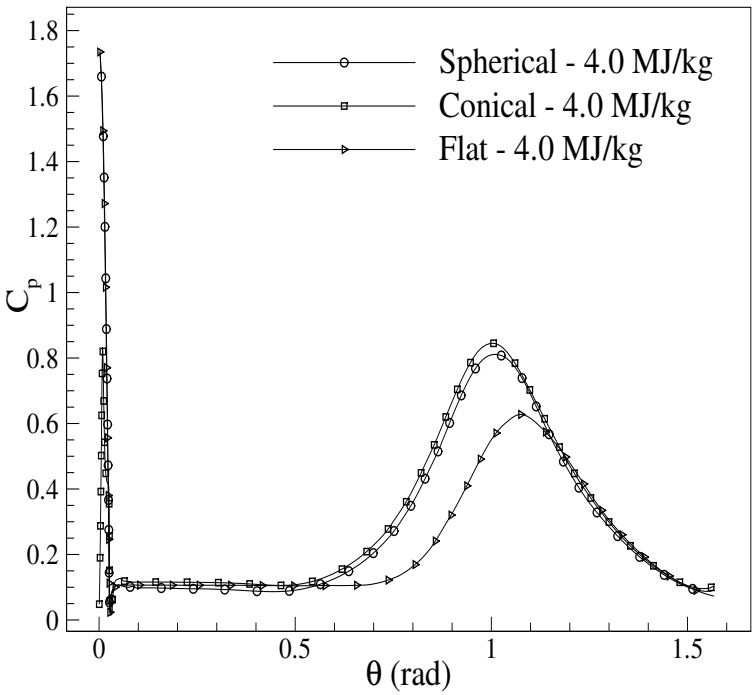

Figure 5.7: Effect of real gas on coefficient of pressure for the different tip of spike at H_0=4.0 MJ/kg

flat-ended spike shows better performance as compared to all other spikes at lower freestream stagnation enthalpy situation (0.45 MJ/Kg). In addition to this, wave drag is calculated for all other higher enthalpies (2.0 MJ/Kg and 4.0 MJ/Kg) also (Table 5.3). It is observed that all spikes predict consistently higher drag coefficients (C_d) with the higher FSE. Thus percentage drag reduction, for all spikes, reduces for higher FSE cases as compared to the lower one. The magnitudes of drag reduction for the round, conical and flat-ended spikes are 67.97%, 66.51% and 74.15%. for the

End conditions	Spherical		Conical		Flat	
h_0	C_d	C_d%	C_d	C_d%	C_d	C_d%
0.45 MJ/kg	0.267	70.70	0.277	68.5	0.118	78.87
2.0 MJ/kg	0.285	67.97	0.289	66.51	0.23	74.15
4.0 MJ/kg	0.343	61.46	0.361	59.31	0.273	69.32

Table 5.3: Drag reduction at various freestream stagnation enthalpy (H_0) for the different end conditions of the spike

intermediate enthalpy of 2.0 MJ/Kg. While for highest freestream enthalpy case (4.0 MJ/Kg) it is 61.46%, 59.31% and 69.32% for the respective cases of the spike. All spikes degrade their drag reduction efficiency in the higher enthalpy flow. But this degradation is lowest for the flat-ended spike which is followed by the spherical and

conical ended spikes. Thus it is advisable to choose flat-ended spike as a better drag reducing device at higher FSE situations of reacting hypersonic flow.

5.4.5 Combination of spike with counter-jet

Mounting a stagnation spike is a conventional technique for drag reduction on the blunt object. For larger drag reduction, a long spike is needed to be attached at the stagnation point of the body. This may lead to the introduction of instability issues of the object. Therefore, the idea of greater magnitude of the drag reduction is introduced with the use of a shorter spike. For this, a novel combination method of active and passive drag reduction techniques is presented. Stagnation spike of length 0.5D and counter flow jet are integrated into a single unit for this purpose. The geometry of blunt object and spike are kept as same as discussed in the above sections. The freestream conditions are also same as given in Table 5.1. The pressure ratio or the jet strength (PR),the total pressure of the jet to the freestream total pressure, is kept as 0.1 with unit Mach number of the counter-jet. The jet is 1.5 mm offset from the stagnation point location, or adjecent to the spike root, and outlet direction is the parallel to the horizontal axis. Various jet diameters are used (0.5 mm, 1.0 mm and 2.0 mm) for better wave drag reduction. The initial shock structure for the fixed spike length (L=0.5D) is shown in Fig. 5.8 (a) for lower stagnation enthalpy of 0.3 MJ/kg. Here, the spike separates the flow which then reattaches on the object surface with two recirculation zones at the stagnation region. The conical shock wave is very near to blunt object due to early reattachment of the flow and thinner shock layer which leads to closer shock impingement on the object. While for the integrated unit, as shown in Fig. 5.8 (b), the conical shock gets pushed by the jet which introduces larger recirculation zone which delayed flow reattachment and thicker shock layer for the same spike length. This reconstruction leads to farther impingement of the shock on the blunt-body. These alterations in the flow field bring in lower surface pressure for the spike with jet case as compared to only spike case (Fig 5.9). There is 3° upstream shift of the impingement location with 56.25% decrement in the peak pressure for the integrated case. The computed drag co-efficient for the spike and integrated case are observed as 0.73 and 0.52 respectively. Here, 18.90% and 42.22% decrement in the wave drag for the respective cases at lower FSE of 0.45 MJ/kg has been registered. It can be noted that very small pressure ratio of the jet (PR=0.1) leads to a significant reduction in the wave drag for integrated case with jet diameter of 0.5 mm.

Larger jet diameters used are d=1.0 mm and d=2.0 mm for higher wave drag reduction with the same jet pressure (PR=0.1) and spike length (L=0.5D). The comparison of the streamline for the lowest and highest jet diameter is presented in Fig. 5.10

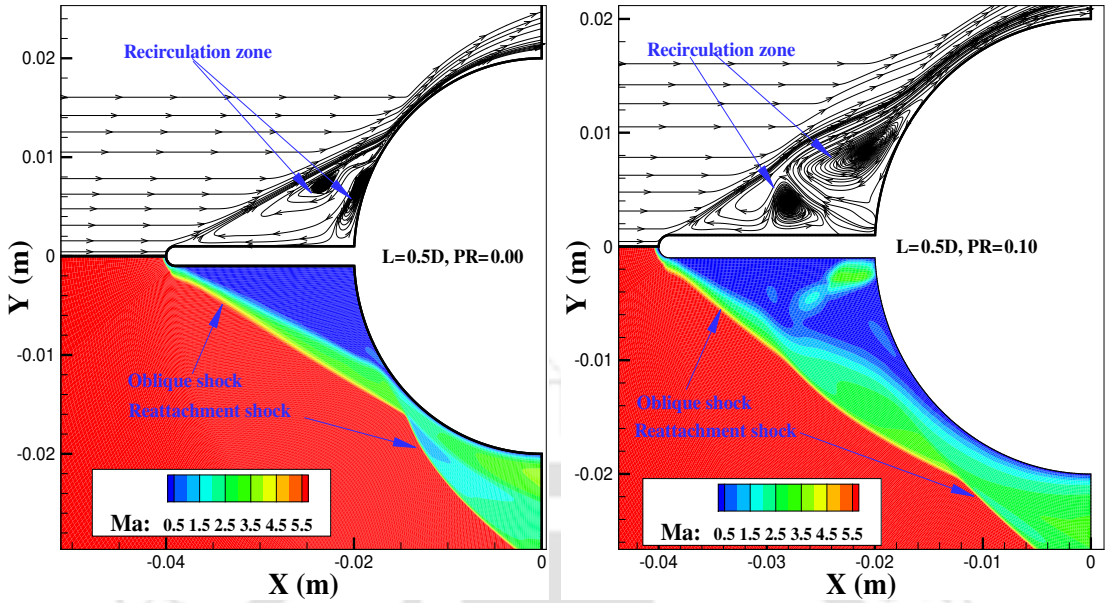

Figure 5.8: [Left] (a) Streamline and Mach distribution for spike only (L=0.5D) and [Right] (b) Streamline and Mach distribution for spike with counter-jet

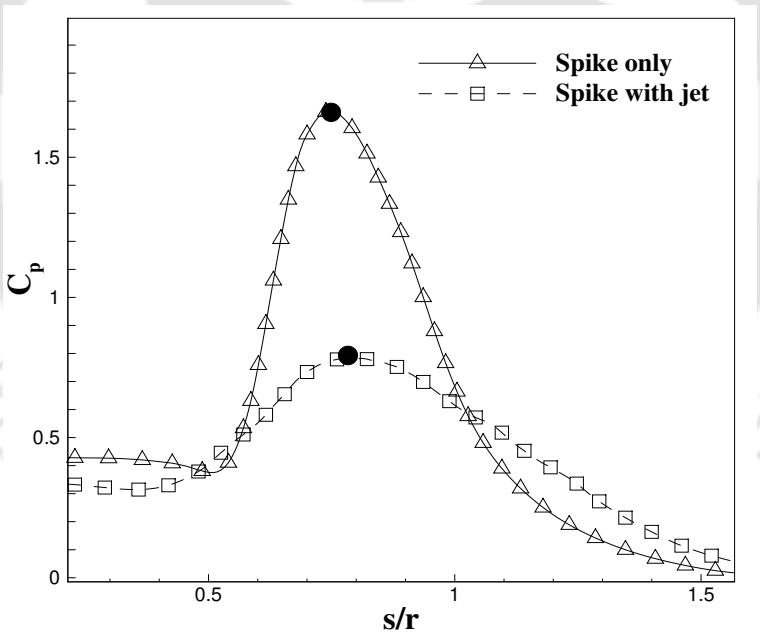

Figure 5.9: Effect of the jet on the surface pressure

(a). This figure shows three recirculation zones for d=2.0 mm case. This increment provides larger space for the low-density gas at the stagnation which leads to the decrease in the Mach number at the surface as shown in Fig. 5.10 (b). It can be seen that there is thicker shock layer near the impingement location for higher jet diameter. These alterations provide consistent decreases in the peak or reattachment pressure, as well as pressure at all locations of the object as shown in Fig. 5.11. Since higher mass flow rate of the gas is emitted through the increased jet diameter therefore weaker

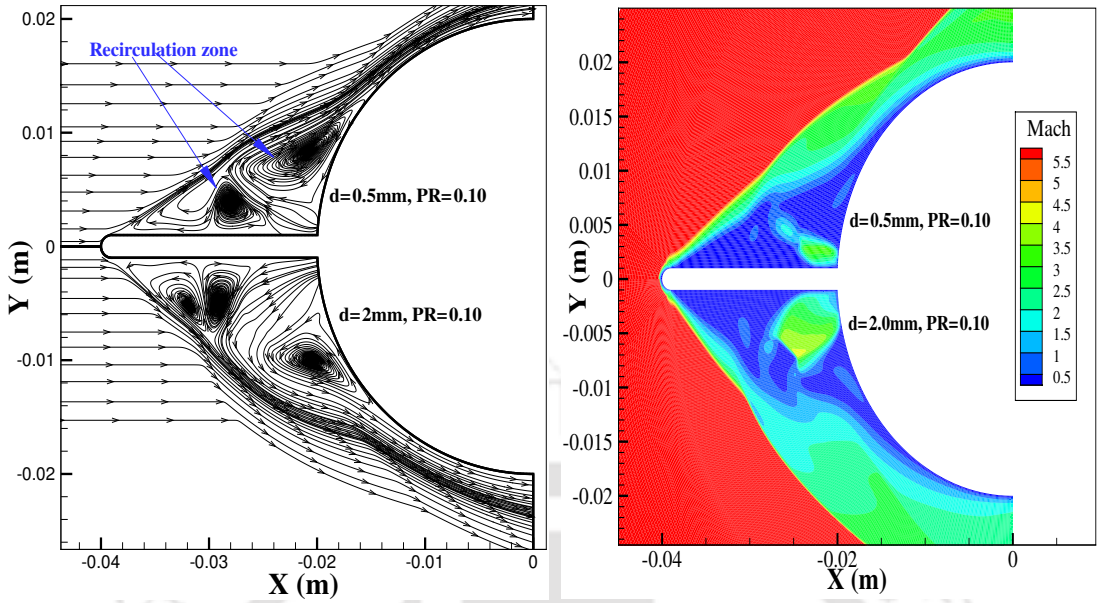

Figure 5.10: [Left] (a) Streamline and [Right] (b) Mach contour for jet of different diameter

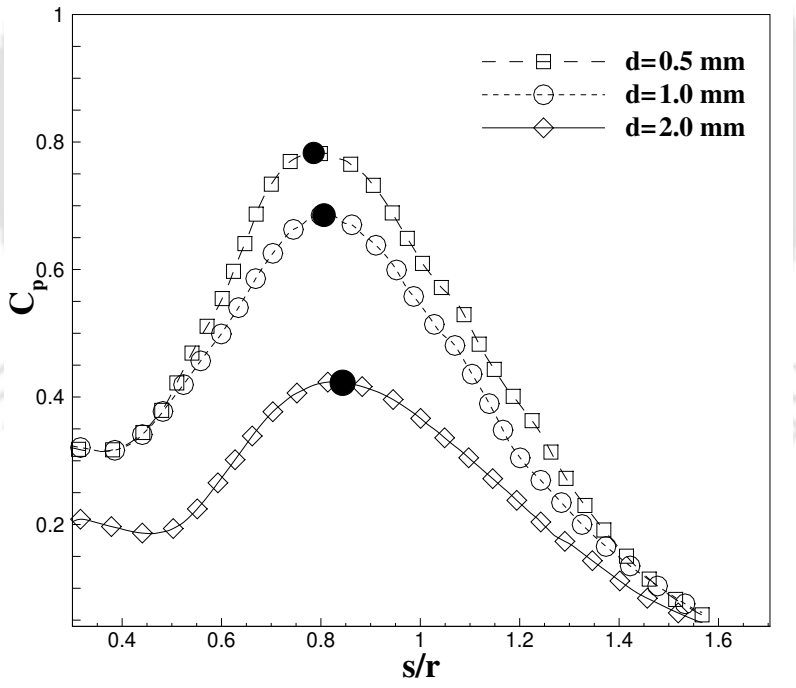

Figure 5.11: Effect of the jet dimeter on the surface pressure

conical shock is observed. The computed drag coefficient (C_d) is 0.52, 0.46 and 0.30 for the jet diameter of 0.5 mm, 1.0 mm and 2.0 mm respectively. Here, 66.67% drag reduction is noted for larger diameter of the jet.

5.5 Conclusion

Present investigations are carried out for the drag reduction of a spherical body by considering different spike shapes. Three shapes of the spike tip are selected such as spherical or round, flat and conical. The length (L=1.5D) and base diameter (2.0 mm) of all spike shapes are kept same but for different FSEs. Initially, simulations are carried out for lower FSE which resembles with the calorically perfect gas assumption. For this, drag reductions noted are 70.70%, 68.5% and 78.87% for the spike with spherical, conical and flat tips respectively. Here, the flat spike tip shows higher drag reduction as compared to other two spikes at lower stagnation enthalpy. However, there is decrease in the drag reduction for intermediate stagnation enthalpy condition which is up to $2-5\%$ for all three cases. Moreover, there is decrease up to $9-10.5\%$ in the computed drag force as we increase the enthalpy to 4.0 MJ/kg. However, in these reacting flows spike with flat end bears more efficiency in drag reduction (69.32%) in comparison with the conical (59.21%) and spherical ended spikes (61.46%). The novel integration method of drag reduction technique shows that larger wave drag reduction can be achieved by relatively shorter spike. The integration of spike with jet shows 42.22% reduction in the wave drag force. However, the magnitude of this reduction can be increased with larger diameter of the jet for same freestream conditions.

CHAPTER 6

AN EFFECTIVE MEANS OF DRAG REDUCTION IN HIGH ENTHALPY FLOW THROUGH UNSTEADY ENERGY DEPOSITION

*Prime objective of this chapter is to assess the performance of unsteady energy and steady energy depositions in the reacting flow. Both perfect gas (PGS) and reacting gas solvers (RGS) are used for this analysis. It has been noted that RGS based predictions show lesser stagnation pressure and thus wall pressure at the same interaction time. It has also been found that better drag reduction depends on the strength of low-density vortex which is formed due to the interaction between shock wave and blast wave. This vortex is stronger for the perfect gas case and thus portrays higher reduced propulsion energy or power effectiveness as compared to RGS based prediction. Simulation with the higher freestream stagnation enthalpy (*3.0 *MJ/kg) shows that there is around* 90% *decrement in the density of the energy pulse as compared to lower enthalpy case (*0.3 *MJ/kg). However, there is* 60.5% *increment in the pressure of cell or outer part of the pulse as compared to* 0.3 *MJ/kg case. Further, the diameter of the pulse also increases by* 19.10% *for this higher freestream enthalpy condition. It has been noticed that lower density of the pulse leads to the formation of stronger vortex and thus deepens the first valley of drag signal with increases in the freestream stagnation enthalpy. The formation of such stronger vortex, introduces one more valley in the drag signal for* 3.0 *MJ/kg case, where,* 152% *higher power effectiveness is registered. But, for steady energy deposition power effectiveness decreases with the inlet stagnation enthalpy. The drag plot showed that the magnitude of drag force is high at the time of shock reflection and this increment is enhanced at higher enthalpy case. Further, the drag reduction is seen for a very short interval of time for a single energy pulse. Hence, the trade-off*

between drag force and reduced or propulsion energy is also investigated. Increased magnitude of negative reduced energy, as well as drag reduction for a very short time, are seen to lower the effectiveness of the blast wave. Therefore, repetitive energy deposition is implemented to prolonge the drag reduction duration as well as to lessen the negative propulsion energy for the same freestream conditions. Higher strength of a single pulse is equally split into multiple pulses for the periodic or repeated deposition. This split helped to reduce the higher drag force as well as achieved the prolonged-time of drag reduction. Further, energy efficiency is also presented, for single as well as periodic pulse energy deposition, for different upstream locations and various higher freestream stagnation enthalpy conditions.

6.1 Introduction

Major problem of the high-speed space vehicles is the enhanced drag which can be accounted due to the presence of strong fore-body shock. Various investigations are performed and techniques are developed to reduce this drag force. As an outcome of these, two techniques namely structured or passive and unstructured or active are available for possible implementation. Few researchers considered mounting of a physical spike at the stagnation point of the blunt-body [51] as a passive technique. Such an aero-spike creates a conical shock wave and a low-pressure region in the stagnation zone which in turn reduces the wave drag. However, certain spike configurations can lead to unsteadiness in the separation bubble and hence an oscillating shock wave. The active drag reduction techniques were proposed to reduce drawbacks of passive techniques so as to have control on the amount of drag force reduced. Among these active methods, counterflow jet [133] and energy deposition are the most prominent. These days energy deposition method is receiving attention of researchers since it has potential to act as an effective flow control technique. Either steady or unsteady energy deposition (Fig 6.1) along the stagnation streamline has been adopted for the reduction of the wave drag force in the supersonic or hypersonic flow through experimental and numerical investigations.

Numerous experimental and computational findings have been performed for the energy deposition in the steady or unsteady form to reduce the wave drag for a blunt-

Kumar S. and Kulkarni V, "An Effective Means of Drag Reduction in High Enthalpy Flow Through Unsteady Energy Deposition", ***Acta Astronautica***, 2021 Sep 1;186:533-43.

Kumar S. and Kulkarni V, "Single and Periodic Energy Pulse Deposition in Reacting Non-equilibrium Supersonic Flows", **Applied Thermal Engineering**, (Under review)

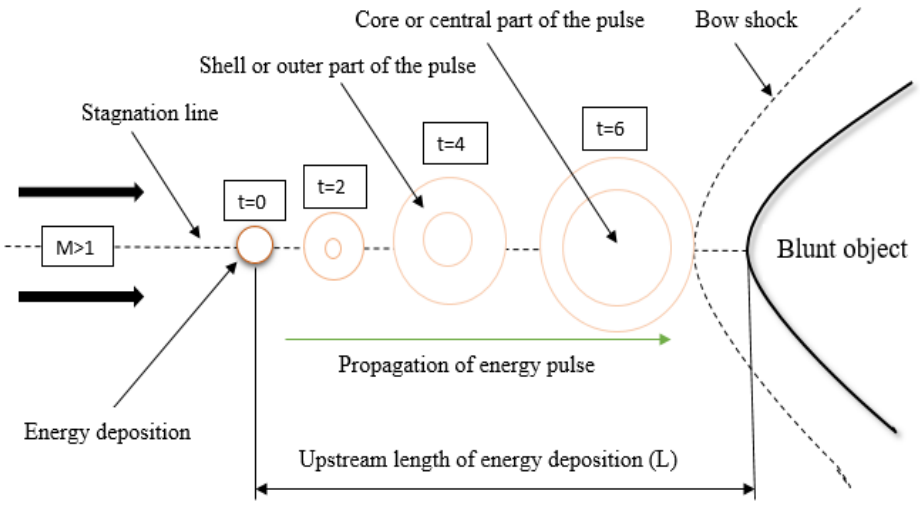

Figure 6.1: Schematics of pulse energy deposition over a blunt object

body in supersonic/hypersonic flows. The major focus of all those explorations was either to understand the mechanism of drag reduction or to quantify the effect of different governing parameters of this technique. Efforts towards optimization are also part of the literature. It is worth to note here that, the steady and unsteady depositions are explored separately and hence it is essential to compare their performance. Further, the effect of stagnation enthalpy on the steady energy deposition is available in the open literature but this effect is unexplored for pulsed energy deposition. Such investigations would not only be beneficial in estimating the time-averaged drag reduction but also to understand the basics of interaction between shock wave and blast waves of different strengths. Moreover, in an extension, it is also possible to comment about the strength of vortex formed with each pulse and the associated amount of drag reduction. Besides, current studies are distinctive since these are planned with non-equilibrium flow solvers so as to understand the real gas effects in comparison with perfect gas assumption estimates. Details of the results obtained and associated analysis are discussed in the following sections.

6.2 Geometry and solver validation

The geometry for present investigations is a hemisphere of diameter (D) 25.4 mm. Only quarter sphere is considered for computations to reduce the computational cost by accounting symmetry boundary condition. Freestream conditions adopted here are the supersonic flow of Mach 3.45, pressure 1.4 MPa and temperature of 85.79 K. The present test model and the freestream conditions are same as those mentioned by Zheltovodov et al. [91] and Adelgren et al. [89]. This supersonic inflow boundary

condition is applied at the inlet of the flow domain. Further, free-slip wall boundary

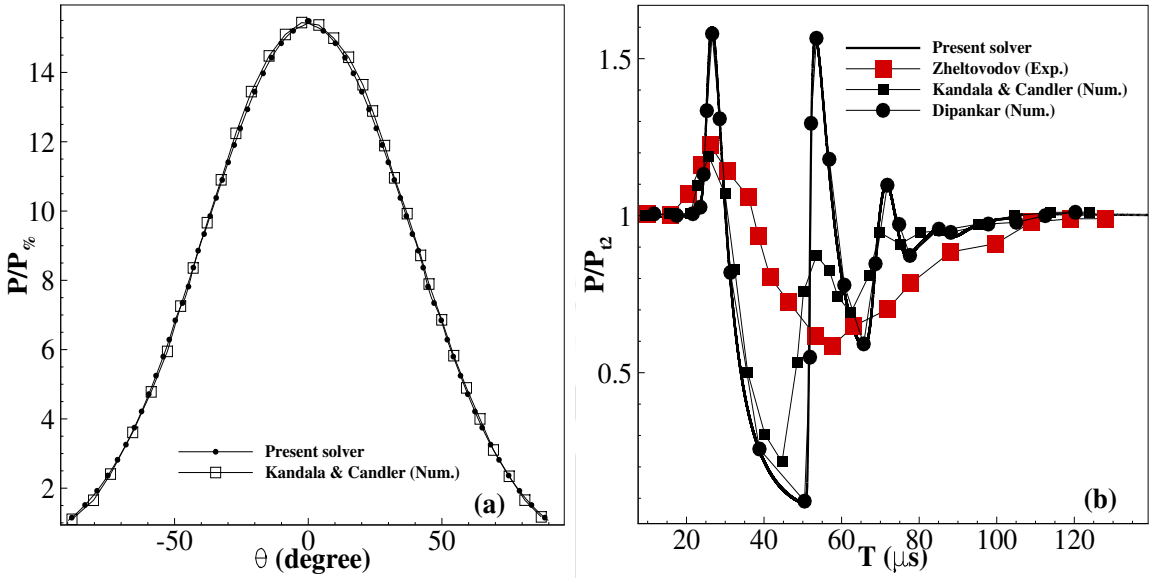

Figure 6.2: Validation of present RGS with experimental and numerical results for [Left] (a) Without energy deposition and [Right] (b) With energy deposition.

condition is implemented on the sphere surface. Initially steady bow shock based surface pressure is comapred with the corresponding reacting numerical results of Kandala & Candler [92] as presnted in Fig 6.2 (a). It is noticed that the pressure profile is in good agreement with the outcome of present reacting gas solver. Further, an energy pulse of 283 mJ is deposited at an upstream location (L) of 1.0D for the time period of 10 ns (Zheltovodov et al. [91]). Stagnation pressure computed from the present non-equilibrium solver is compared with the corresponding experimental result of Adelgren et al. [89] and the numerical results of Dipanker et al. [74] and Kandala and Candlar [93], for same test case as presented in Fig 6.2 (b). At the time of interaction of blast wave with the bow shock, a peak in the stagnation pressure has been noticed. Further decrement in pressure is due to the lensing effects, but beyond this, it again increases due to the reflected blast wave. Same trend is observed in the reported experimental and numerical findings also. Currently predicted magnitude and trend are in good agreement with the literature reported numerical results of Dipanker et al. [74] and Kandala and Candlar [93]. The lower peak pressure estimates, obtained during experiments, would mainly be due to the viscous effects.

6.3 Results and discussion

6.3.1 Flowfield with pulsed energy deposition

(A) Comparison of perfect and real gas considerations

Simulations for pulsed energy deposition are performed using perfect gas solver (PGS) and real gas solver (RGS) to understand the alterations. In these simulations, energy pulse of 283 mJ is deposited at a location of 0.5D upstream of a hemisphere of diameter (D) 25.4 mm, along the stagnation streamline. Freestream of Mach number 3.45 and total temperature of 291 K are considered for the simulations. This deposition produces a spherical blast wave which then travels towards the standing forebody shock ahead of the hemisphere. Travelling time (t_0) of the blast wave can be non-

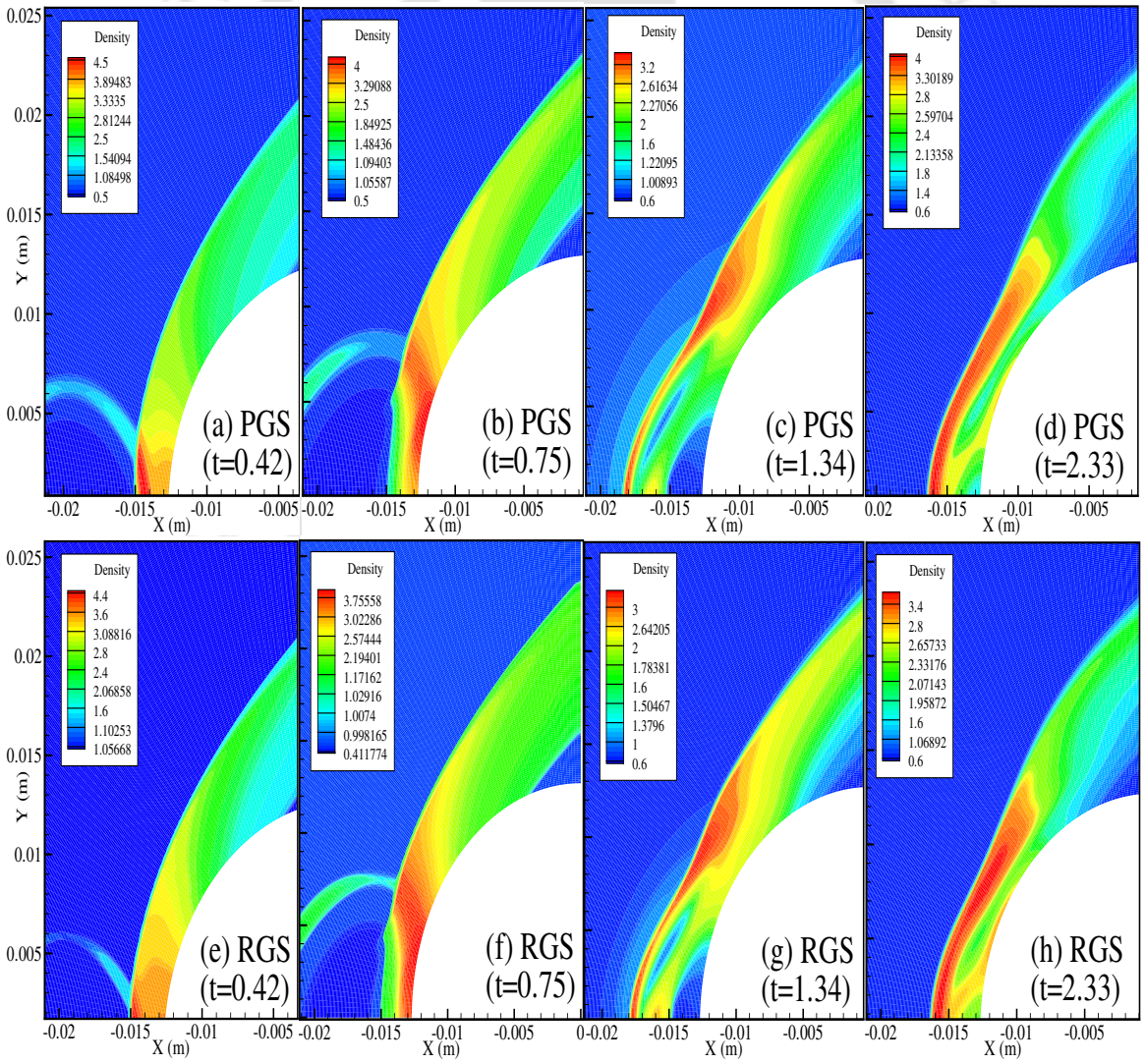

Figure 6.3: Comparision of density contour at various time

dimensionalized by the reference quantities like freestream velocity (U_∞) and base radius (R) of the object to evaluate the dimensionless time (t) as $t_0 U_\infty / R$. The blast front is seen to reach near the standing bow shock at the non-dimensional time of 0.42 as noted from the density contours given in Fig. 6.3 - (a). The blast wave gets compressed upon interaction with the forebody shock (t=0.75). This interaction allows high density gas to flow over the surface from the stagnation location (Fig. 6.3 - (b)). As a result of this, stagnation pressure increases which is evident from the temporal variation of stagnation pressure shown in Fig. 6.4. Higher pressure on the wall confirms the presence of pressurised fluid near the surface of the object (Fig. 6.5). It can also

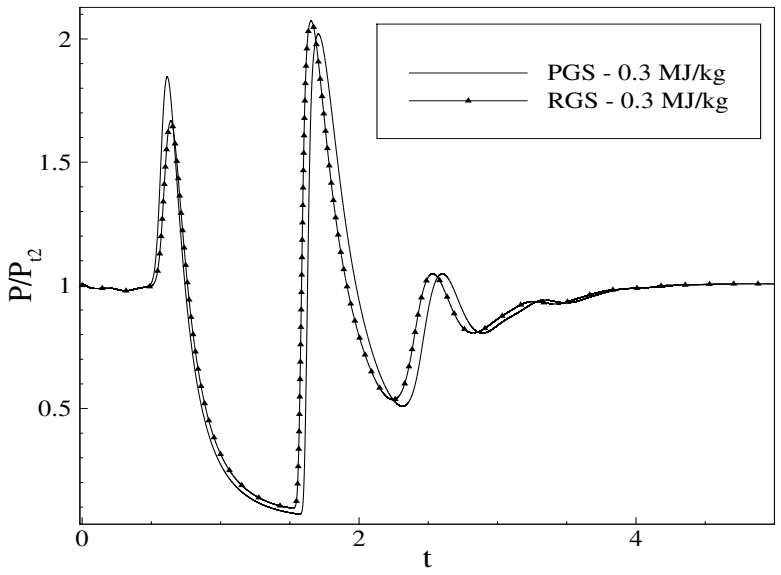

Figure 6.4: Stagnation pressure for the various time

be seen that the estimate of stagnation pressure using the PGS is higher than the one obtained from RGS at the dimensionless time of 0.75. Density contour also predicts the same behaviour for PGS (Fig. 6.3 - (b)) and RGS (Fig. 6.3 - (f)). It can be noted that the freestream for the present simulation is reletively colder ($T_{0\infty} = 291$ K) but still the dominance of real gas effect is very much evident. Since the addition of energy leads to higher temperature in the flow field, it negates the perfect gas assumption of the PGS. At such higher temperature, specific heats (C_p and C_v) experience change in the downstream direction. Further propagation of the blast wave advects the low-density core of the pulse in the shock layer (Fig. 6.3 - (c) and (g)). At the non-dimensional time of 1.34, fluid of higher density is seen to be moved downstream and low-density fluid surrounds the stagnation part. Apart from this, a low-density region or a ring is observed around the high-pressure fluid. This ring is responsible for the first trough in the stagnation pressure signal seen in Fig. 6.4 and 6.5. But it may be noted that the pressure at any location and specifically at the stagnation point is higher

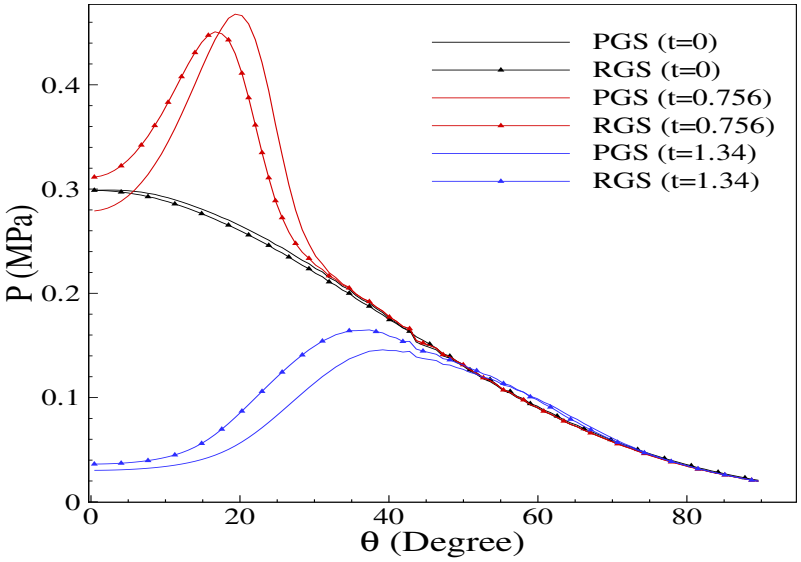

Figure 6.5: Wall pressure at the time of maximum and minimum drag signal

for the RGS at the time instance of 1.34. As time advances, the low-density ring advets downstream. Then at an instance of 2.33, high-pressure and high-density fluid (Fig. 6.3 - (d) and (h)) is seen to cover the entire shear layer. Such interaction of high and low-pressure fluid with the object induces oscillations in the stagnation pressure (Fig. 6.4). Steady-state is achieved upon dying out all the pulses.

The time history of the drag force, incurred by the blunt body, is shown in Fig. 6.6. It can be observed here that the drag signal attains its first peak when the high density region surrounds the surface (t=0.75). But, there is no vortex formation at this time instant. Further, first valley in the drag signal is noted when lower density core surrounds the stagnation region. Also, formation of the low-density vortex near the stagnation part (t=1.34), as seen from the Fig. 6.3, is accounted for the first valley in the drag signal. After this instance, the vortex gets advected downstream along the surface. Such changes in the flow field form several smaller peaks and valleys in the wave drag signal (Fig. 6.6). Moreover motion of the vortex ensures presence of low pressure and low density gas near the wall which remains the criterion for unsteady wave drag reduction. A parameter named "Reduced propulsion energy (E_R)" is introduced for better understanding [94]. This parameter is evaluated using time integration of instantaneous drag reduction as given in the expression below:

$$E_R = U_\infty \int_0^{t_0} (F_{d0} - F_d(t_0))dt_0 \tag{6.1}$$

Here, F_{d0} and $F_d(t_0)$ represent steady and instantaneous drag forces respectively. Time variation of this new parameter is plotted in Fig. 6.7. It can be observed here that

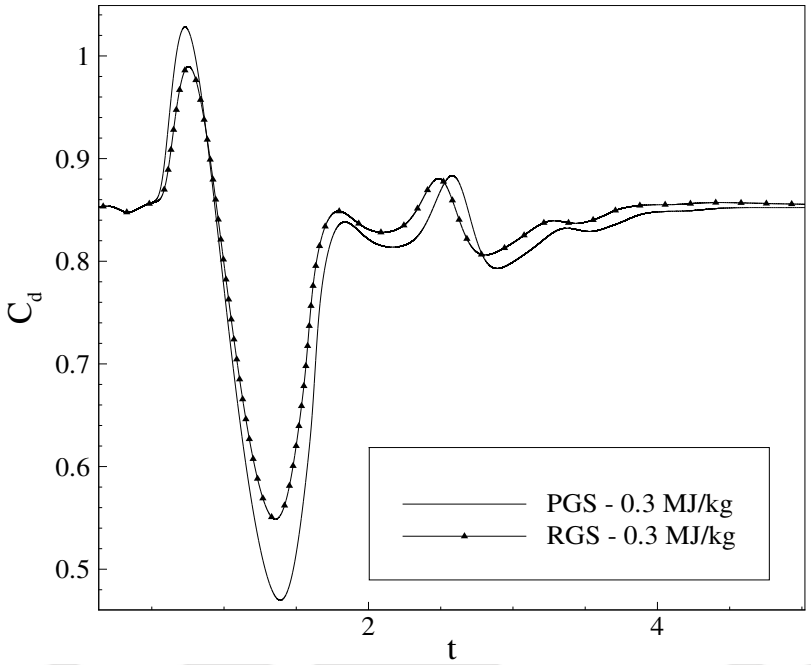

Figure 6.6: Instantenious wave drag signal with travelling of blast wave

the negative propulsion energy is present until the formation of vortex at the stagnation part. Then onward, formation of low density vortex (Fig. 6.3) ensures wave drag reduction. Therefore, a major part of the positive propulsion energy is seen after this instance (Fig. 6.7). Further, PGS predicts more negative propulsion energy than the RGS. On the other hand, after generation of the vortex, PGS shows more drag reduction during the advection of this vortex (Fig. 6.6) and thus shows higher propulsion energy (Fig. 6.7) as compared to RGS. This indicates that the size and strength of the vortex govern the drag reduction.

(B) Effect of freestream enthalpy

Investigations are extended to understand the high enthalpy effect on drag reduction by pulsed energy deposition. Various freestream conditions are considered for this objective. These conditions include freestream total temperatures (T_0) as, 295 K, 992 K, 1989.5 K and 2984 K with corresponding stagnation enthalpies (H_0) as 0.3 MJ/kg, 1.0 MJ/kg, 2.0 MJ/kg, 3.0 MJ/kg respectively. The simulations for this objective are carried out with same hemisphere as considered earlier. An energy pulse is created by depositing 283 mJ energy at a location 0.5D upstream of the sphere. High freestream static temperature along with the presence of blast wave leads to various chemical reactions. As a result of this, different species like O, N and NO can be observed in the flow field. It has been noted that the low-density vortex, formed by the blast wave during its interaction with the bow shock wave, plays a dominant role in the reduction

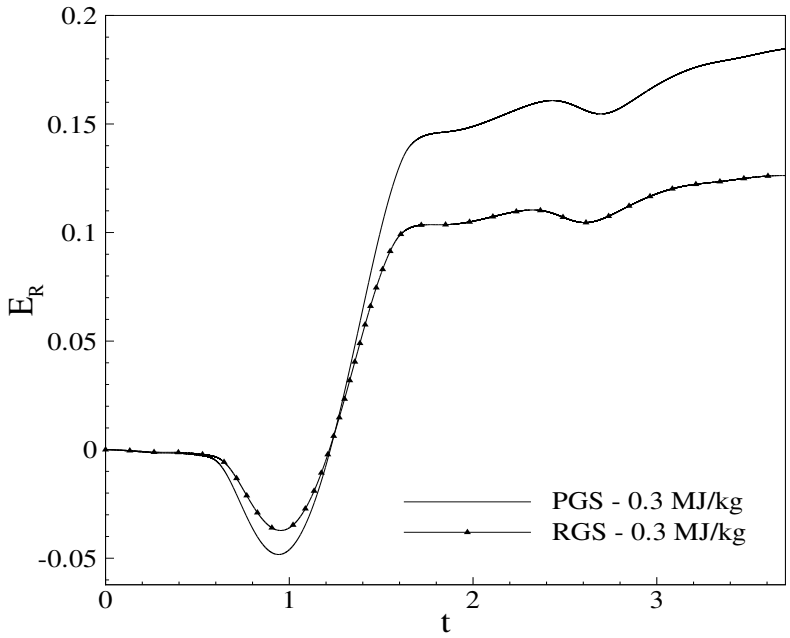

Figure 6.7: Time history of reduced energy of blast wave

of drag force. For a given freestream, the strength of this vortex mainly depends on the properties and strength of the blast wave. Figure 6.8 shows the pressure distribution just before the interaction of the blast wave with the standing bow shock for all the cases. It can be noted that the outer region of the blast wave or shell, along with its core or central part, experiences higher pressure for the higher freestream enthalpy conditions. The magnitude of pressure in the outer shell of deposited pulse increases from around 48.10 kPa to 122.50 kPa when the freestream stagnation enthalpy changes from 0.3 MJ/kg (Fig. 6.8 - (a)) to 3.0 MJ/kg (Fig. 6.8 - (d)). Further, the central or core part along with the outer or shell part of the blast wave experiences lower density at higher inflow stagnation enthalpy conditions as shown in the Fig. 6.9. Here, magnitude of the density of the pulse core for lower enthalpy condition (0.3 MJ/kg) is around 0.2 kg/m^3 while for highest enthalpy (3.0 MJ/kg), is around 0.02 kg/m^3. It can be noted that there is 90% decrement in the magnitude of the core density. Such changes in the pressure and density of the deposited pulse are due to the continual dissociation and Zel'dovich reactions for high enthalpy flow. These reactions produce the new species (N, O and NO) in the flow field. Here, distribution of the mass fraction of oxygen (Y_O), along the stagnation streamline, just upto the interaction with the bow shock, is shown in Fig. 6.10. The most and the least amount of dissociated species are present at the outer shell and the inner core respectively. Further, the diameter of the deposited pulse (D_b) changes from 9.8 mm to 12.0 mm from the lowest to the highest freestream stagnation enthalpy condition. This increment in diameter by 19.48% can also be confirmed from the plateau distribution of Y_O (Fig. 6.10). Such

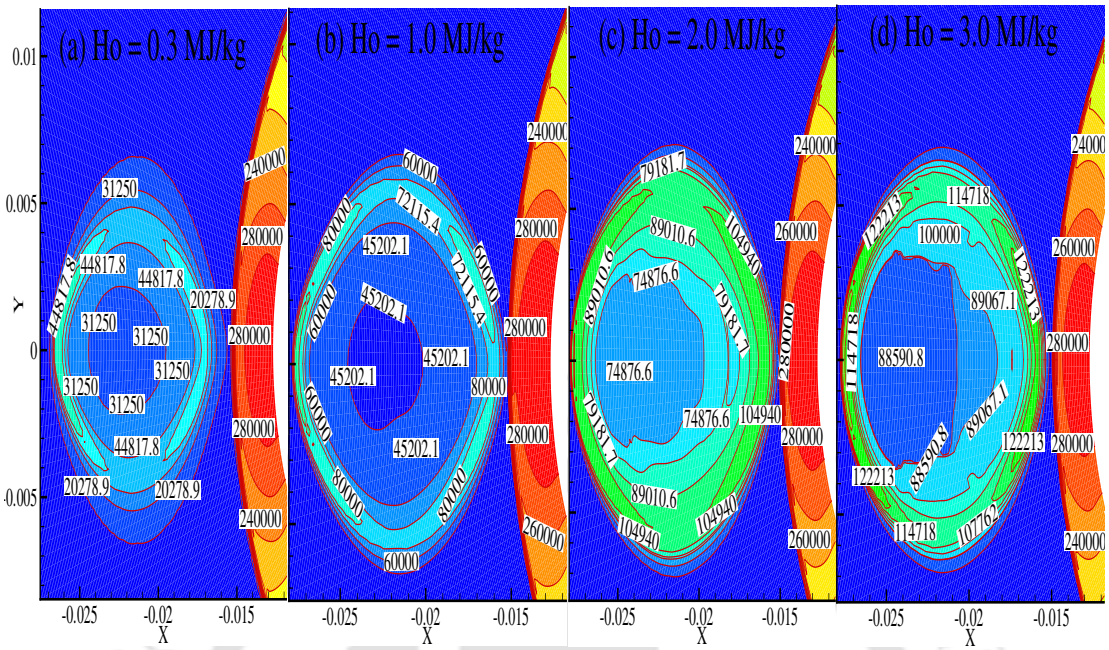

Figure 6.8: Pressure contour of the pulse before interaction with the bow shock

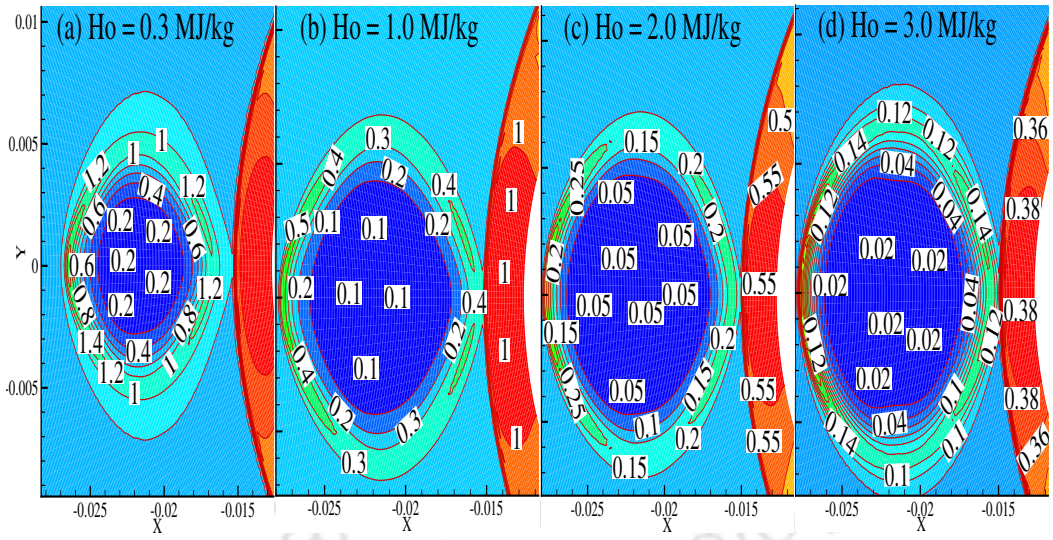

Figure 6.9: Density contour of the pulse before interaction with the bow shock

alterations in the pulse property would also alter its interaction with the bow shock Temporal variation of the stagnation pressure and wall pressure distribution, for the initial interaction time (t=0.75), are shown in Fig. 6.11 and Fig. 6.12 - (2) respectively. Pressure due to shock reflection increases with higher inflow stagnation enthalpy. High pressure outer shell and the core region of the pulse ensure strong interaction and are responsible for high pressure gas near the wall surface. This leads to higher stagnation (Fig. 6.11) and wall pressures (Fig. 6.12 - (2)). Such alteration in the field and wall pressure led to higher wave drag for the object (Fig. 6.13). With the advancement in

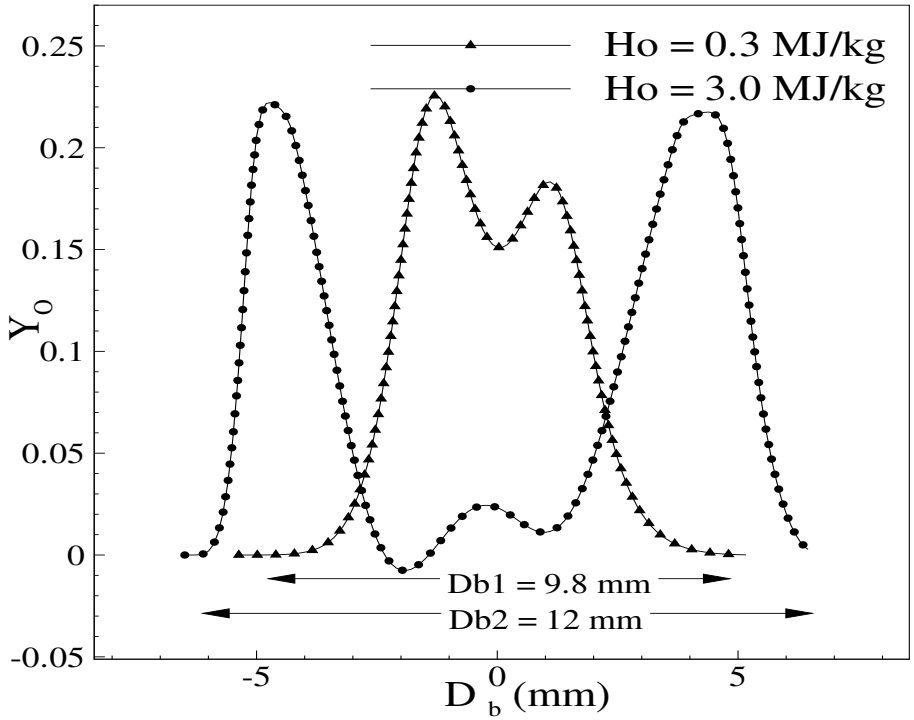

Figure 6.10: Variation of Y_O across the diametral stagnation line of blast wave

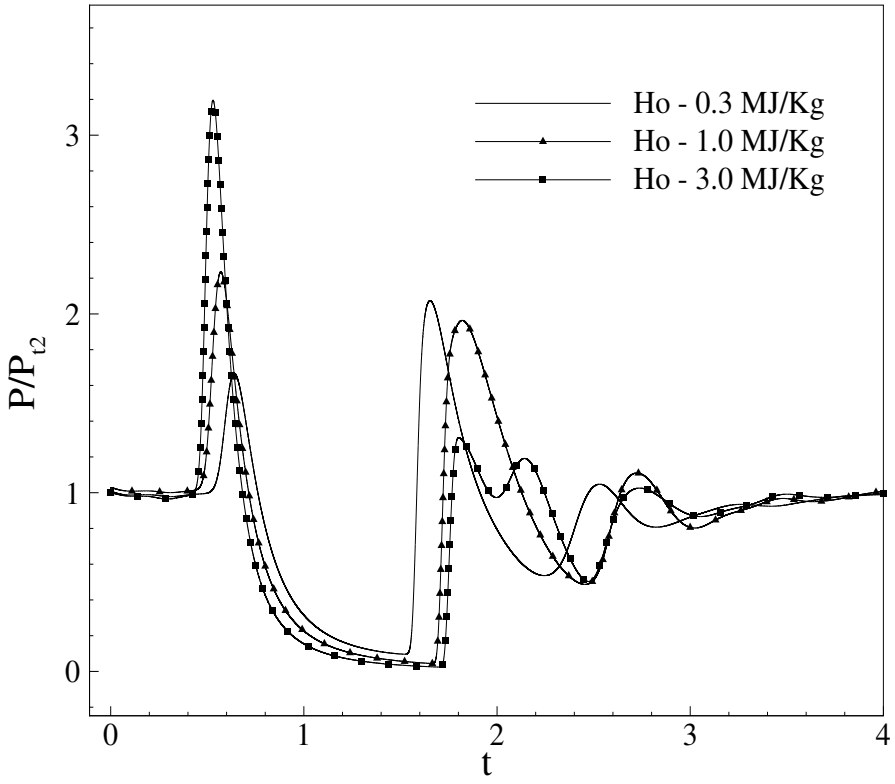

Figure 6.11: Time variation of stagnation pressure for different freestream enthalpy

time (t=1.34), core of the pulse reaches near the stagnation part of the body. This

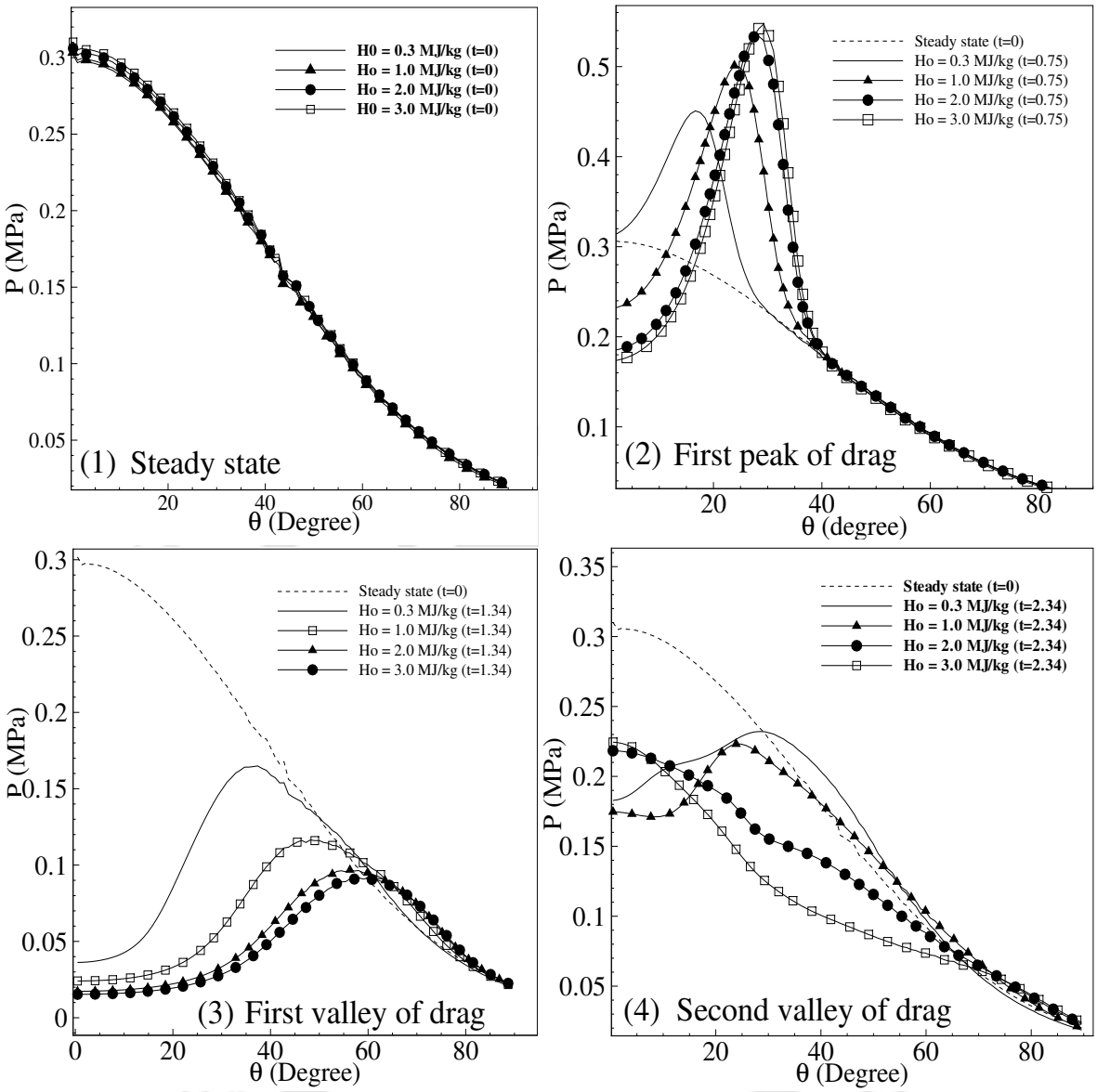

Figure 6.12: Alteration of wall pressure at various time instances

interaction consistently lowers the stagnation pressure (Fig. 6.11) and surface pressure with the enthalpy (Fig. 6.12 - (3)). This change is mainly due to lower density and low pressure at the core of the blast wave (Fig. 6.9) with the higher stagnation enthalpy cases. Since low-density core led to the formation of stronger vortex in the flow field, it is eventually responsible for the reduction in stagnation and wall pressures. Therefore lower drag is experienced by the object, for this time instance (t=1.34), which is evident from the deeper valley of in the drag signal for higher enthalpy cases (Fig. 6.13). Then this vortex moves over the object surface and introduces fluctuations in the drag signal.

One of the silent features of the present study is to understand the second valley in the drag signal experienced by the object. This valley can be seen in the Fig. 6.13.

Here, lower enthalpy simulations show only one valley at the time instance of 1.34. But high enthalpy conditions generate one more valley at the later time instance of 2.34. This is mainly because of the increment in the pulse size and lower density at the core of blast wave in case of higher enthalpy of 3.0 MJ/kg. These changes lead to

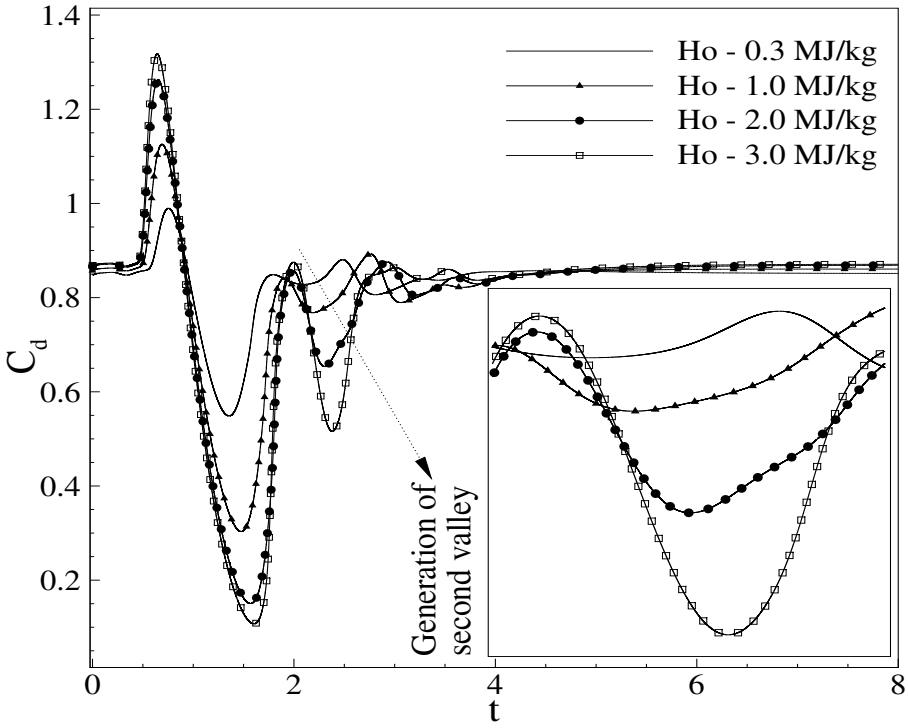

Figure 6.13: Time history of impulse drag signal for pulse deposition at L = 0.5D

the formation of stronger low-density vortex during the interaction of blast wave with the bow shock. Advection of such stronger vortex, along the surface of object, ensures lower surface pressure (Fig. 6.12 - (4)) at higher stagnation enthalpy as compared to 0.3 MJ/kg stagnation entahlpy case. Same phenomenon has also been noticed if the energy is deposited further upstream location (L) of 1.0D, as shown in Fig. 6.14. This is the reason for the first and second vallies in the drag signal (Fig. 6.14) for both cases of upstream locations (L=0.5D and 1.0D).

(C) Instanteneous and integrated analysis

The interaction characteristics of the blast wave can be represented by the instantaneous drag force (F_{dt}) which is calculated by the expression $F_{dt} = \int_S (P(t) - P_\infty) dA$. Here, P(t) is instantaneous pressure on the surface and s is surface are. Further, a dimensionless time ($t^* = U_\infty t/R$) is also simultaneously calculated to compare the drag force and reduced energy for different freestream stagnation enthalpy conditions.

At first, a single pulse is deposited at an upstream location of 0.5D for which the instanteneous drag force is shown in Fig. 6.15. The initial interaction of blast with

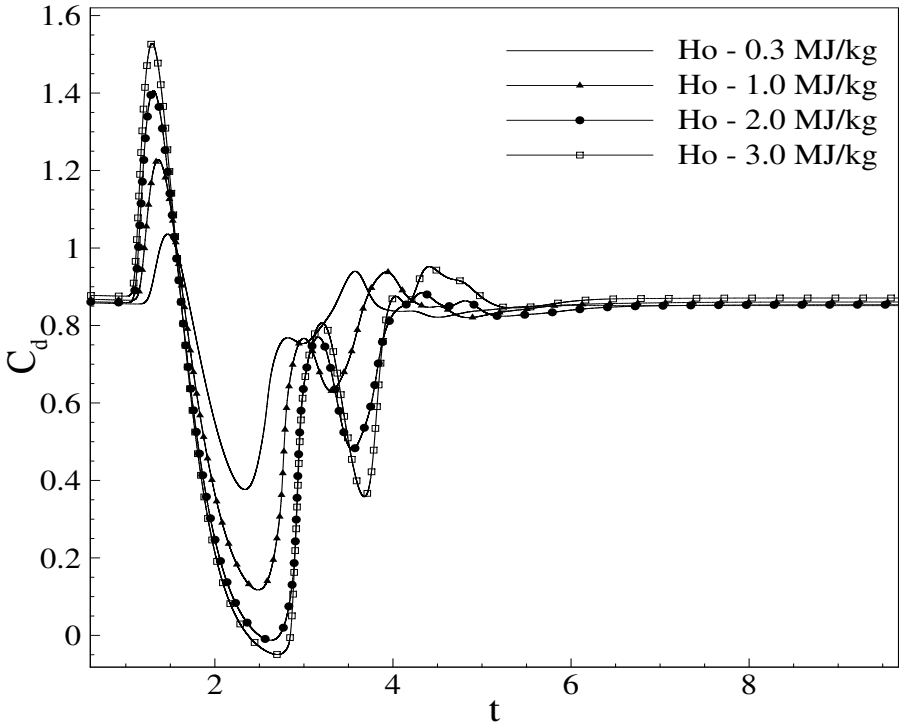

Figure 6.14: Time history of impulse drag signal for pulse deposition at L = 1.0D

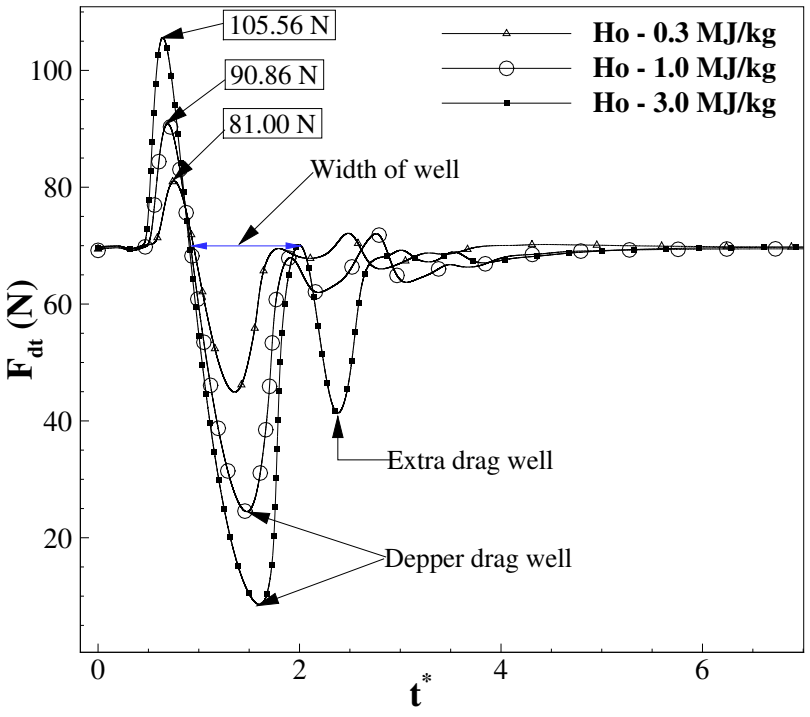

Figure 6.15: Drag force variation with dimensionless time for different enthalpy at an upstream location of 0.5D

standing bow shock produces higher drag force. Further, the formation of low-density vortex in the flow field is responsible for the first well in the drag plot (Fig. 6.15).

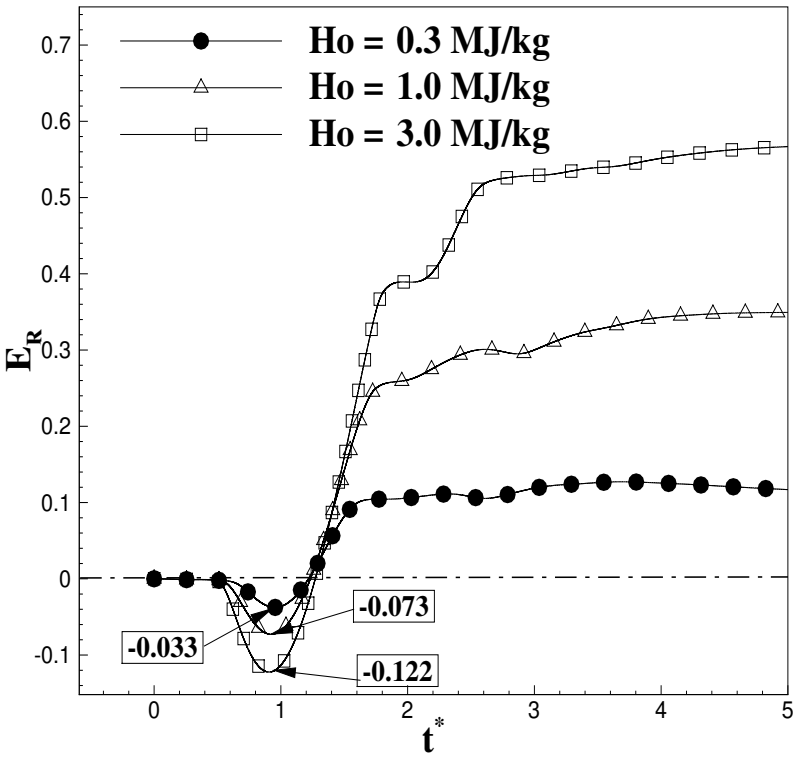

Figure 6.16: Changes in reduced energy of the blast wave for different enthalpy at L=0.5D

Advection of this vortex over the object produces fluctuations in the drag signal and it attains a steady-state after time passes. The magnitude of the peak drag, at the time of shock transmission on the surface (Fig. 6.15), is found to be increasing with inlet enthalpies. This magnitude is 81 N and 105 N for the lowest (0.3 MJ/kg) and highest enthalpy (3.0 MJ/kg) cases respectively. As the pressure of the blast wave increases (Fig. 6.8) with the enthalpy, they are responsible for the consistently higher drag during shock reflection. However, the drag force, at the time of vortex interactions, decreases and forms a well like structure for all the FSE. Figure. 6.15 reflects a stronger vortex for decreased density (Fig. 6.9) of blast along with it's increased size. Further, the increased width of this drag well also represents larger duration of the drag reduction, at the time of vortex interactions, for higher freestream conditions. Furthermore, such a strong vortex generates an extra drag well at elevated enthalpy of 3.0 MJ/kg (Fig. 6.15). The term "Reduced energy or Propulsion energy E_R" is also calculated to show the energy consumed or used for the instantaneous drag reduction. This can be calculated by the expression $E_R = U_\infty \int_0^t (F_{d0} - F_d(t))dt$ where, F_{d0} is the steady-state drag. The higher drag force, due to the shock reflection, demands negative propulsion energy as shown in Fig. 6.16. This negative energy is increased by 73% for the higher freestream enthalpy as compared to lower one. Such increment di-

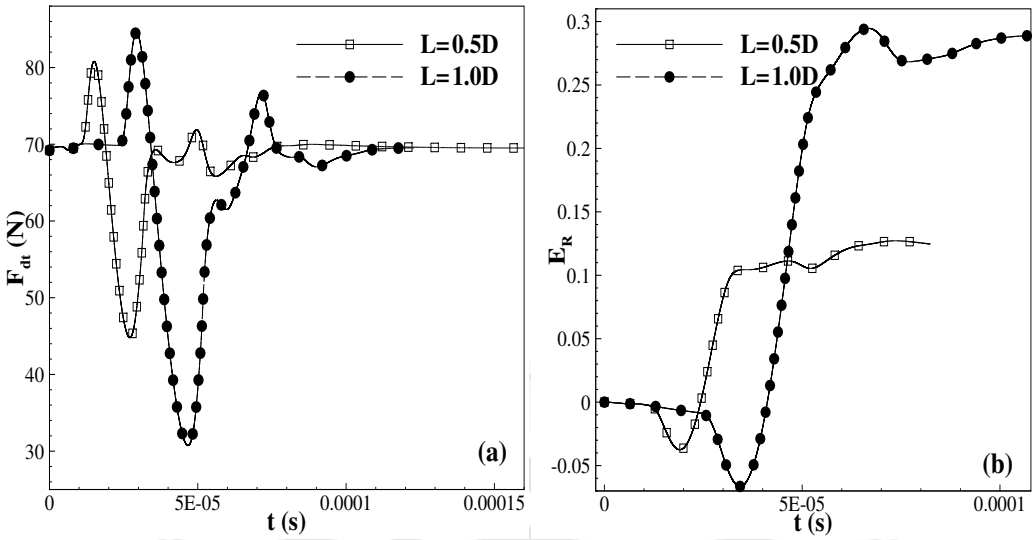

Figure 6.17: Drag force variation with time for upstream length of 0.5D and 1.0D at given FSE of 0.3 MJ/kg

rectly reflects the increased drag on the surface with FSE. Moreover, positive reduced energy represents the decreased drag force on the blunt object. It can be seen that higher positive energy is obtained for increased enthalpy which reflects larger drag reduction. Studies are also carried out at higher length of energy deposition location, L=1.0D. The same freestream enthalpies and energy deposition conditions are used for L=1.0D. The comparison between drag force signal and propulsion energy for up-

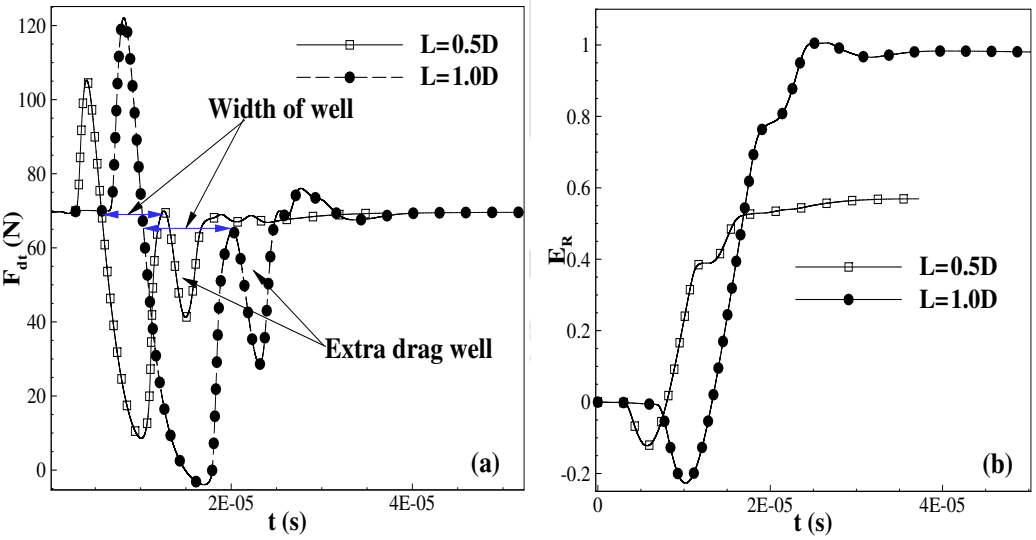

Figure 6.18: Drag force variation with time for upstream length of 0.5D and 1.0D at given FSE of 3.0 MJ/kg

stream deposition location of 0.5D and 1.0D at FSE of 0.3 and 3.0 MJ/kg are shown in Fig. 6.17 and Fig. 6.18 respectively. Higher upstream location produces higher wave drag (Fig. 6.17(a) and Fig. 6.18(a)), at the time of shock reflection, and thus increased

negative reduced energy (Fig. 6.17(b) and Fig. 6.18(b)) is predicted at lower as well as higher enthalpy cases. Further the higher upstream length produces a stronger vortex which imposes lesser drag force at the time of vortex interactions. This decrement can also be seen from the higher magnitude of positive reduced energy for any enthalpy cases. Moresover, the width of the first drag well also increases at higher deposition locations. The drag plots, for higher enthalpy case, show that the formation of the second drag valley is consistent with any upstream deposition location (Fig. 6.18 (a)). Thus increase in the freestream stagnation enthalpy or increase in the upstream deposition location produces simiar effects for the pulsed energy deposition.

(D) Alteration of power effectivness

Investigations are further extended for the calculation of performance of deposited energy for higher enthalpy flow cases. Since there are fluctuatons in drag signal, it is hard to support any specific freestream enthalpy for better drag force reduction. For this, power effectiveness or energy efficiency [94] is introduced to calculate the performance of the unsteady energy deposition. It can be calculated as E_R/Q where E_R

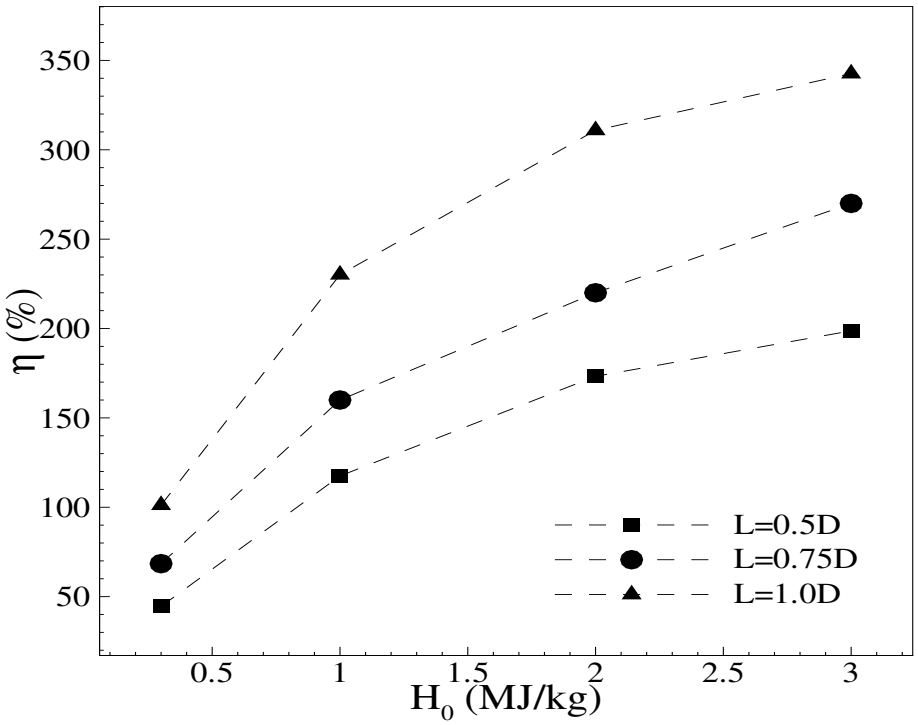

Figure 6.19: Power effectiveness for different freestream stagnation enthaply conditions

is evaluated by the Eq(6.1) and Q is the deposited energy. This efficiency is evaluated for all freestream stagnation enthalpy conditions. Various upstream lengths (L=0.5D, 0.75D and 1.0D), for a given amount of energy strength (283 mJ), are considered for calculation of the power effectiveness (Fig. 6.19). It can be noted that the effectiveness

for the lowest enthalpy and highest enthalpy case are 41% and 170% respectively for the upstream deposition location of 0.5D. This alteration is due to the larger size of the energy pulse along with the lower density pulse core formed at higher freestream enthalpy conditions. On the other hand presence of the second valley in the drag signal, for enthalpy of 3.0 MJ/Kg, increases the magnitude of reduced energy (E_R) and thus improves the power effectiveness. It can be noted that there is 130% increment in the power effectiveness for the higher enthalpy case. Similar magnitude and trend are obtained for further upstream depositions (L=0.75D and 1.0D) as shown in Fig. 6.19. Various amounts of energy depositions (Q=150 mJ, 283 mJ and 400 mJ),

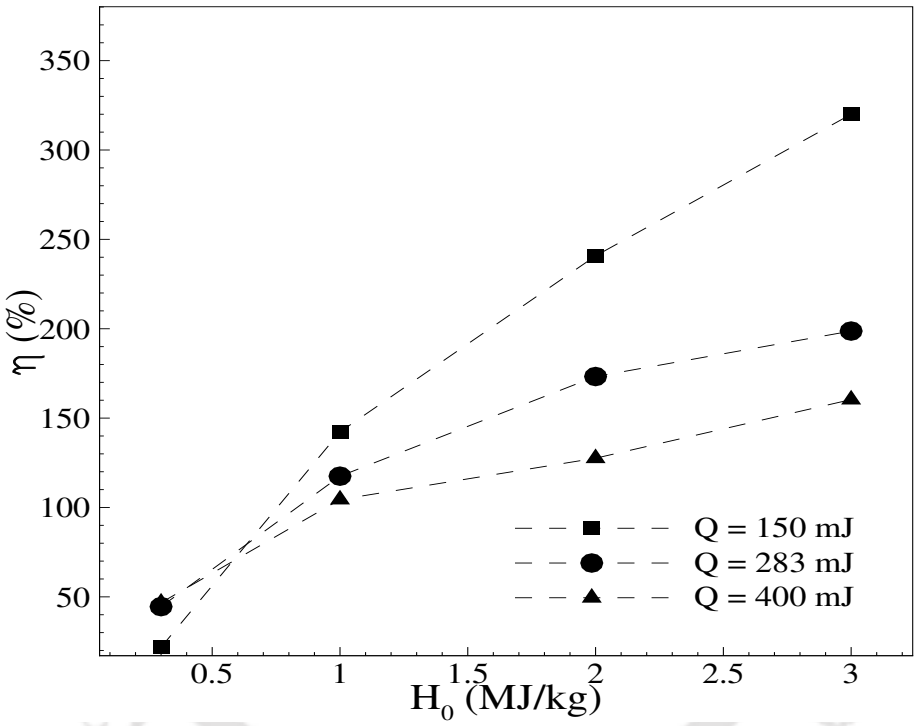

Figure 6.20: Power effectiveness for different strength of energy pulse

for a fixed upstream location of 0.5D, have also been taken for calculations of the power effectiveness. Their variation with different higher freestream enthalpy has been shown in Fig. 6.20. It can be noted that the power effectiveness increases with the inlet stagnation enthalpy for any amount of energy deposited. On the other hand, it decreases for higher strength of energy at a given freestream stagnation enthalpy. The power effectiveness for 150 mJ, 283 mJ and 400 mJ energy depositions are 370%, 170%, and 130% respectively for the stagnation enthalpy case of 3.0 MJ/Kg. There is decrement of 240% in power effectiveness for the higher strength of energy deposition (400 mJ) as compared to the lower one (150 mJ). Though the higher amount of energy increases the reduced energy (E_R), at the same time energy strength (Q) also increases. Thus the power effectiveness (E_R/Q) decreases due to the dominance of

energy strength. The trend of the results is also consistent for the other strengths of the energy deposition.

6.3.2 Flow field with the steady energy deposition

Studies are further extended for the high enthalpy effect on surface pressure and wave drag for the steady energy deposition (SED). The geometry of the object and freestream parameters are kept same as mentioned earlier for the unsteady energy deposition (UED) case. But the amount of deposited energy is taken as 400 W for the SED case. This strength of energy is deposited at an upstream location (L) of 0.5D. Simulations are performed for various freestream stagnation enthalpy conditions. The energy deposition in steady case, SED, replaces the bow shock into the oblique shocks and creates a conical dead air region near the stagnation zone for the lowest freestream

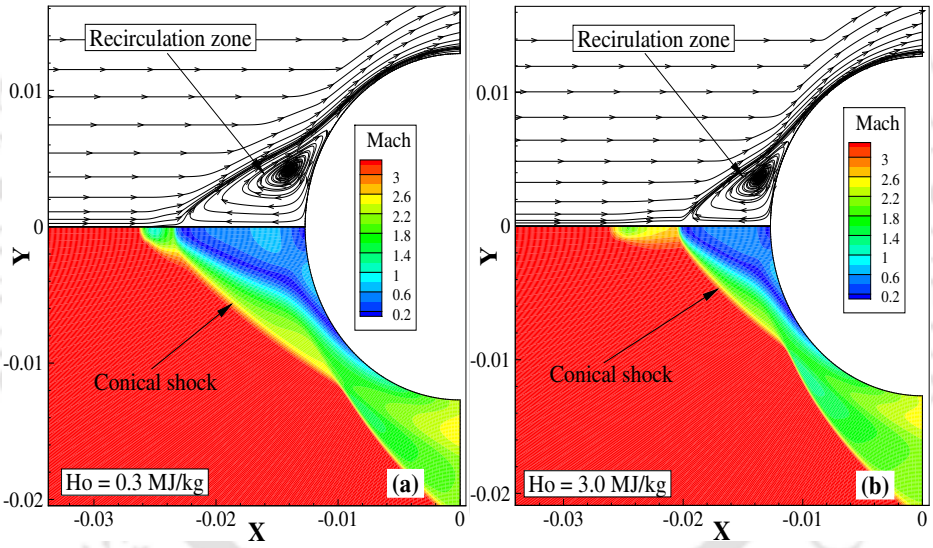

Figure 6.21: Changes in the flowfield at higher enthalpy at same freestream conditions

enthalpy case (0.3 MJ/kg) as presented in Fig 6.21 (a). Due to this, the object experiences lesser pressure and thus lower drag as compared to no deposition case. This oblique shock shifts in the downstream direction for the higher freestream enthalpy case (3.0 MJ/kg) as shown in Fig 6.21 (b). Since this shock governs the extent of the conical dead air region around the stagnation zone, smaller sized dead air region is noticed at higher enthlpy case as compared to lower one (Fig 6.21). The decrease in size of the conical region increases the surface pressure for the higher enthalpy case as shown in Fig. 6.22. Here the peak pressure on the object shows the sign of shock impingement. These results are consistent with the reported literature (Siddesh et. al. [73] and Dipanker et al. [74]) for the SED case. Further, the Power effectiveness for the steady deposition is calculated as $(F_{d0} - F_d)U_\infty/Q$. Here, F_{d0} and F_d are the

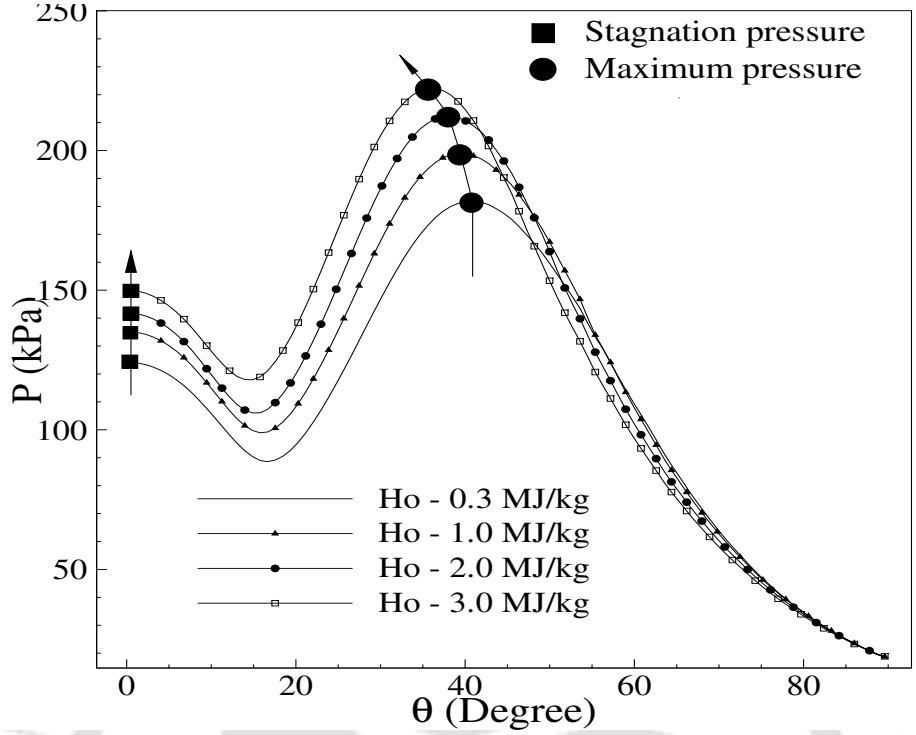

Figure 6.22: Alteration of surface pressure with enthalpy for SED at L = 0.5D

drag forces in the absence and presence of energy deposition respectively. Figure 6.23 shows the variation of power effectiveness and co-efficient of wave drag for the various higher enthalpy situations. It is expected that, calculated drag force should increase

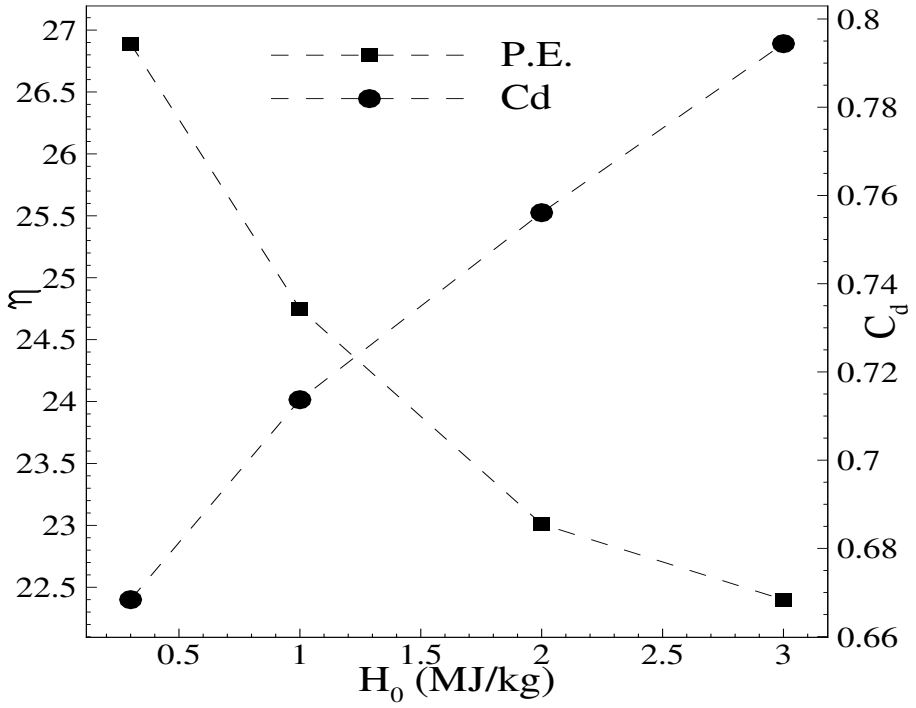

Figure 6.23: Variation of power effectiveness and wave drag for SED

with the enthalpy because of the increase in surface pressure (Fig. 6.22). The dominance of the higher wave drag leads to lower power effectiveness for the higher inlet stagnation enthalpy [73], [74], [134]. Here, it can be seen that the change in power effectiveness for the UED is positive than the SED for the higher enthalpy conditions.

Criteria of the drag reduction for SED is governed by size of the dead air region but for the UED, it is the advection of vortex over the object. Here we see that the size of conical dead air region decreases in case of SED, but the strength of vortex increases in case of UED for the higher freestream stagnation enthalpy case. Hence it is concluded that SED is less efficient for drag reduction at higher stagnation enthalpy. Thus it is recommended to use unsteady energy deposition rather the steady one for higher drag reduction if the stagnation enthalpy of the flow increases.

6.3.3 Periodic pulse energy deposition

The above discussion clearly states that the single energy pulse deposition is marked for increased positive reduced energy at higher enthalpy conditions due to stronger vortex. On the other hand, the drag at the time of shock reflection is consistently higher with increase in the negative reduced energy for higher inlet enthalpies. This

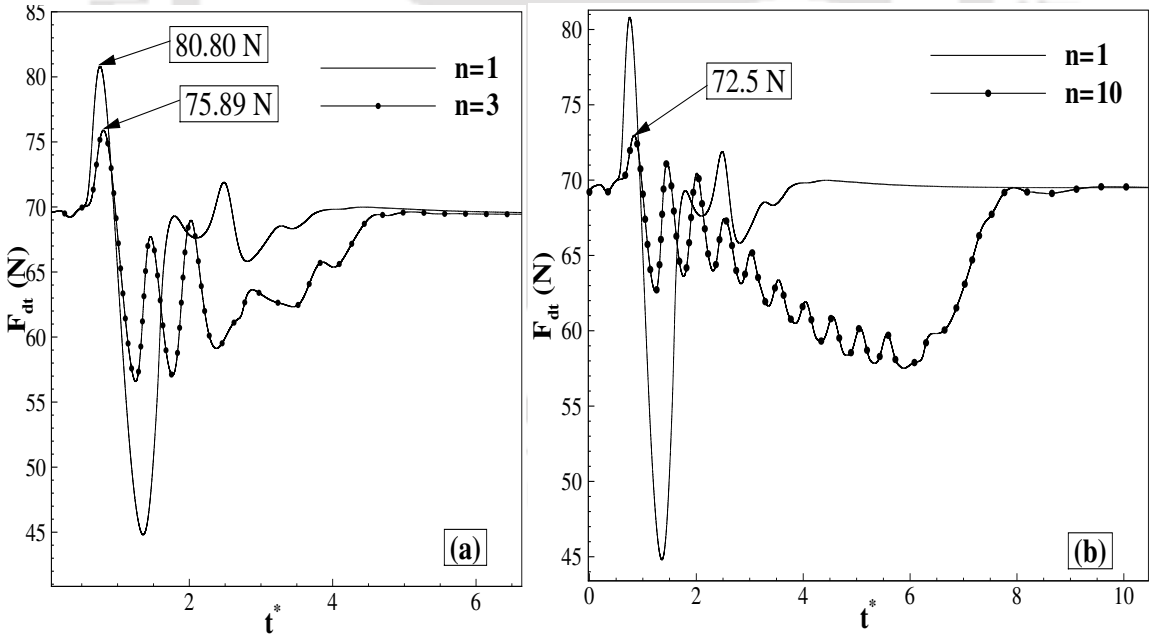

Figure 6.24: Time history of drag force for splitted blast wave at given upstrem length (L=0.5D) and stagnation enthalpy (H_0=0.3 MJ/kg)

increment produces an adverse effect on the optimum performance calculation of the energy efficiency of the blast wave. Further, the decrement in the drag force for single pulse is observed for a very small time interval. Hence, lower shell pressure is essential for possible drag reduction at the time of shock reflection. Moreover, prolonged drag

force reduction can be obtained by the use of repetitive blast waves. In this regard, the number of small energy pulses have been used for periodic deposition instead of the single pulse deposition, for the same freestream conditions and upstream locations. In this case, higher strength of the single blast wave (Q=283 mJ) is equally split into the smaller strength of 'n' pulses for the periodic deposition. As a consequence, three continuous pulses (n=3) of strength (Q_3) 94.33 mJ, six pulses (n=6) of strength (Q_6) 47.16 mJ and ten pulses (n=10) of strength (Q_{10}) 28.3 mJ are selected for deposition at a frequency of 100 kHz. Initial periodic deposition is carried out for the lowest enthalpy case and an upstream location of 0.5D. The estimated time varying drag

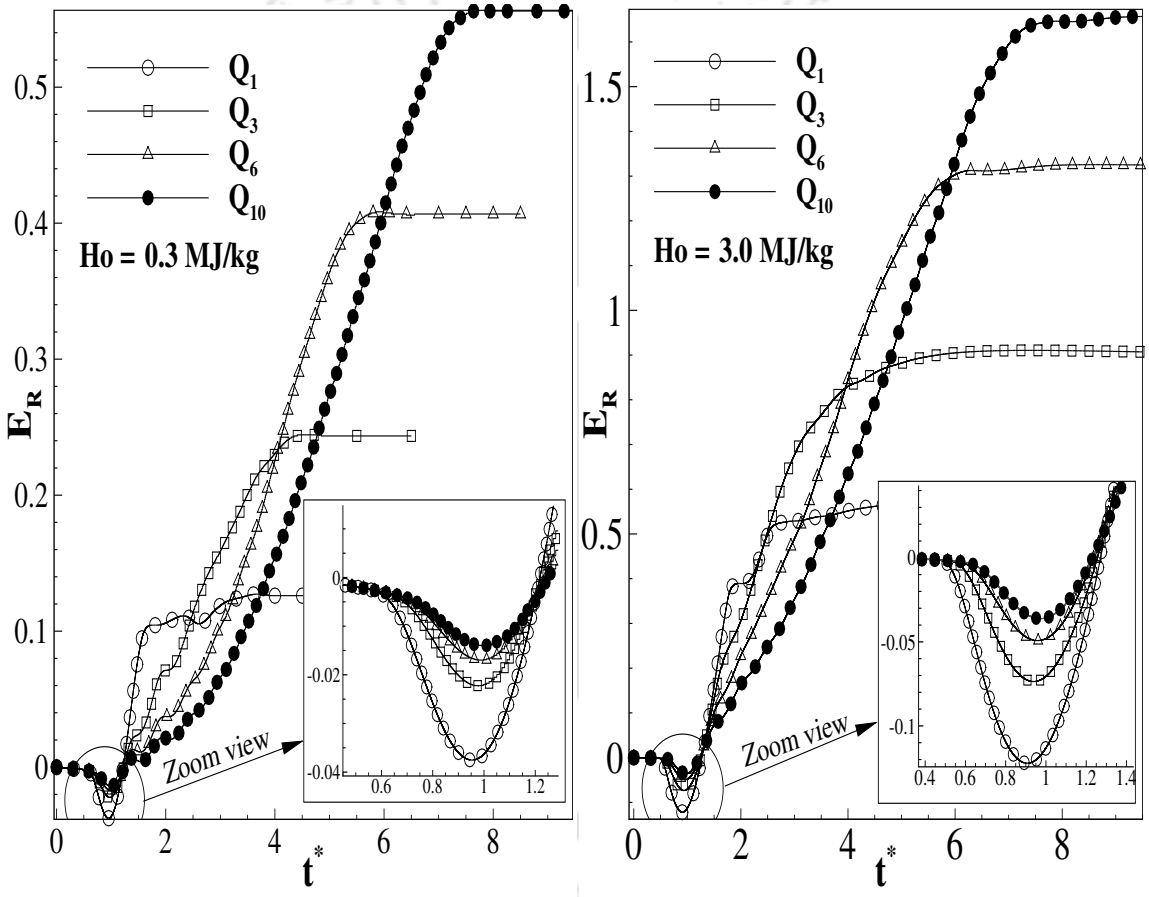

Figure 6.25: Reduced/propulsive energy variation, for all splitted pulse, for lowest ($0.3MJ/kg$) and Highest (3.0 MJ/kg) FSE conditions at L=0.5D

force is comapred for three and ten pulses, with single pulse deposition, are shown in Fig. 6.24 at lower stagnation enthalpy (0.3 MJ/kg). The drag force at the time of shock reflection decreases for three pulses (Fig. 6.24 (a)) and this decrement is enhanced for higher number of pulse depositions (Fig. 6.24 (b)). The peak drag is found also to be 10.27% reduced for ten pulses as compared to single pulse depositions. It can also be seen that, for the initial three pulses, the fluctuation in the drag force are higher due to the flow stabilization [135]. After three pulses, low magnitude fluctuations

in the drag force are observed. The instantaneous drag force reduction is lesser for Q_{10} as compared to Q_3 case. Moreover, the advantage of higher number of pulses (n=10) is that it provides prolonged drag force reduction (Fig. 6.24). Hence, it can be mentioned that the single larger drag well for the lower period should be replaced by several smaller wells for a larger period and better drag reduction using periodic pulse deposition. Further, the drag force dynamics of the split pulse can be seen

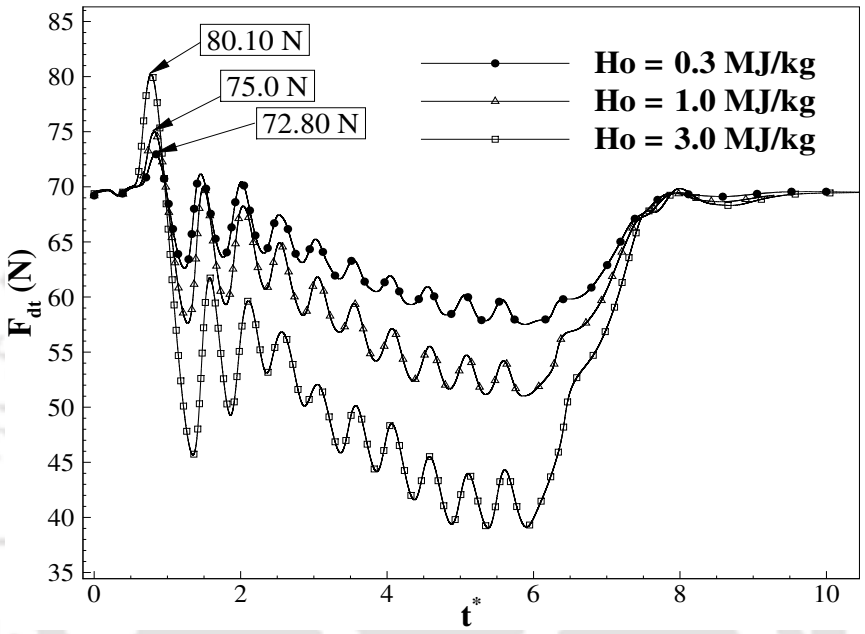

Figure 6.26: Comparision of drag force signal for different enthalpy conditions

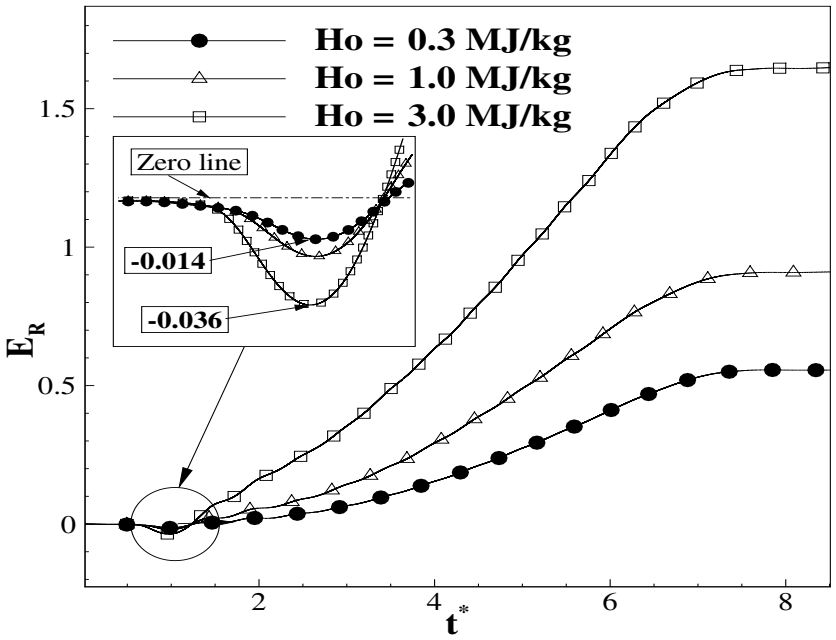

Figure 6.27: Comparision of propulsion energy for different inlet enthalpy conditions

from the reduced energy plots as well which is shown in Fig. 6.25. It can be seen that the magnitude of negative propulsive energy decreases as the peak drag force decreases for higher number of pulses. Further, the magnitude of positive propulsive energy increases due to decrease in negative propulsion energy and increase in period of drag reduction with the number of pulses for lower enthalpy of 0.3 MJ/kg. Similar behavior of propulsion energy is observed for increased pulses at higher freestream enthalpy of 3.0 MJ/kg (Fig. 6.25). The magnitude of negative as well as positive propulsion energy increases, due to altered properties of the blast wave, for higher freestream enthalpy considerations. Higher reduced energy for an increased number of pulses represents better utilization of energy pulse. The comparison of drag force for higher freestream inlet enthalpy, at given number of pulses (Q_{10}) and an upstream location (L=0.5D), is shown in Fig. 6.26. It is obvious that the drag force, at the time of shock reflection, is increased with inlet enthalpy but the magnitude is still lesser as compared to single pulse deposition (Fig. 6.15) for the same freestream conditions. This increment in the drag force agrees well with the increased magnitude of negative propulsion energy with increase in the inflow stagnation enthalpy for same number of pulses as shown in Fig. 6.27. It is noted that periodic pulse deposition (Q_{10}) causes 57.5% and 70.5% decrement in the negative propulsive energy for lower and higher enthalpy cases respectively. Further, the drag force after the vortex formation is found to be lower and it is consistent with every higher enthalpy case. Each peak and valley of drag force signal also increase for higher enthalpy cases. These changes lead to higher positive propulsion energy at elevated enthalpy conditions for same number of pulses.

6.3.4 Energy efficiency of the blast wave

The performance for each energy pulse case has been estimated. For this, efficiency is calculated as the ratio of cumulative propulsive energy to the total strength of blast wave (E_R/Q). The computed efficiency, for single as well as multiple pulses, is shown in Table. 6.1 at different freestream enthalpies and upstream locations. Here, the energy efficiency of the single blast wave (Q_1) increases at higher enthalpy (1.0 MJ/kg and 3.0 MJ/kg) and this increment further enhances for upstream deposition location of 1.0D. This performance parameter is seen to be enhanced for any increased number of pulses, as the magnitude of the positive propulsion energy increases with number of the blast waves, for lower enthalpy and deposition location of 0.5D. The altered properties of pulse at higher enthalpy increase the positive reduced energy as compared to lower enthalpy and thus energy efficiency. These calculations are consistent for any higher stagnation enthalpy, number of pulses and upstream deposition locations (Table. 6.1).

Table 6.1: Gas dynamic energy efficiency for given laser strength of 283 mJ

Conditions	L=0.5D				L=1.0D			
	Q_1	Q_3	Q_6	Q_{10}	Q_1	Q_3	Q_6	Q_{10}
FSE-0.3 MJ/kg	44.9	84.80	144	189.46	101.4	165.2	203.54	230.93
FSE-1.0 MJ/kg	122.85	188.30	259.60	318.72	260.77	325.46	420.10	532.30
FSE-3.0 MJ/kg	200	318.70	463.60	579.5	370.88	436.5	548.87	660.4

Here, it can be concluded that the effectiveness of unsteady energy deposition is higher, for single as well as periodic blast wave deposition of the same total strength, at elevated freestream stagnation enthalpy conditions. Further, periodic deposition of multiple small intensity pulses is found to be more effective than single pulse and there is increment in this effectiveness with increased number of pulses. It has also been observed that the increment in upstream deposition location has same effect as that of increase in the stagnation enthalpy for a given number of pulses. It is also marked that higher efficiency and higher drag reduction can be obtained at higher enthalpies if we deposit multiple pulses at further upstream locations.

6.4 Conclusions

Present computational investigations are carried for understanding the flow field of energy deposition-based drag reduction technique. For this, the pulsed energy is deposited at a location upstream of the bow shock of a sphere. This pulse travels with advancement of time and interacts with this standing bow shock. Comparison between perfect and real gas flow solver shows less rise in the surface pressure at the time of first interaction of pulse face with the bow shock if flow of real gas is assumed. The first valley in drag is also noted to be higher for RGS, hence real gas flow leads to lesser change for propulsion energy, as compared to perfect gas. A valley in the drag for each case is observed at the time of formation of a low-density vortex in the flow field. Advection of this vortex in downstream direction leads to the fluctuation in the stagnation pressure, wall pressure and in turn the wave drag force. High enthalpy inflow leads to decrease in density and an increase in pressure of the deposited pulse. Such pulse is responsible for higher wall pressure at the time of first interaction which increases further with higher enthalpy. On the other hand, decreased density of the core is accounted for deeper valley in the drag signal. Again, this valley increases with the stagnation enthalpy of the freestream. Higher strength of the low-density vortex formed due to lesser core density is found responsible for more reduction of wave drag.

It is worth to note that one more valley in time history of drag signal is present at higher enthalpy conditions. This shows the supportive nature of low-density vortex for high enthalpy inflow. It eventually leads to higher power effectiveness of the deposited pulse with the enthalpy. On the other hand, steady-state energy deposition shows an increase in the wall pressure with the inlet enthalpy. This leads to less reduction in the drag force and thus lower the power effectiveness of the pulse. It is worth to mention here that the unsteady energy deposition is a better method as compared with the steady energy deposition for the higher enthalpy freestream conditions. But higher magnitude of negative reduced energy is observed at higher enthalpy conditions for single pulse case which reflects higher drag force at the time of shock reflection. Therefore, periodic pulse deposition is studied to overcome the negative aspects of single energy deposition in high enthalpy flows. Increased pulses are observed to decrease the initial higher drag force and prolonge the drag reduction on the object. These changes reduce the decrement in negative propulsion energy which then enhances the positive reduced energy for the same strength of energy deposition. Thus periodic deposition enhances the energy efficiency of this technique which further improves at higher freestream enthalpy conditions and upstream deposition locations.

CHAPTER 7

CONCLUSIONS AND SCOPE OF FUTURE WORK

7.1 Summary of the present work

The objectives of the present thesis are to study the various flow alteration techniques and high enthalpy effects in non-equilibrium supersonic or hypersonic flow regime. Accordingly, a FVM based solver is developed with higher accuracy for laminar compressible flow simulations. This solver accounts five species and eleven elementary chemical reactions. Different types of gas model are also implemented in the solver to show the effect of reacting gas models over the non-reacting one as per the requirement. The temperature-dependent specific heats and transport terms are welded to demonstrate low as well as high enthalpy effects over the object. Before the detailed investigation, the present solver is validated with the different experimental and numerical results for two-dimensional and axisymmetric cases. The summary of the present work is as follows:-

- **Aerothermodynamic Assessment of Spiked Configuration For Drag Reduction at Hypersonic Speeds**
  Initial studies have been carried out to show the effect of reacting gas models over the non-reacting one on the blunt object. The downstream movement of bow shock and shock stand-off distance is observed at the higher enthalpy conditions. The stagnation pressure, as well as pressure at all locations on the object, is noted to be higher for the RGS as compared to the PGS for the same freestream higher enthalpy condition. Thus computed wave drag and frictional drag are higher for the reacting gas solver. Different chemical reactions decrease the temperature of flow for RGS which is responsible for the lower prediction of surface heat flux as compared to PGS. Further, a conical spike is attached to this blunt body, and simulation is performed for PGS and RGS at different

higher freestream stagnation enthalpies. The downstream shift of the UIL and the upstream movement of the SIL are observed at higher enthalpy. This leads to decrease in the size of recirculation zone for RGS and this is consistent with all spike lengths. Here, the computed wave drag and frictional drag are higher for RGS as compared to PGS for every case of spike at same freestream enthalpy condition. Two and three vortices for lower and higher spike lengths are observed at any freestream condition. Better drag reduction is achieved by longer spikes for lower as well as higher enthalpy. But the amount of drag reduction decreases for any length of the spike at higher stagnation enthalpy. Thus, it can be concluded that there is a need to account real gas effects while studying spiked body aerodynamics.

- **On Drag of a Spiked Body in Chemically Reacting Hypersonic Flow**
  The spike length is a very sensitive parameter to enhance or reduce the drag over the blunt object. Thus, this investigation is carried out to find the gas dynamic reason behind the drag enhancement as well as the drag reduction by using a forward-facing spike. Initial stagnation spike (L=0.125D) mounting is marked with higher skin frictional drag as compared to the wave drag and hence higher total drag on the object. Spike length of 0.2D initiates the Shock-Shock interaction and witnesses the peak surface pressure. Further higher length of the spike (L=0.25D) produces strong Shock-Shock interaction and an underdeveloped recirculation zone which lead to the maximum drag on the blunt object. After this spike length, two recirculation bubbles are observed in the separated region which reconstructs the shock structure near the reattachment. This phenomenon leads to the weaker S-S interaction which is responsible for the drag reduction for the blunt object. A thermodynamical parameter named exergy destruction is also simultaneously compared with total drag force to show the effectiveness of the spikes. In the support of this conclusion, the combination method of spike with the counter-flow jet is also investigated.

- **Evaluation of Drag for Spikes of Different Geometry in Non-equilibrium Hypersonic Flow**
  Studies are further extended for the prediction of drag force of a blunt object having spikes of different geometries. Three shapes such as round or spherical, flat and conical or pointed shapes of the spike of fixed length are selected for the drag evaluation at different low and high freestream stagnation enthalpy conditions. The downstream movement of conical shock leads to decrease in the recirculation area near the stagnation region. This shock reconstruction support higher wall pressure for every spike shape. However, the flat-ended spike bears lesser

pressure among all other spikes at low as well as high inlet enthalpy conditions. This flat-tipped spike is followed by the spherical and then conical ended spikes for effectiveness. It can be mentioned that the flat-ended spike is more efficient spike for drag reduction at every enthalpy case in non-equilibrium hypersonic flow. Further studies of spike (L=0.5D) with counterflow jet (PR=0.1) showed that the larger magnitude of drag reduction can be obtained by the combination of two drag methods.

- **An Effective Means of Drag Reduction in High Enthalpy Flow Through Unsteady Energy Deposition**
  The unsteady energy deposition (UED) based active flow alteration technique is also investigated to estimate the power effectiveness of energy pulse. Initially, various surface properties and drag signal results of the perfect and real gas solvers are compared at lower stagnation enthalpy conditions. Further, different higher freestream enthalpies are considered for the performance evaluation of the unsteady energy deposition. Here, density of the energy pulse decreases with the enthalpy and it is responsible for the generation of a strong low-density vortex during the interaction. These alterations lead to consistently lower drag as well as extra drag valley in the drag signal at higher enthalpy. Reduction in the wave drag is responsible for the higher power effectiveness of the blast wave at the higher FSE conditions. However, power effectiveness decreases with higher energy strength for fixed freestream enthalpy conditions. Steady energy deposition (SED) is also carried out to compare the power effectiveness with unsteady energy deposition. Higher freestream enthalpy leads to the advection of conical shock in the downstream direction which decreases the size of dead air zone for SED. These alterations conclude higher drag and thus lesser power effectiveness at the higher stagnation enthalpy conditions. It can be concluded that UED is a better drag reduction technique as compared to the SED at higher freestream stagnation enthalpy conditions. Possibilities of the performance enhancement of UED has also been explored with periodic energy depositions. It has been found that amount of drag reduction, period of drag reduction and power effectiveness are higher when same amount of energy is deposited in multiple pulses with a given frequency.

7.2 Scope of future work

- Present studies on the spike-based structural method of drag reduction technique are constrained to the steady-state only. The mounting of forward facing

stagnation spike produces multiple recirculation bubbles which may lead to unsteadiness in the flow field. Hence, incorporation of the turbulence model in steady reacting flow solver is necessary for the prediction of this unsteadiness in the flowfield. The benchmark of unsteadiness also needs to be investigated for different spikes and freestream conditions. Along with this, unsteadiness associated with other flowfield features such as shock-wave boundary layer interactions and shock-shock interaction should be studied with the help of a turbulent reacting flow solver in supersonic/hypersonic flow regimes.

- Three-dimensional numerical formulation of the present solver is necessary to widen the envelope of studies of the present reacting two-dimensional compressible flow solver. Further, extra chemical species such as CO_2, C and CO have to be incorporated in the present reacting solver to upgrade its potential.

- Unsteady energy deposition-based drag reduction technique is also investigated in present studies. Single pulse and periodic energy pulses are deposited along the stagnation streamline to study the power effectiveness in high enthalpy flow conditions. The drag reduction efficiency of this technique is strongly dependent on the shape, size and properties of the blast wave. Hence, different shapes of blast wave such as elliptical, with rotated major and minor axes, should be explored in the reacting flows. Further, different freestream Mach numbers and body geometries are also important parameters regarding performance enhancement in high enthalpy reacting flow conditions. Higher frequency of energy deposition is used to correlate the approach of steady energy deposition through the unsteady energy deposition. Moreover for 3-D object, the off-axis energy deposition is still an open area for the performance calculation with steady as well as unsteady energy depositions.

- At a time single active or passive drag reduction method has been used in the present thesis work. Therefore, a combination of the active and passive methods of drag reduction should also needed to be investigated for the larger amount of drag reduction in the reacting flows. Further, the heat flux reduction should also be addressed for the integration.

Publications

Journals

- **Kumar Shailendra** and Vinayak Kulkarni. "Drag of a Spiked Body in Chemically Reacting Hypersonic Flow." ***Journal of Spacecraft and Rockets***, 2020 Sep;57:1092-7

- **Kumar Shailendra**, Vinayak Kulkarni and Satya Pramod Jammy. "Aerothermodynamic Assessment of Spiked Configuration for Drag Reduction at Hypersonic Speeds." ***Journal of Aerospace Engineering***, 2020 Nov 1;33:04020076.

- **Kumar Shailendra** and Vinayak Kulkarni. "An Effective Means of Drag Reduction in High Enthalpy Flow Through Unsteady Energy Deposition". ***Acta Astronautica***, 2021 Sep 1;186:533-43.

- **Kumar Shailendra** and Vinayak Kulkarni. "Single and Periodic Energy Deposition in Reacting Non-equilibrium Flows". ***Applied Thermal Engineering***, 2021 (Under review)

- Patil Ajay, **Kumar Shailendra** and Vinayak Kulkarni, "Analysis of Counter Flow Injection Technique at Elevated Enthalpy Hypersonic Reacting Flows." ***International Journal of Heat and Mass Transfer***, (Review Submitted)

- Patil Ajay, **Kumar Shailendra** and Vinayak Kulkarni, "Exergy Destruction and Drag Reduction Analysis of Active and Passive Techniques". ***Journal of Aerospace Engineering*** (Under review)

Conferences

- **Kumar S**, Patel J, Kulkarni V and Jammy S P. Real Gas Effect on Spike of Different Geometry. *Proceedings of the* 25^{th} *National and* 3^{rd} *International ISHMT-ASTFE Heat and Mass Transfer Conference* ***(IHMTC-2019)*** 2019. Begel House Inc.

- Patil A, **Kumar S**, Kulkarni V and Jammy S P. Alterations in dynamics of counterjet injection technique in the presence of real gas effects. *Proceedings of the* 25^{th} *National and* 3^{rd} *International ISHMT-ASTFE Heat and Mass Transfer Conference* ***(IHMTC-2019)*** 2019. Begel House Inc.

APPENDIX

Table : Formulations of different flux computation schemes with suitable modifications

Scheme	**Flux formula**	**Terms**
	Interface flux, $H_{I_\perp} = {H_I}^+ + {H_I}^-$	${M_L}^+ = \begin{cases} M_L, & \text{if, } M_L \geq 1 \\ \frac{1}{4}(M_L+1)^2 & \text{if, } \lvert M_L \rvert < 1 \\ 0 & \text{if, } M_L \leq -1 \end{cases}$
Van-Leer	${H_I}^+ = H_{I_\perp},\ {H_I}^- = 0$ if, $M_\perp \geq 1$	
FVM	${H_I}^- = H_{I_\perp},\ {H_I}^+ = 0$ if, $M_\perp \geq -1$	
Van Leer B	$H_{I\perp} = H_I^+ + H_I^-$ if, $-1 < M_\perp < 1$	

Continued on next page

Table – *Continued from previous page*

Scheme	Flux formula	Terms
Van-Leer FVM Van Leer B	$H_{I_\perp} = \begin{bmatrix} \rho u_\perp \\ \rho u u_\perp + p n_x \\ \rho v u_\perp + p n_y \\ (\rho e + p) u_\perp \\ C_i u_\perp \end{bmatrix}$ i=1,2,...,N-1 if $\lvert M_\perp \rvert < 1$ $H_I^\pm = \begin{bmatrix} {f_{mass}}^\pm \\ {f_{mass}}^\pm \left[u + n_x \left(-u_\perp \pm 2a \right) \frac{p}{\rho a^2} \right] \\ {f_{mass}}^\pm \left[v + n_y \left(-u_\perp \pm 2a \right) \frac{p}{\rho a^2} \right] \\ {f_{mass}}^\pm \left[H + m \left(-u_\perp \pm a \right)^2 \right] \\ {f_{mass}}^\pm C_i / \rho] \end{bmatrix}$	$M_R{}^- = \begin{cases} 0 & \text{if, } M_R \geq 1 \\ \frac{1}{4}(M_R + 1)^2 & \text{if, } \lvert M_R \rvert < 1 \\ M_R & \text{if, } M_R \leq -1 \end{cases}$ $M_{\perp L} = \frac{u_{\perp L}}{a_L}, \quad M_{\perp R} = \frac{u_{\perp R}}{a_R}$ $f^+_{mass} = +\rho_L a_L \frac{(M_L + 1)^2}{4}$ $f^-_{mass} = -\rho_R a_R \frac{(M_R - 1)^2}{4}$ $m = \frac{h}{a^2 + 2h}$ h is specific enthalpy and H is total enthalpy.

Continued on next page

Table – *Continued from previous page*

Scheme	Flux formula	Terms
AUSM-delta Hybrid	Interface flux, $H_{I_\perp} = (M_n)_{I+\frac{1}{2}} \begin{bmatrix} \rho a \\ \rho a u \\ \rho a v \\ (\rho e + p) a \\ C_i a \end{bmatrix}_{L/R} + \begin{bmatrix} 0 \\ p n_x \\ p n_y \\ 0 \\ 0 \end{bmatrix}_{I+\frac{1}{2}}$ where $(M_n)_{I+\frac{1}{2}} = {M_L}^+ + {M_R}^-$ $(p)_{I+\frac{1}{2}} = {p_L}^+ + {p_R}^-$ $(M_n)_{I+\frac{1}{2}} = {M_L}^+ + {M_R}^-$ $(\cdot)_{L/R} = \begin{cases} (\cdot)_L & \text{if, } M_{n_{I+\frac{1}{2}}} \geq 0 \\ (\cdot)_R & Otherwise \end{cases}$ Interface flux,	$p_L^+ = \begin{cases} p_L & \text{if, } M_L \geq +1 \\ \frac{p_L}{4}(M_L+1)^2(2-M_L) & \text{if, } \lvert M_L \rvert < 1 \\ 0 & \text{if, } M_L \leq -1 \end{cases}$ $p_R^- = \begin{cases} 0 & \text{if, } M_R \geq +1 \\ \frac{p_R}{4}(M_R-1)^2(2+M_R) & \text{if, } \lvert M_R \rvert < 1 \\ p_R & \text{if, } M_R \leq -1 \end{cases}$ To avoid zero advection Mach number $(M_n)_{I+\frac{1}{2}}$ is modified in AUSM-delta as, $\lvert M_{n_{I+\frac{1}{2}}} \rvert = \begin{cases} \lvert M_{n_{I+\frac{1}{2}}} \rvert & \text{if, } \lvert M_{n_{I+\frac{1}{2}}} \rvert > \delta \\ \frac{{M_n}^2_{I+\frac{1}{2}} + \delta^2}{2\delta} & \text{if, } \lvert M_{n_{I+\frac{1}{2}}} \rvert \leq \delta \end{cases}$

Continued on next page

Table – *Continued from previous page*

Scheme	Flux formula	Terms
AUSM + Hybrid	$H_{I_\perp} = m_{I+\frac{1}{2}}{}^{+}(a)_{I+\frac{1}{2}} \begin{bmatrix} \rho a \\ \rho a u \\ \rho a v \\ (\rho e + p)a \\ C_i a \end{bmatrix}_L$	$M^{\pm}_{L/R} = \begin{cases} \frac{1}{2}\left(M_{L/R} \pm +\lvert M_{L/R}\rvert\right) & \text{if, } \lvert M_{L/R} > 1 \\ \pm\frac{1}{2}\left(M_{L/R} \pm 1\right)^2 \pm \beta\left({M_{L/R}}^2 - 1\right)^2 & \\ & \text{Otherwise} \end{cases}$
	$+m_{I+\frac{1}{2}}{}^{-}(a)_{I+\frac{1}{2}} \begin{bmatrix} \rho a \\ \rho a u \\ \rho a v \\ (\rho e + p)a \\ C_i a \end{bmatrix}_R + \begin{bmatrix} 0 \\ p n_x \\ p n_y \\ 0 \\ 0 \end{bmatrix}_{I+\frac{1}{2}}$	where, $-\frac{1}{6} \le \beta \le \frac{1}{2}$
	$p_{I+\frac{1}{2}} = {p_L}^{+} + {p_R}^{-}$	
	$m_{I+\frac{1}{2}} = {M_L}^{+} + {M_R}^{-} \qquad a_{I+\frac{1}{2}} = \sqrt{a_L a_R}$	$p_{L/R} = \begin{cases} \frac{1}{2}\left(1 \pm sign(M_{L/R})\right) & \text{if, } \lvert M_{L/R} \ge 1 \\ \frac{1}{4}\left(M_{L/R} \pm 1\right)^2\left(2 \mp M_{L/R}\right) \pm \alpha M_{L/R} & \\ \times\left(M^2_{L/R} - 1\right)^2 & \text{Otherwise} \end{cases}$
	$m^{\pm}_{I+\frac{1}{2}} = \frac{1}{2}\left(m_{I+\frac{1}{2}} + \lvert m_{I+\frac{1}{2}}\rvert\right)$	where $-\frac{2}{4} \le \alpha \le \frac{3}{16}$
	Interface flux, $H_{I_\perp} = \frac{1}{2}(H_{I_L} + H_{I_R}) - \frac{1}{2}S^{+}(U_R - U_L)$	$S^{+} = max\left(V_L + S_L, V_L - S_L, S_L, V_R + S_R V_R - S_R, S_R\right)$

Continued on next page

Table – *Continued from previous page*

Scheme	**Flux formula**	**Terms**
Rusanov FDM	$H_{L/R} = \begin{bmatrix} \rho u_\perp \\ \rho u u_\perp + p n_x \\ \rho v u_\perp + p n_y \\ (\rho e + p) u_\perp \\ C_i u_\perp \end{bmatrix}_{L/R}$	S_L and S_R can be calculated either from equation given below or can be approximated as corresponding sonic velocity at left and right of the face $S = \sqrt{{\lambda_0}^2 + \beta},\ \lambda_0 = u n_x + v n_y$ β = pseudo-compressibility parameter

REFERENCES

[1] Xue Y, Wang L, Fu S. Drag reduction and aerodynamic shape optimization for spike-tipped supersonic blunt nose. *Journal of Spacecraft and Rockets*. 55:552-60, (2018)

[2] Rego ID, Toro PG, Minucci MA, Chanes Júnior JB, Costa FJ, Oliveira AC. Calculation of the vehicle drag and heating reduction at hypervelocities with laser-induced air spike. *Journal of Aerospace Technology and Management*. 5:43-8, (2013)

[3] Mortazavi M, Knight DD, Azarova OA, Shi J, Yan H. Numerical simulation of energy deposition in a supersonic flow past a hemisphere. 52^{nd} *Aerospace Sciences Meeting*, (p. 0944), (2014)

[4] Fraile Jr AC, Rosa MA. A Numerical Investigation of Localized and Steady Energy Addition to High Speed Airflows. *Journal of Aerospace Technology and Management*, 5:169-80, (2013)

[5] Ganesh MA, John B. Concentrated energy addition for active drag reduction in hypersonic flow regime. *Acta Astronautica*, 142:221-31, (2018)

[6] Huang W. A survey of drag and heat reduction in supersonic flows by a counterflowing jet and its combinations. *Journal of Zhejiang University-Science A*, 16:551-61 (2015)

[7] Shen B, Liu W, Yin L. Drag and heat reduction efficiency research on opposing jet in supersonic flows. *Aerospace Science and Technology*, 77:696-703, (2018)

[8] Brainerd JG, Emmons HW. Effect of Variable Viscosity on Boundary Layers with a Discussion of Drag Measurements. *Journal of Applied Mechanics*, 9:A1-6, (1942)

[9] Moore LL. A solution of the laminar boundary-layer equations for a compressible fluid with variable properties, including dissociation. *Journal of the Aeronautical Sciences*, 19:505-18, (1952)

[10] Fay JA, Riddell FR. Theory of stagnation point heat transfer in dissociated air. *Journal of the Aerospace Sciences*, 25:73-85, (1958)

[11] Rose PH, Stark WI. Stagnation point heat-transfer measurements in dissociated air. *Journal of the Aerospace Sciences*, 25:86-97, (1958)

[12] Rose PH, Stankevics JO. Stagnation point heat transfer measurements in partially ionized air. *AIAA Journal*, 1:2752-63, (1963)

[13] Fenster SJ. Stagnation-point heat transfer for a new binary air model including dissociation and ionization. *AIAA Journal*, 3:2189-96, (1965)

[14] Conti R, Van Dyke M. Inviscid reacting flow near a stagnation point. *Journal of Fluid Mechanics*, 35:799-813, (1969)

[15] Liu Y, Vinokur M. Upwind algorithms for general thermo-chemical nonequilibrium flows. 27^{th} *Aerospace Sciences Meeting*, p. 201, (1989)

[16] Grossman B, Cinnella P. Flux-split algorithms for flows with non-equilibrium chemistry and vibrational relaxation. *Journal of Computational Physics*, 88:131-68, (1990)

[17] Netterfield M. Validation of a Navier-Stokes code for thermochemical non-equilibrium flows. 27^{th} *Thermophysics Conference*, p. 2878, (1992)

[18] Park C. Assessment of a two-temperature kinetic model for dissociating and weakly ionizing nitrogen. *Journal of Thermophysics and Heat Transfer*, 2:8-16, (1998)

[19] Park C. Review of chemical-kinetic problems of future NASA missions. I-Earth entries. *Journal of Thermophysics and Heat transfer*, 7:385-98, (1993)

[20] Sawley ML, Wothrich S. Non-equilibrium hypersonic flow simulations using the second-order boundary layer equations. *Computer Methods in Applied Mechanics and Engineering*, 89:129-40, (1991)

[21] Sabetta F, Favini B, Moretti G, Onofri M, Valorani M. Reactive and inert inviscid flow solutions by quasi-linear formulations and shock fitting. *Hypersonic Flows for Reentry Problems Springer*, pp. 782-797, (1991)

[22] Desideri JA, Glinsky N, Hettena E. Hypersonic reactive flow computations. *Computers Fluids*, 18:151-82, (1990)

[23] Hassan B, Candler GV, Olynick DR. Thermo-chemical nonequilibrium effects on the aerothermodynamics of aerobraking vehicles. *Journal of Spacecraft and Rockets*, 30:647-55, (1993)

[24] Miller JH, Tannehill JC, Lawrence SL, Edwards TA. Parabolized Navier–Stokes code for hypersonic flows in thermo-chemical equilibrium or nonequilibrium. *Computers Fluids*, 27:199-215, (1998)

[25] Candlar G. Computation of thermo-chemical nonequilibrium Martian atmospheric entry flows. *In 5th Joint Thermophysics and Heat Transfer Conference*, p. 1695, (1990)

[26] Gupta RN, Lee KP, Thompson RA, Yos JM. A review of reaction rates and thermodynamic and transport properties for an 11-species air model for chemical and thermal nonequilibrium calculations to 30000 K, (1990)

[27] Wen CY, Hornung HG. Non-equilibrium dissociating flow over spheres. *Journal of Fluid Mechanics*, 299:389-405, (1995)

[28] Argyris J, Doltsinis IS, Friz H, Urban J. An exploration of chemically reacting viscous hypersonic flow. *Computer Methods in Applied Mechanics and Engineering*, 89:85-128, (1991)

[29] Argyris J, Doltsinis IS, Friz H, Urban J. Physical and computational aspects of chemically reacting hypersonic flows. *Computer Methods in Applied Mechanics and Engineering*. 111:1-35, (1994)

[30] Reddy DS, Sinha K. Effect of chemical reaction rates on aeroheating predictions of reentry flows. *Journal of Thermophysics and Heat Transfer*, 25:21-33, (2011)

[31] Greenshields CJ, Reese JM. Rarefied hypersonic flow simulations using the Navier–Stokes equations with non-equilibrium boundary conditions. *Progress in Aerospace Sciences*, 52:80-7, (2012)

[32] Mair WA. LXVIII. Experiments on separation of boundary layers on probes in front of blunt-nosed bodies in a supersonic air stream. *The London, Edinburgh, and Dublin Philosophical Magazine and Journal of Science*, 43:695-716, (1952)

[33] Bogdonoff SM, Vas IE. Preliminary investigations of spiked bodies at hypersonic speeds. *Journal of the Aerospace Sciences*, 26:65-74, (1959)

[34] Maull DJ. Hypersonic flow over axially symmetric spiked bodies. *Journal of Fluid Mechanics*, 8:584-92, (1960)

[35] Wood CJ. Hypersonic flow over spiked cones. *Journal of Fluid Mechanics*, 12:614-24, (1962)

[36] Zorea C, Rom J. Effect of a Spike on the Drag and on the Aerodynamic Stability of Blunt Bodies in Supersonic Flow. *Journal of Spacecraft and Rockets*, 7:1017-9, (1970)

[37] Reding JP, Guenther RA, Richter BJ. Unsteady aerodynamic considerations in the design of a drag-reduction spike. *Journal of Spacecraft and Rockets*, 14:54-60, (1977)

[38] Hutt GR, Howe AJ. Forward facing spike effects on bodies of different cross section in supersonic flow. *The Aeronautical Journal*, 93:229-34, (1989)

[39] Shoemaker J. Aerodynamic spike flowfields computed to select optimum configuration at Mach 2.5 with experimental validation. 28^{th} *Aerospace Sciences Meeting*, p. 414 (1990)

[40] Yamauchi M, Fujii K, Higashino F. Numerical investigation of supersonic flows around a spiked blunt body. *Journal of Spacecraft and Rockets*, 32:32-42, (1995)

[41] Huebner L, Mitchell A, Boudreaux E. Experimental results on the feasibility of an aerospike for hypersonic missiles. 33^{rd} *Aerospace Sciences Meeting and Exhibit*, p. 737, (1995)

[42] Mikhail AG. Spike-nosed projectiles with vortex rings: steady and nonsteady flow simulations. *Journal of Spacecraft and Rockets*, 33:8-14, (1996)

[43] Motoyama N, Mihara K, Miyajima R, Watanuki T, Kubota H. Thermal protection and drag reduction with use of spike in hypersonic flow. 10^{th} *AIAA/NAL-NASDA-ISAS International Space Planes and Hypersonic Systems and Technologies Conference*, p. 1828, (2001)

[44] Milicev SS, Pavlovic MD. Influence of spike shape at supersonic flow past blunt-nosed bodies: experimental study. *AIAA Journal*, 40:1018-20, (2002)

[45] Menezes V, Saravanan S, Reddy KP. Shock tunnel study of spiked aerodynamic bodies flying at hypersonic Mach numbers. *Shock Waves*, 12:197-204, (2002)

[46] Asif M, Zahir S, Kamran N, Khan M. Computational investigations aerodynamic forces at supersonic/hypersonic flow past a blunt body with various forward facing spikes. 22^{nd} *Applied Aerodynamics Conference and Exhibit*, p. 5189, (2004)

[47] Kobayashi H, Maru Y, Fukiba K. Experimental study on aerodynamic characteristics of telescopic aerospikes with multiple disks. *Journal of spacecraft and Rockets*, 44:33-41, (2007)

[48] Kulkarni V, Menezes V, Reddy KP. Effectiveness of aerospike for drag reduction on a blunt cone in hypersonic flow. *Journal of Spacecraft and Rockets*, 47:542-4, (2010)

[49] Srinath S, Reddy KJ. Experimental investigation of the effects of aerospike geometry on aerodynamic drag and heat transfer rates for a blunt body configuration at hypersonic Mach numbers. *International Journal of Hypersonics*, (2010)

[50] Tahani M, Karimi MS, Motlagh AM, Mirmahdian S. Numerical investigation of drag and heat reduction in hypersonic spiked blunt bodies. Heat and Mass Transfer, 49:1369-84, (2013)

[51] Mohandas S, Siddharth RK, John B. Reduction of wave drag on parameterized blunt bodies using spikes with varied tip geometries. *Acta Astronautica*, 160:25-35, (2019)

[52] Srulijes J, Gnemmi P, Runne K, Seiler F. High-pressure shock tunnel experiments and CFD calculations on spike-tipped blunt bodies. 22^{nd} *AIAA Aerodynamic Measurement Technology and Ground Testing Conference*, p. 2918, (2002)

[53] Sahoo D, Das S, Kumar P, Prasad JK. Effect of spike on steady and unsteady flow over a blunt body at supersonic speed. *Acta Astronautica*, 28:521-33, (2016)

[54] Mehta RC. Numerical heat transfer study around a spiked blunt-nose body at Mach 6. *Heat and Mass Transfer*, 49:485-96, (2013)

[55] Gerdroodbary MB, Hosseinalipour SM. Numerical simulation of hypersonic flow over highly blunted cones with spike. *Acta Astronautica*, 67:180-93, (2010)

[56] Ahmed MY, Qin N. Metamodels for aerothermodynamic design optimization of hypersonic spiked blunt bodies. *Aerospace Science and Technology*, 14:364-76, (2010)

[57] Kharati-Koopaee M, Gazor H. Assessment of the aerodisk size on drag reduction and thermal protection of high-bluntness vehicles at hypersonic speeds. *Journal of Aerospace Engineering*, 30:04017008, (2017)

[58] Yadav R, Velidi G, Guven U. Aerothermodynamics of generic re-entry vehicle with a series of aerospikes at nose. *Acta Astronautica*, 96:1-0, (2014)

[59] Borzov VY, Rybka IV, Yur'ev AS. Effect of local energy supply to a hypersonic flow on the drag of bodies with different nose bluntness. *Journal of Engineering Physics and Thermophysics*, 67:997-1002, (1994)

[60] Levin VA, Terent'eva LV. Supersonic flow over a cone with heat release in the neighborhood of the apex. *Fluid Dynamics*, 28:244-7, (1993)

[61] Levin VA, Gromov VG, Afonina NE. Numerical analysis of the effect of local energy supply on the aerodynamic drag and heat transfer of a spherically blunted body in a supersonic air flow. *Journal of Applied Mechanics and Technical Physics*, 41:915-22, (2000)

[62] Vlasov VV, Grudnitskii BG, Rygalin VN. Gas dynamics with local energy release in subsonic and supersonic flow. *Fluid Dynamics*, 30:275-80, (1995)

[63] Riggins D, Nelson HF, Johnson E. Blunt-body wave drag reduction using focused energy deposition. *AIAA Journal*, 37:460-7, (1999)

[64] Riggins DW, Nelson HF. Hypersonic flow control using upstream focused energy deposition. *AIAA Journal*, 38:723-5, (2000)

[65] Bracken R, Myrabo L, Nagamatsu H, Meloney E, Shneider M. Experimental investigation of an electric arc air-spike in Mach 10 flow with preliminary drag measurements. 32^{nd} *AIAA Plasmadynamics and Lasers Conference*, p. 2734, (2001)

[66] Georgievskii PY, Levin VA. Control of the flow past bodies using localized energy addition to the supersonic oncoming flow. *Fluid Dynamics*, 38:794-805, (2003)

[67] Erdem E, Yang L, Kontis K. Drag reduction studies by steady energy deposition at Mach 5. 49^{th} *AIAA Aerospace Sciences Meeting including the New Horizons Forum and Aerospace Exposition*, p. 1027, (2011)

[68] Gutiérrez DR, Poggie J. Effects of power deposition on the aerodynamic forces on a slender body. *AIAA Journal*, 56:2911-7, (2018)

[69] Kulkarni V, Hegde GM, Jagadeesh G, Arunan E, Reddy KP. Aerodynamic drag reduction by heat addition into the shock layer for a large angle blunt cone in hypersonic flow. *Physics of Fluids*, 20:081703, (2008)

[70] Ganesh MA, John B. Concentrated energy addition for active drag reduction in hypersonic flow regime. *Acta Astronautica*, 142:221-31, (2018)

[71] Knight D. Survey of aerodynamic drag reduction at high speed by energy deposition. *Journal of Propulsion and Power*, 24:1153-67, (2008)

[72] Shneyder M, Macheret S, Zaidi S, Girgis I, Miles R. Steady and unsteady supersonic flow control with energy addition. 34^{th} *AIAA Plasmadynamics and Lasers Conference*, p. 3862, (2003)

[73] Desai S, Kulkarni V, Gadgil H, John B. Aerothermodynamic considerations for energy deposition based drag reduction technique. *Applied Thermal Engineering*, 122:451-60, (2017)

[74] Das D, Desai S, Kulkarni V, Gadgil H. Performance assessment of energy deposition based drag reduction technique for Earth and Mars flight conditions. *Acta Astronautica*, 159:418-28, (2019

[75] Nedungadi A, Lewis MJ. Computational study of the flowfields associated with oblique shock/vortex interactions. *AIAA Journal*, 34:2545-53, (1996)

[76] Kolesnichenko Y, Brovkin V, Azarova O, Grudnitsky V, Lashkov V, Mashek I. Microwave energy release regimes for drag reduction in supersonic flows. 40^{th} *AIAA Aerospace Sciences Meeting Exhibit*, p. 353, (2002)

[77] Georgievsky P, Levin V. Bow shock wave structures control by pulse-periodic energy input. 42^{nd} *AIAA Aerospace Sciences Meeting and Exhibit*, p. 1019, (2004)

[78] Hong Y, Wang D, Li Q, Ye J. Interaction of single-pulse laser energy with bow shock in hypersonic flow. *Chinese Journal of Aeronautics*, 27:241-7, (2004)

[79] Knight D, Kolesnichenko YF, Brovkin V, Khmara D, Lashkov V, Mashek I. Interaction of microwave-generated plasma with a hemisphere cylinder at mach 2.1. *AIAA Journal*, 47:2996-3010, (2009)

[80] Kremeyer K, Sebastian K, Shu CW. Computational study of shock mitigation and drag reduction by pulsed energy lines. *AIAA Journal*, 44:1720-31, (2006)

[81] Osuka T, Erdem E, Hasegawa N, Majima R, Tamba T, Yokota S, Sasoh A, Kontis K. Laser energy deposition effectiveness on shock-wave boundary-layer interactions over cylinder-flare combinations. *Physics of Fluids*, 26:096103, (2014)

[82] Sakai T. Supersonic drag performance of truncated cones with repetitive energy depositions. *International Journal of Aerospace Innovations*, 1:31-43, (2009)

[83] SuSasoh A, Sekiya Y, Sakai T, Kim JH, Matsuda A. Supersonic drag reduction with repetitive laser pulses through a blunt body. *AIAA Journal*, 48:2811-7, (2010)

[84] Sasoh A, Kim JH, Yamashita K, Sakai T. Supersonic aerodynamic performance of truncated cones with repetitive laser pulse energy depositions. *Shock Waves*, 24:59-67, (2014)

[85] Taguchi S, Ohnishi N, Furudate M, Sawada K. Numerical analysis of drag reduction for supersonic blunt body by pulse energy deposition. 45^{th} *AIAA Aerospace Sciences Meeting*, pp. 14760-14767, (2007)

[86] Kianvashrad N, Knight DD. Non-Equilibrium Effects of Interaction of Laser Discharge with Hemisphere-Cylinder in Supersonic Flow. *Flow Control Conference*, p. 3757, (2018)

[87] Kianvashrad N, Knight DD, Wilkinson SP, Chou A, Horne RA, Herring GC, Beeler GB, Jangda M. Effect of off-body laser discharge on drag reduction of hemisphere cylinder in supersonic flow. 48^{th} *AIAA Plasmadynamics and Lasers Conference*, p. 3478, (2017)

[88] Kim JH, Matsuda A, Sakai T, Sasoh A. Wave drag reduction with acting spike induced by laser-pulse energy depositions. *AIAA Journal*, 49:2076-8, (2011)

[89] Adelgren RG, Yan H, Elliott GS, Knight DD, Beutner TJ, Zheltovodov AA. Control of Edney IV interaction by pulsed laser energy deposition. *AIAA Journal*, 43:256-69, (2005)

[90] Lashkov V, Mashek I, Anisimov Y, Ivanov V, Kolesnichenko Y, Ryvkin M. Gas dynamic effect of microwave discharge on supersonic cone-shaped bodies. 42^{nd} *AIAA Aerospace Sciences Meeting and Exhibit*, p. 671 (2004)

[91] Zheltovodov A, Pimonov E, Knight D. Energy deposition influence on supersonic flow over axisymmetric bodies. 45^{th} *AIAA Aerospace Sciences Meeting and Exhibit*, p. 1230, (2007)

[92] Kandala R, Candler GV. Numerical studies of laser-induced energy deposition for supersonic flow control. 41^{st} *Aerospace Sciences Meeting and Exhibit* (2003).

[93] Kandala R, Candler GV. Numerical studies of laser-induced energy deposition for supersonic flow control. *AIAA Journal*, 42:2266-75, (2004)

[94] Sangtabi AR, Ramiar A, Ranjbar AA, Abdollahzadeh M, Kianifar A. Influence of repetitive laser pulse energy depositions on supersonic flow over a sphere, cone and oblate spheroid. *Aerospace Science and Technology*, 76:72-81, (2018)

[95] Ogino Y, Ohnishi N, Taguchi S, Sawada K. Baroclinic vortex influence on wave drag reduction induced by pulse energy deposition. *Physics of Fluids*, 21:066102, (2009)

[96] Edney B. Anomalous Heat Transfer and Pressure Distributions on Blunt Bodies at Hypersonic Speeds in the Presence of an Impinging Shock. Flygtekniska Forsoksanstalten, Stockholm (Sweden), (1968)

[97] Crawford DH. A graphical method for the investigation of shock interference phenomena. *AIAA Journal*, 11(11):1590-2, (1973)

[98] BRAMLETTE TT. Simple Technique for Predicting Type 11 and IV Shock Interference. *AIAA Journal*, 12:1151-2, (1974)

[99] Furumoto G, Zhong X, Furumoto G, Zhong X. Numerical simulation of viscous unsteady type IV shock-shock interaction with thermochemical nonequilibrium. 35^{th} *Aerospace Sciences Meeting and Exhibit*, p. 982, (1997)

[100] Holden M, Moselle J, Wieting A, Glass C. Studies of aerothermal loads generated in regions of shock/shock interaction in hypersonic flow. 26^{th} *Aerospace Sciences Meeting*, p. 477, (1988)

[101] Lind CA, Lewis MJ. Computational analysis of the unsteady type IV shock interaction of blunt body flows. *Journal of Propulsion and Power*, 12:127-33, (1996)

[102] Olejniczak J, Wright M, Candler G. Numerical study of shock interactions on double-wedge geometries. *In 34th Aerospace Sciences Meeting and Exhibit*, p. 41 , (1996)

[103] Boldyrev SM, Borovoy VY, Chinilov AY, Gusev VN, Krutiy SN, Struminskaya IV, Yakovleva LV, Délery J, Chanetz B. A thorough experimental investigation of shock/shock interferences in high Mach number flows. *Aerospace Science and Technology*, 5:167-78, (2001)

[104] Grasso F, Purpura C, Chanetz B, Délery J. Type III and type IV shock/shock interferences: theoretical and experimental aspects. *Aerospace Science and Technology*, 7:93-106, (2003)

[105] Gordon S, McBride BJ. Computer Program for Calculation of Complex Chemical Equilibrium. *NASA Reference Publication*, 1311, (1994)

[106] Shuen JS, Liou MS, Van Leer B. Inviscid flux-splitting algorithms for real gases with non-equilibrium chemistry. *Journal of Computational Physics*, 90:371-95, (1990)

[107] Liou MS, Steffen Jr CJ. A new flux splitting scheme. *Journal of Computational Physics*, 107:23-39, (1993)

[108] Liou MS. A sequel to ausm: Ausm+. *Journal of computational Physics*, 129:364-82, (1996)

[109] Van Leer B. Flux-vector splitting for the Euler equation. In Upwind and high-resolution schemes, *Springer, Berlin, Heidelberg*, pp. 80-89, (1997)

[110] Calculation of interaction of non-steady shock waves with obstacles. *NRC, Division of Mechanical Engineering*, (1962)

[111] Barth TJ and Jespersen D. The design and application of upwind schemes on unstructured meshes. *AIAA Paper*, 89-0366, (1989)

[112] Blazek J. *Computational fluid dynamics: principles and applications*, *Elsevier, Amsterdam*, (2001)

[113] Poinsot TJ, Lelef SK. Boundary conditions for direct simulations of compressible viscous flows. *Journal of Computational Physics*, 101:104-29, (1992)

[114] Bussing TR, Murman EM. Finite-volume method for the calculation of compressible chemically reacting flows. *AIAA Journal*, 26:1070-8, (1988)

[115] John B, Sarath G, Kulkarni V, Natarajan G. Performance comparison of flux schemes for numerical simulation of high-speed inviscid flows. *Progress in Computational Fluid Dynamics, an International Journal*, 14:83-96, (2014)

[116] Sutherland W. LII. The viscosity of gases and molecular force. *The London, Edinburgh, and Dublin Philosophical Magazine and Journal of Science*, 36:507-31, (1893)

[117] Huang J, Li P, Yao W. Thermal protection system gap analysis using a loosely coupled fluid-structural thermal numerical method. *Acta Astronautica*, 146:368-77, (2018)

[118] Hinman WS, Johansen CT. Rapid prediction of hypersonic blunt body flows for parametric design studies. *Aerospace science and technology*, 58:48-59, (2016)

[119] Li SB, Wang ZG, Huang W, Liu J. Drag and heat reduction performance for an equal polygon opposing jet. *Journal of Aerospace Engineering*, 30:04016065, (2017)

[120] Zaidi S, Shneider M, Mansfield D, Ionikh Y, Miles R. Influence of Upstream Pulsed Energy Addition on Shock-Wave Structure in Supersonic Flow. 22^{nd} *AIAA Aerodynamic Measurement Technology and Ground Testing Conference*, p. 2703 (2002)

[121] Huang J, Yao WX. Multi-objective design optimization of blunt body with spike and aerodisk in hypersonic flow. *Aerospace Science and Technology*, (2019)

[122] Huang W, Zhao ZT, Yan L, Zhou Y, Zhang RR. Parametric study on the drag and heat flux reduction mechanism of forward-facing cavity on a blunt body in supersonic flows. *Aerospace Science and Technology*, 71:619-26, (2017)

[123] Zhu L, Li Y, Chen X, Gong L, Xu J, Feng Z. Novel combinational aerodisk and lateral jet concept for drag and heat reduction in hypersonic flows. *Journal of Aerospace Engineering*, 32:04018133, (2019)

[124] Gauer M, Paull A. Numerical investigation of a spiked blunt nose cone at hypersonic speeds. *Journal of Spacecraft and Rockets*, 45:459-71, (2018)

[125] d'Humières G, Stollery JL. Drag reduction on a spiked body at hypersonic speed. *The Aeronautical Journal*, 114:113-9, (2010)

[126] Billig FS. Shock-wave shapes around spherical-and cylindrical-nosed bodies. *Journal of Spacecraft and Rockets*, 4:822-3, (1967)

[127] Kulkarni V, Reddy KP. Effect of a supersonic counterflow jet on blunt body heat transfer rates for oncoming high enthalpy flow. *Journal of Engineering Physics and Thermophysics*, 82:1-5, (2019)

[128] Lee L. Laminar heat transfer rate over blunt nosed body at hypersonic speeds. *Jet Propulsion*, 26:259-69, (1956)

[129] Bibin J, Vinayak K. Numerical assessment of correlations for shock wave boundary layer interaction. *Computers & Fluids* 2014; **90**:42–50.

[130] Guy Y, McLaughlin T, Morrow J. Blunt body wave drag reduction by means of a standoff spike. 39^{th} *Aerospace Sciences Meeting and Exhibit*, p. 888, (2001)

[131] Jones E, Townsend S, Guy Y, McLaughlin T. Reduction of the wave drag of a blunt body by means of a standoff spike. 38^{th} *Aerospace Sciences Meeting and Exhibit*, p. 268, (2000)

[132] Kalimuthu R, Mehta RC, Rathakrishnan E. Drag reduction for spike attached to blunt-nosed body at Mach 6. *Journal of Spacecraft and Rockets*, 47:219-22, (2010)

[133] Yisheng R. Drag reduction research in supersonic flow with opposing jet. *Acta Astronautica*, 91:1-7, (2013)

[134] Bibin J, Vinayak K. Investigation of energy deposition technique for drag reduction at hypersonic speeds. *Applied Mechanics and Materials*, 367:222-227 (2013)

[135] Hong Y, Wang D, Li Q, Ye J. Interaction of single-pulse laser energy with bow shock in hypersonic flow. *Chinese Journal of Aeronautics*, 27:241-7, (2014)